

## Dark Energy Survey year 3 results: Constraints on cosmological parameters and galaxy-bias models from galaxy clustering and galaxy-galaxy lensing using the redMaGiC sample

S. Pandey<sup>1,\*</sup> E. Krause,<sup>2</sup> J. DeRose,<sup>3</sup> N. MacCrann,<sup>4</sup> B. Jain,<sup>1</sup> M. Crocce,<sup>5,6</sup> J. Blazek,<sup>7,8</sup> A. Choi,<sup>9</sup> H. Huang,<sup>10</sup> C. To,<sup>11,12,13</sup> X. Fang,<sup>2</sup> J. Elvin-Poole,<sup>9,14</sup> J. Prat,<sup>15,16</sup> A. Porredon,<sup>9,14</sup> L. F. Secco,<sup>1,16</sup> M. Rodriguez-Monroy,<sup>17</sup> N. Weaverdyck,<sup>18</sup> Y. Park,<sup>19</sup> M. Raveri,<sup>1</sup> E. Rozo,<sup>10</sup> E. S. Rykoff,<sup>12,13</sup> G. M. Bernstein,<sup>1</sup> C. Sánchez,<sup>1</sup> M. Jarvis,<sup>1</sup> M. A. Troxel,<sup>20</sup> G. Zacharegkas,<sup>16</sup> C. Chang,<sup>15,16</sup> A. Alarcon,<sup>21</sup> O. Alves,<sup>18,22,23</sup> A. Amon,<sup>12</sup> F. Andrade-Oliveira,<sup>22,23</sup> E. Baxter,<sup>24</sup> K. Bechtol,<sup>25</sup> M. R. Becker,<sup>21</sup> H. Camacho,<sup>22,23</sup> A. Campos,<sup>26</sup> A. Carnero Rosell,<sup>27,23,28</sup> M. Carrasco Kind,<sup>29,30</sup> R. Cawthon,<sup>25</sup> R. Chen,<sup>20</sup> P. Chintalapati,<sup>31</sup> C. Davis,<sup>12</sup> E. Di Valentino,<sup>32</sup> H. T. Diehl,<sup>31</sup> S. Dodelson,<sup>26,33</sup> C. Doux,<sup>1</sup> A. Drlica-Wagner,<sup>15,31,16</sup> K. Eckert,<sup>1</sup> T. F. Eifler,<sup>2,34</sup> F. Elsner,<sup>35</sup> S. Everett,<sup>36</sup> A. Farahi,<sup>18,37</sup> A. Ferté,<sup>34</sup> P. Fosalba,<sup>5,6</sup> O. Friedrich,<sup>38</sup> M. Gatti,<sup>1</sup> G. Giannini,<sup>39</sup> D. Gruen,<sup>11,12,13</sup> R. A. Gruendl,<sup>29,30</sup> I. Harrison,<sup>40,32</sup> W. G. Hartley,<sup>41</sup> E. M. Huff,<sup>34</sup> D. Huterer,<sup>18</sup> A. Kovacs,<sup>27,28</sup> P. F. Leget,<sup>12</sup> J. McCullough,<sup>12</sup> J. Muir,<sup>12</sup> J. Myles,<sup>11,12,13</sup> A. Navarro-Alsina,<sup>42</sup> Y. Omori,<sup>15,16,12</sup> R. P. Rollins,<sup>32</sup> A. Roodman,<sup>12,13</sup> R. Rosenfeld,<sup>43,23</sup> I. Sevilla-Noarbe,<sup>17</sup> E. Sheldon,<sup>44</sup> T. Shin,<sup>1</sup> A. Troja,<sup>43,23</sup> I. Tutusaus,<sup>5,6</sup> T. N. Varga,<sup>45,46</sup> R. H. Wechsler,<sup>11,12,13</sup> B. Yanny,<sup>31</sup> B. Yin,<sup>26</sup> Y. Zhang,<sup>31</sup> J. Zuntz,<sup>47</sup> T. M. C. Abbott,<sup>48</sup> M. Aguena,<sup>23</sup> S. Allam,<sup>31</sup> J. Annis,<sup>31</sup> D. Bacon,<sup>49</sup> E. Bertin,<sup>50,51</sup> D. Brooks,<sup>35</sup> D. L. Burke,<sup>12,13</sup> J. Carretero,<sup>39</sup> C. Conselice,<sup>32,52</sup> M. Costanzi,<sup>53,54,55</sup> L. N. da Costa,<sup>23,56</sup> M. E. S. Pereira,<sup>18</sup> J. De Vicente,<sup>17</sup> J. P. Dietrich,<sup>57</sup> P. Doel,<sup>35</sup> A. E. Evrard,<sup>58,18</sup> I. Ferrero,<sup>59</sup> B. Flaugher,<sup>31</sup> J. Frieman,<sup>31,16</sup> J. García-Bellido,<sup>60</sup> E. Gaztanaga,<sup>5,6</sup> D. W. Gerdes,<sup>58,18</sup> T. Giannantonio,<sup>61,38</sup> J. Gschwend,<sup>23,56</sup> G. Gutierrez,<sup>31</sup> S. R. Hinton,<sup>62</sup> D. L. Hollowood,<sup>36</sup> K. Honscheid,<sup>9,14</sup> D. J. James,<sup>63</sup> T. Jeltema,<sup>36</sup> K. Kuehn,<sup>64,65</sup> N. Kuropatkin,<sup>31</sup> O. Lahav,<sup>35</sup> M. Lima,<sup>66,23</sup> H. Lin,<sup>31</sup> M. A. G. Maia,<sup>23,56</sup> J. L. Marshall,<sup>67</sup> P. Melchior,<sup>68</sup> F. Menanteau,<sup>29,30</sup> C. J. Miller,<sup>58,18</sup> R. Miquel,<sup>69,39</sup> J. J. Mohr,<sup>57,45</sup> R. Morgan,<sup>25</sup> A. Palmese,<sup>31,16</sup> F. Paz-Chinchón,<sup>29,61</sup> D. Petravick,<sup>29</sup> A. Pieres,<sup>23,56</sup> A. A. Plazas Malagón,<sup>68</sup> E. Sanchez,<sup>17</sup> V. Scarpine,<sup>31</sup> S. Serrano,<sup>5,6</sup> M. Smith,<sup>70</sup> M. Soares-Santos,<sup>18</sup> E. Suchyta,<sup>71</sup> G. Tarle,<sup>18</sup> D. Thomas,<sup>49</sup> and J. Weller<sup>45,46</sup>

(DES Collaboration)

<sup>1</sup>*Department of Physics and Astronomy, University of Pennsylvania, Philadelphia, Pennsylvania 19104, USA*

<sup>2</sup>*Department of Astronomy/Steward Observatory, University of Arizona, 933 North Cherry Avenue, Tucson, Arizona 85721-0065, USA*

<sup>3</sup>*Lawrence Berkeley National Laboratory, 1 Cyclotron Road, Berkeley, California 94720, USA*

<sup>4</sup>*Department of Applied Mathematics and Theoretical Physics, University of Cambridge, Cambridge CB3 0WA, United Kingdom*

<sup>5</sup>*Institut d'Estudis Espacials de Catalunya (IEEC), 08034 Barcelona, Spain*

<sup>6</sup>*Institute of Space Sciences (ICE, CSIC),*

*Campus UAB, Carrer de Can Magrans, s/n, 08193 Barcelona, Spain*

<sup>7</sup>*Department of Physics, Northeastern University, Boston, Massachusetts 02115, USA*

<sup>8</sup>*Laboratory of Astrophysics, École Polytechnique Fédérale de Lausanne (EPFL), Observatoire de Sauverny, 1290 Versoix, Switzerland*

<sup>9</sup>*Center for Cosmology and Astro-Particle Physics, The Ohio State University, Columbus, Ohio 43210, USA*

<sup>10</sup>*Department of Physics, University of Arizona, Tucson, Arizona 85721, USA*

<sup>11</sup>*Department of Physics, Stanford University, 382 Via Pueblo Mall, Stanford, California 94305, USA*

<sup>12</sup>*Kavli Institute for Particle Astrophysics and Cosmology, P.O. Box 2450, Stanford University, Stanford, California 94305, USA*

<sup>13</sup>*SLAC National Accelerator Laboratory, Menlo Park, California 94025, USA*

<sup>14</sup>*Department of Physics, The Ohio State University, Columbus, Ohio 43210, USA*

<sup>15</sup>*Department of Astronomy and Astrophysics, University of Chicago, Chicago, Illinois 60637, USA*

<sup>16</sup>*Kavli Institute for Cosmological Physics, University of Chicago, Chicago, Illinois 60637, USA*

<sup>17</sup>*Centro de Investigaciones Energéticas, Medioambientales y Tecnológicas (CIEMAT), Madrid, Spain*

<sup>18</sup>*Department of Physics, University of Michigan, Ann Arbor, Michigan 48109, USA*

<sup>19</sup>*Kavli Institute for the Physics and Mathematics of the Universe (WPI), UTIAS, The University of Tokyo, Kashiwa, Chiba 277-8583, Japan*

<sup>20</sup>*Department of Physics, Duke University Durham, North Carolina 27708, USA*

<sup>21</sup>*Argonne National Laboratory, 9700 South Cass Avenue, Lemont, Illinois 60439, USA*

- <sup>22</sup>*Instituto de Física Teórica, Universidade Estadual Paulista, São Paulo, Brazil*
- <sup>23</sup>*Laboratório Interinstitucional de e-Astronomia - LIneA,  
Rua Gal. José Cristino 77, Rio de Janeiro, RJ - 20921-400, Brazil*
- <sup>24</sup>*Institute for Astronomy, University of Hawai'i, 2680 Woodlawn Drive, Honolulu, Hawaii 96822, USA*
- <sup>25</sup>*Physics Department, 2320 Chamberlin Hall, University of Wisconsin–Madison,  
1150 University Avenue, Madison, Wisconsin 53706-1390, USA*
- <sup>26</sup>*Department of Physics, Carnegie Mellon University, Pittsburgh, Pennsylvania 15312, USA*
- <sup>27</sup>*Instituto de Astrofísica de Canarias, E-38205 La Laguna, Tenerife, Spain*
- <sup>28</sup>*Universidad de La Laguna, Departamento Astrofísica, E-38206 La Laguna, Tenerife, Spain*
- <sup>29</sup>*Center for Astrophysical Surveys, National Center for Supercomputing Applications,  
1205 West Clark Street, Urbana, Illinois 61801, USA*
- <sup>30</sup>*Department of Astronomy, University of Illinois at Urbana-Champaign,  
1002 West Green Street, Urbana, Illinois 61801, USA*
- <sup>31</sup>*Fermi National Accelerator Laboratory, P.O. Box 500, Batavia, Illinois 60510, USA*
- <sup>32</sup>*Jodrell Bank Center for Astrophysics, School of Physics and Astronomy, University of Manchester,  
Oxford Road, Manchester, M13 9PL, United Kingdom*
- <sup>33</sup>*NSF AI Planning Institute for Physics of the Future, Carnegie Mellon University,  
Pittsburgh, Pennsylvania 15213, USA*
- <sup>34</sup>*Jet Propulsion Laboratory, California Institute of Technology,  
4800 Oak Grove Drive, Pasadena, California 91109, USA*
- <sup>35</sup>*Department of Physics and Astronomy, University College London,  
Gower Street, London, WC1E 6BT, United Kingdom*
- <sup>36</sup>*Santa Cruz Institute for Particle Physics, Santa Cruz, California 95064, USA*
- <sup>37</sup>*Departments of Statistics and Data Science, University of Texas at Austin, Austin, Texas 78757, USA*
- <sup>38</sup>*Kavli Institute for Cosmology, University of Cambridge,  
Madingley Road, Cambridge CB3 0HA, United Kingdom*
- <sup>39</sup>*Institut de Física d'Altes Energies (IFAE), The Barcelona Institute of Science and Technology,  
Campus UAB, 08193 Bellaterra (Barcelona), Spain*
- <sup>40</sup>*Department of Physics, University of Oxford,  
Denys Wilkinson Building, Keble Road, Oxford OX1 3RH, United Kingdom*
- <sup>41</sup>*Department of Astronomy, University of Geneva, ch. d'Écogia 16, CH-1290 Versoix, Switzerland*
- <sup>42</sup>*Instituto de Física Gleb Wataghin, Universidade Estadual de Campinas,  
13083-859, Campinas, SP, Brazil*
- <sup>43</sup>*ICTP South American Institute for Fundamental Research, Instituto de Física Teórica,  
Universidade Estadual Paulista, São Paulo, Brazil*
- <sup>44</sup>*Brookhaven National Laboratory, Building 510, Upton, New York 11973, USA*
- <sup>45</sup>*Max Planck Institute for Extraterrestrial Physics, Giessenbachstrasse, 85748 Garching, Germany*
- <sup>46</sup>*Universitäts-Sternwarte, Fakultät für Physik, Ludwig-Maximilians Universität München,  
Scheinerstrasse 1, 81679 München, Germany*
- <sup>47</sup>*Institute for Astronomy, University of Edinburgh, Edinburgh EH9 3HJ, United Kingdom*
- <sup>48</sup>*Cerro Tololo Inter-American Observatory, NSF's National Optical-Infrared Astronomy Research  
Laboratory, Casilla 603, La Serena, Chile*
- <sup>49</sup>*Institute of Cosmology and Gravitation, University of Portsmouth,  
Portsmouth, PO1 3FX, United Kingdom*
- <sup>50</sup>*CNRS, UMR 7095, Institut d'Astrophysique de Paris, F-75014, Paris, France*
- <sup>51</sup>*Sorbonne Universités, UPMC Université Paris 06, UMR 7095,  
Institut d'Astrophysique de Paris, F-75014, Paris, France*
- <sup>52</sup>*University of Nottingham, School of Physics and Astronomy, Nottingham NG7 2RD, United Kingdom*
- <sup>53</sup>*Astronomy Unit, Department of Physics, University of Trieste, via Tiepolo 11, I-34131 Trieste, Italy*
- <sup>54</sup>*INAF-Osservatorio Astronomico di Trieste, via G. B. Tiepolo 11, I-34143 Trieste, Italy*
- <sup>55</sup>*Institute for Fundamental Physics of the Universe, Via Beirut 2, 34014 Trieste, Italy*
- <sup>56</sup>*Observatório Nacional, Rua Gal. José Cristino 77, Rio de Janeiro, RJ - 20921-400, Brazil*
- <sup>57</sup>*Faculty of Physics, Ludwig-Maximilians-Universität, Scheinerstrasse 1, 81679 Munich, Germany*
- <sup>58</sup>*Department of Astronomy, University of Michigan, Ann Arbor, Michigan 48109, USA*
- <sup>59</sup>*Institute of Theoretical Astrophysics, University of Oslo,  
P.O. Box 1029, Blindern, NO-0315 Oslo, Norway*
- <sup>60</sup>*Instituto de Física Teórica UAM/CSIC, Universidad Autónoma de Madrid, 28049 Madrid, Spain*
- <sup>61</sup>*Institute of Astronomy, University of Cambridge,  
Madingley Road, Cambridge CB3 0HA, United Kingdom*
- <sup>62</sup>*School of Mathematics and Physics, University of Queensland, Brisbane, Queensland 4072, Australia*

<sup>63</sup>*Center for Astrophysics | Harvard and Smithsonian,*

*60 Garden Street, Cambridge, Massachusetts 02138, USA*

<sup>64</sup>*Australian Astronomical Optics, Macquarie University, North Ryde, New South Wales 2113, Australia*

<sup>65</sup>*Lowell Observatory, 1400 Mars Hill Road, Flagstaff, Arizona 86001, USA*

<sup>66</sup>*Departamento de Física Matemática, Instituto de Física, Universidade de São Paulo,*

*CP 66318, São Paulo, SP, 05314-970, Brazil*

<sup>67</sup>*George P. and Cynthia Woods Mitchell Institute for Fundamental Physics and Astronomy, and Department of Physics and Astronomy, Texas A&M University, College Station, Texas 77843, USA*

<sup>68</sup>*Department of Astrophysical Sciences, Princeton University,*

*Peyton Hall, Princeton, New Jersey 08544, USA*

<sup>69</sup>*Institució Catalana de Recerca i Estudis Avançats, E-08010 Barcelona, Spain*

<sup>70</sup>*School of Physics and Astronomy, University of Southampton, Southampton, SO17 1BJ, United Kingdom*

<sup>71</sup>*Computer Science and Mathematics Division, Oak Ridge National Laboratory, Oak Ridge, Tennessee 37831, USA*



(Received 21 June 2021; accepted 1 August 2022; published 15 August 2022)

We constrain cosmological parameters and galaxy-bias parameters using the combination of galaxy clustering and galaxy-galaxy lensing measurements from the Dark Energy Survey (DES) year-3 data. We describe our modeling framework and choice of scales analyzed, validating their robustness to theoretical uncertainties in small-scale clustering by analyzing simulated data. Using a linear galaxy-bias model and redMaGiC galaxy sample, we obtain 10% constraints on the matter density of the Universe. We also implement a nonlinear galaxy-bias model to probe smaller scales that includes parametrization based on hybrid perturbation theory and find that it leads to a 17% gain in cosmological constraining power. We perform robustness tests of our methodology pipeline and demonstrate stability of the constraints to changes in the theory model. Using the redMaGiC galaxy sample as foreground lens galaxies and adopting the best-fitting cosmological parameters from DES year-1 data, we find the galaxy clustering and galaxy-galaxy lensing measurements to exhibit significant signals akin to decorrelation between galaxies and mass on large scales, which is not expected in any current models. This likely systematic measurement error biases our constraints on galaxy bias and the  $S_8$  parameter. We find that a scale-, redshift- and sky-area-independent phenomenological decorrelation parameter can effectively capture this inconsistency between the galaxy clustering and galaxy-galaxy lensing. We trace the source of this correlation to a color-dependent photometric issue and minimize its impact on our result by changing the selection criteria of redMaGiC galaxies. Using this new sample, our constraints on the  $S_8$  parameter are consistent with previous studies and we find a small shift in the  $\Omega_m$  constraints compared to the fiducial redMaGiC sample. We infer the constraints on the mean host-halo mass of the redMaGiC galaxies in this new sample from the large-scale bias constraints, finding the galaxies occupy halos of mass approximately  $1.6 \times 10^{13} M_\odot/h$ .

DOI: [10.1103/PhysRevD.106.043520](https://doi.org/10.1103/PhysRevD.106.043520)

## I. INTRODUCTION

Wide-area imaging surveys of galaxies provide cosmological information through measurements of galaxy clustering and weak gravitational lensing. Galaxies are useful tracers of the full matter distribution, and their spatial clustering is used to infer the matter power spectrum. The shapes of distant galaxies are lensed by the intervening matter, providing a second way to probe the mass distribution. With wide-area galaxy surveys, these two probes of the late-time Universe have provided information on both the geometry and growth of structure in the Universe. In recent years, the combination of two-point correlations—galaxy-galaxy lensing (the cross-correlation of lens galaxy

positions with background source galaxy shear) and the angular autocorrelation of the lens galaxy positions—have been developed in a theoretical framework [1–5] and used to constrain cosmological parameters [6–13]. In practice, two galaxy samples are used: *lens* galaxies tracing the foreground large-scale structure and background *source* galaxies whose shapes are used to infer the lensing shear, and this combination of galaxy-galaxy lensing and galaxy clustering is referred to as “ $2 \times 2$ pt” data vector. This is generally complemented with the two-point of cosmic shear (the lensing shear autocorrelation, referred to as  $1 \times 2$ pt). The Dark Energy Survey (DES) presented cosmological constraints from their year-1 (Y1) dataset from cosmic shear [14] and a joint analysis of all three two-point correlations (henceforth called the “ $3 \times 2$ pt” data vector) [15].

\*shivamp@sas.upenn.edu

This paper is part of a series describing the methodology and results of DES year-3 (Y3)  $3 \times 2\text{pt}$  analysis. The cosmological constraints are presented for cosmic shear [16,17] and the combination of galaxy clustering and galaxy-galaxy lensing using two different lens galaxy samples (this paper and Refs. [18,19]), as well as the  $3 \times 2\text{pt}$  analysis [20]. These cosmological results are enabled by extensive methodology developments at all stages of the analysis from pixels to cosmology, which are referenced throughout. This paper presents the modeling methodology and cosmology inference from DES Y3 galaxy clustering [21] and galaxy-galaxy lensing [22] measurements. We focus on the redMaGiC [23] galaxy sample, described further below. A parallel analysis using a different galaxy sample, the MagLim sample [24], is presented in a separate paper [18].

Incomplete theoretical understanding of the relationship of galaxies to the mass distribution, called galaxy bias, has been a limiting factor in interpreting the lens galaxy autocorrelation function [denoted  $w(\theta)$ ] and galaxy-galaxy lensing [denoted  $\gamma_t(\theta)$ ]. At large scales, galaxy bias can be described by a single number, the linear bias  $b_1$ . On smaller scales, bias is nonlocal and nonlinear, and its description is complicated [25,26]. Perturbation theory (PT) approaches have been developed for quasilinear scales  $\sim 10$  Mpc, though the precise range of scales of its validity is a subtle question that depends on the galaxy population, the theoretical model, and the statistical power of the survey.

With a model for galaxy bias,  $w(\theta)$  and  $\gamma_t$  measurements, together called the “ $2 \times 2\text{pt}$ ” data vector, can probe the underlying matter power spectrum. They are also sensitive to the distance-redshift relation over the redshift range of the lens and source galaxy distributions. These two data vectors constitute a useful subset of the full  $3 \times 2\text{pt}$  data vector, since bias and cosmological parameters can both be constrained [though the uncertainty in galaxy bias would limit either  $w(\theta)$  or  $\gamma_t(\theta)$  individually].

A major part of the modeling and validation involves PT models of galaxy bias and tests using mock catalogs based on  $N$ -body simulations with various schemes of populating galaxies. Approaches based on the halo occupation distribution (HOD) have been widely developed and are used for the DES galaxy samples. For the year-3 (Y3) dataset of DES, two independent sets of mock catalogs have been developed, based on the Buzzard [27] and MICE simulations [28–30].

An interesting recent development in cosmology is a possible disagreement between the inference of the expansion rate and the amplitude of mass fluctuations (denoted  $\sigma_8$ ) and direct measurements or the inference of these quantities in the late-time Universe. The predictions are anchored via measurements of the cosmic microwave background (CMB) and use general relativity and a cosmological model of the Universe to extrapolate to late times. This cosmological model, denoted by  $\Lambda\text{CDM}$ , relies

on two ingredients in the energy budget of the Universe that have yet to be directly detected: cold dark matter (CDM) and dark energy in the form of a cosmological constant denoted as  $\Lambda$ . The experiments that infer the cosmological constraints using the lensing of source galaxies, particularly using the cosmic-shear 2pt correlation, are unable to generally break the degeneracy between  $\Omega_m$  and  $\sigma_8$ . A derived parameter,  $S_8 = \sigma_8(\Omega_m/0.3)^{0.5}$ , is well constrained as it approximately controls the amplitude of the cosmic-shear correlation function. The value of  $S_8$  or  $\sigma_8$  inferred from measurements of cosmic shear and the  $3 \times 2\text{pt}$  data vector [14–17,20,31–33], from galaxy clusters [34,35] and the redshift-space power spectrum [36] tends to be lower than the CMB prediction. The significance of this tension is a work in progress and crucial to the viability of  $\Lambda\text{CDM}$ . The Hubble tension refers to the measured expansion rate being

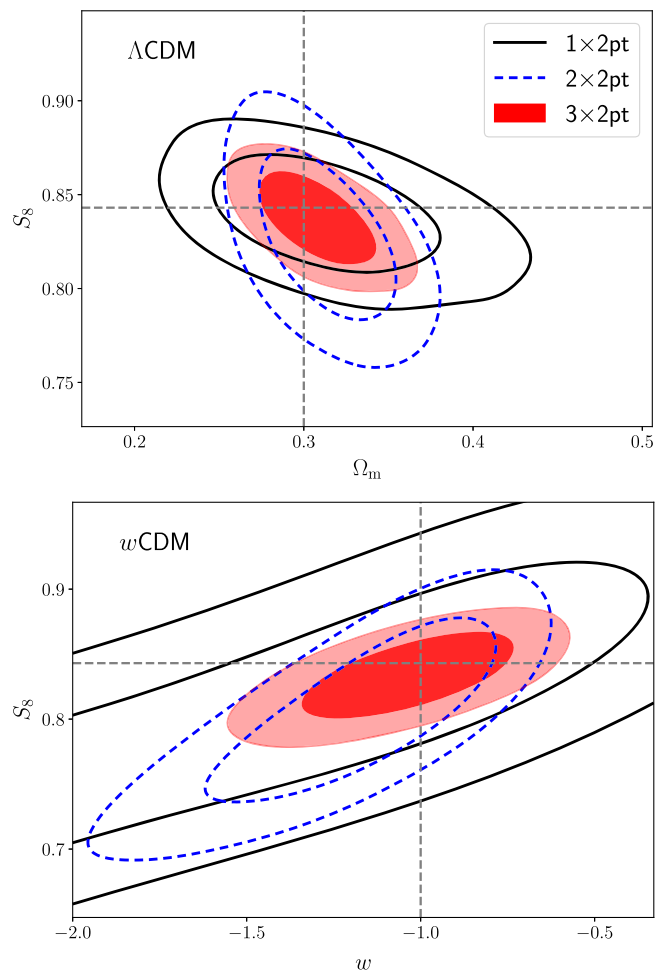


FIG. 1. Comparison of *simulated* constraints on cosmological parameters  $\Omega_m$  and  $S_8$  from cosmic shear alone ( $1 \times 2\text{pt}$ ), galaxy clustering + galaxy-galaxy lensing ( $2 \times 2\text{pt}$ ) and including all three probes ( $3 \times 2\text{pt}$ ). This plot uses a *simulated noiseless baseline data vector* (see Sec. IV B) and shows that  $2 \times 2\text{pt}$  adds complementary information to cosmic-shear constraints, particularly, providing stronger constraints on  $\Omega_m$  and  $w$ .

higher than predicted by the CMB. The resolution of the two tensions, and their possible relationship, is an active area of research in cosmology and provides additional context for the analysis presented here.

Figure 1, based on simulated data, shows the expected constraints on  $S_8$  and  $\Omega_m$  from the  $2 \times 2$ pt data vector and cosmic shear ( $1 \times 2$ pt). It is evident that the two have some complementarity, which enables the breaking of degeneracies in both  $\Lambda$ CDM and  $w$ CDM cosmological models (where  $w$  is the dark energy equation of state parameter and  $w \neq -1$  points toward the departure from the standard  $\Lambda$ CDM model). Particularly noteworthy are the significantly better constraints compared to  $1 \times 2$ pt on the parameter  $w$  and  $\Omega_m$  using  $2 \times 2$ pt in the  $w$ CDM and  $\Lambda$ CDM models, respectively. Note that unlike in  $1 \times 2$ pt, where all the matter in front of source galaxy contributes to its signal,  $2 \times 2$ pt receives contribution only from galaxies within the narrow lens redshift bins. Therefore, we attribute better constraints on these cosmological parameters from  $2 \times 2$ pt to significantly more precise redshifts of the lens galaxy sample. This allows for precise tomographic measurements of  $2 \times 2$ pt data vector which constrains the background geometric parameters like  $w$  and  $\Omega_m$ . With data, these somewhat independent avenues to cosmology provide a valuable cross-check, as the leading sources of systematics are largely different.

The formalism used to compute the  $2 \times 2$ pt data vector is presented in Sec. II. The description of the lens and source galaxy samples, their redshift distributions and measurement methodology of our data vector and its covariance estimation are presented in Sec. III. In Sec. IV we validate our methodology using  $N$ -body simulations and determine the scale cuts for our analysis. Note that in this paper we focus on validation of analysis when using the redMaGiC lens galaxy sample and we refer the reader to Porredon *et al.* [18] for validation of analysis choices for the MagLim sample. The results on data are presented in Sec. V, and we conclude in Sec. VI.

## II. THEORETICAL MODEL

### A. Two-point correlations

Here we describe the hybrid perturbation theory (PT) model used to make theoretical predictions for the two-point statistics  $w(\theta)$  and  $\gamma_t(\theta)$ .

#### 1. Power spectrum

To compute the two-point projected statistics  $w(\theta)$  and  $\gamma_t(\theta)$ , we first describe our methodology of predicting galaxy-galaxy and galaxy-matter power spectra ( $P_{gg}$  and  $P_{gm}$ , respectively). PT provides a framework to describe the distribution of biased tracers of the underlying dark matter field in quasilinear and linear scales. This framework allows for an order-by-order controlled expansion of the overdensity of biased tracer (here galaxies) in terms of the overdensity of the dark matter field where successively higher-order nonlinearities dominate only in successively smaller-scale modes. We will analyze two PT models in this analysis, a hybrid linear bias model (that is complete only at first order) and a hybrid one-loop PT model (that is complete up to third order).

For the linear bias model, we can write the galaxy-matter cross spectrum as  $P_{gm}(k) = b_1 P_{mm}$  and autopower spectrum of the galaxies as  $P_{gg}(k) = b_1^2 P_{mm}(k)$ . Here  $b_1$  is the linear bias parameter and  $P_{mm}(k)$  is the *nonlinear* power spectrum of the matter field. We use the nonlinear matter power spectrum prediction from Takahashi *et al.* [37] to model  $P_{mm}(k)$  (referred to as Halofit hereafter). We use the Bird, Viel, and Haehnelt [38] prescription to model the impact of massive neutrinos in this Halofit fitting formula. We refer the reader to Krause *et al.* [39] for robustness of our results despite the limitations of these modeling choices (cf. [40] for an alternative modeling scheme).

In the hybrid one-loop PT model used here,  $P_{gm}$  and  $P_{gg}$  can be expressed as

$$P_{gm}(k, z) = b_1 P_{mm}(k, z) + \frac{1}{2} b_2 P_{b_1 b_2}(k, z) + \frac{1}{2} b_s P_{b_1 s^2}(k, z) + \frac{1}{2} b_{3nl} P_{b_1 b_{3nl}}(k, z) + b_k k^2 P_{mm}(k, z), \quad (1)$$

$$P_{gg}(k, z) = b_1^2 P_{mm}(k, z) + b_1 b_2 P_{b_1 b_2}(k, z) + b_1 b_s P_{b_1 s^2}(k, z) + b_1 b_{3nl} P_{b_1 b_{3nl}}(k, z) + \frac{1}{4} b_2^2 P_{b_2 b_2}(k, z) + \frac{1}{2} b_2 b_s P_{b_2 s^2}(k, z) + \frac{1}{4} b_s^2 P_{s^2 s^2}(k, z) + 2b_1 b_k k^2 P_{mm}(k, z). \quad (2)$$

Here the parameters  $b_1$ ,  $b_2$ ,  $b_s$ ,  $b_{3nl}$  and  $b_k$  are the renormalized bias parameters [41]. The kernels  $P_{b_1 b_2}$ ,  $P_{b_1 s^2}$ ,  $P_{b_1 b_{3nl}}$ ,  $P_{b_2 b_2}$ ,  $P_{b_2 s^2}$  and  $P_{s^2 s^2}$  are described in Saito *et al.* [42] and are calculable from the linear matter power spectrum. We validated this model in Pandey *et al.* [43] using 3D correlation functions,  $\xi_{gg}$  and  $\xi_{gm}$ , of redMaGiC

galaxies measured in DES-like MICE simulations [28–30]. These configuration space statistics are the Fourier transforms of the power spectra mentioned above. We found this model to describe the high signal-to-noise 3D measurements on the simulations above scales of 4 Mpc/ $h$  and redshift  $z < 1$  with a reduced  $\chi^2$  consistent with one.

Our tests also showed that, at the projected precision of this analysis, two of the nonlinear bias parameters ( $b_s$  and  $b_{3nl}$ ) can be fixed to their coevolution values given by  $b_s = (-4/7)(b_1 - 1)$  and  $b_{3nl} = (b_1 - 1)$ ; while  $b_k$  can be fixed to zero. We will use this result as our *fiducial* modeling choice for the one-loop PT model.

We note that there are alternative ways of modeling the scale-dependent nonlinear biasing of galaxies. For example, Simon and Hilbert [44] used a template fitting procedure using the Millennium simulation suite [45], using a semianalytic galaxy model [46] and obtaining a significantly higher resolution of interhalo physics. However, in order to validate the bias model on the scales above 4 Mpc/h on mock catalogs, the simulation volume (to minimize cosmic variance) and realistic galaxy selection are more important than resolution within individual halos. Due to the larger volume of the Buzzard flock compared to the Millennium simulation, and detailed DES galaxy selection modeling in Buzzard and MICE, we believe that the bias modeling validation performed in Pandey *et al.* [43] (and in Sec. IV C) is more direct (not affected by model imperfections of an intermediate fitting function), more stringent (due to lower cosmic variance) and more specific (due to DES-specific galaxy selection). Finally, as described in Goldstein *et al.* [47], our two-parameter model also fits the 3D correlations measurements between matter and galaxy catalogs at various limiting magnitudes at 2% level, in both configuration and Fourier spaces in a high-resolution simulation suite.

## 2. Angular correlations

In order to calculate our observables  $w(\theta)$  and  $\gamma_l(\theta)$ , we project the 3D power spectra described above to angular space. The projected galaxy clustering and galaxy-galaxy lensing angular power spectra of tomography bins  $i, j$  are given by

$$C_{AB}^{ij}(\ell) = \frac{2}{\pi} \int d\chi_1 W_A^i(\chi_1) \int d\chi_2 W_B^j(\chi_2) \times \int dk k^2 P_{AB}[k, z(\chi_1), z(\chi_2)] j_\ell(k\chi_1) j_\ell(k\chi_2), \quad (3)$$

$$C_{gg}^{ij}(\ell) = \int d\chi \frac{W_g^i(\chi) W_g^j(\chi)}{\chi^2} \left[ P_{gg} \left( \frac{\ell + 0.5}{\chi}, \chi \right) - b_1^i b_1^j P_{lin} \left( \frac{\ell + 0.5}{\chi}, \chi \right) \right] + \frac{2}{\pi} \int d\chi_1 b_1^i W_g^i(\chi_1) D[z(\chi_1)] \int d\chi_2 b_1^j W_g^j(\chi_2) D[z(\chi_2)] \int \frac{dk}{k} k^3 P_{lin}(k, 0) j_\ell(k\chi_1) j_\ell(k\chi_2), \quad (6)$$

where  $D(z(\chi))$  is the growth factor and  $P_{lin}$  is the linear matter power spectrum. The full model of galaxy clustering, including the contributions from other modeling ingredients like redshift-space distortions and lens

where  $AB = gg$  models galaxy clustering and  $AB = g\kappa$ , where  $\kappa$  denotes the convergence field, models galaxy-galaxy lensing. Here  $W_g^i(\chi) = n_g^i(z(\chi)) dz/d\chi$  is the normalized radial selection function of lens galaxies for tomographic bin  $i$ , and  $W_\kappa^i$  is the tomographic lensing efficiency of the source sample

$$W_\kappa^i(\chi) = \frac{3\Omega_m H_0^2}{2} \int_\chi^\infty d\chi' n_s^i[z(\chi')] \frac{\chi}{a(\chi)} \frac{\chi' - \chi}{\chi'}, \quad (4)$$

with  $n_{g/s}^i(z)$  the normalized redshift distribution of the lens or source galaxies in tomography bin  $i$ . For the galaxy-galaxy lensing observable, we use the Limber approximation [48,49] which simplifies Eq. (3) to

$$C_{g\kappa}^{ij}(\ell) = \int d\chi \frac{W_g^i(\chi) W_\kappa^j(\chi)}{\chi^2} P_{g\kappa} \left[ k = \frac{\ell + 1/2}{\chi}, z(\chi) \right]. \quad (5)$$

In the absence of other modeling ingredients that are described in the next section, we have  $C_{g\kappa}^{ij}(\ell) \equiv C_{gm}^{ij}(\ell)$  (similarly  $P_{g\kappa} \equiv P_{gm}$ ). As described in Fang *et al.* [50], even at the accuracy beyond this analysis, it is sufficient to use the Limber approximation for the galaxy-galaxy lensing observable, while for galaxy clustering this may cause significant cosmological parameter biases.

To evaluate galaxy clustering statistics using Eq. (3), we split the predictions into small and large scales. The non-Limber correction is only significant on large scales where nonlinear contributions to the matter power spectra as well as galaxy biasing are subdominant. Therefore we use the Limber approximation for the small-scale nonlinear corrections and use non-Limber corrections strictly on large scales using linear theory. Schematically, i.e., ignoring contributions from redshift-space distortions and lens magnification (see [39] for details), the galaxy clustering angular power spectrum between tomographic bins  $i$  and  $j$  is given by

magnification that we describe below, is detailed in Fang *et al.* [50] and Krause *et al.* [39].

The real-space projected statistics of interest can be obtained from these angular correlations via

$$w^{ij}(\theta) = \sum \frac{2\ell + 1}{4\pi} \overline{P}_\ell[\cos(\theta)] C_{\text{gg}}^{ij}(\ell), \quad (7)$$

$$\gamma_t^{ij}(\theta) = \sum \frac{2\ell + 1}{4\pi\ell(\ell + 1)} \overline{P}_\ell^2[\cos(\theta)] C_{\text{gk}}^{ij}(\ell), \quad (8)$$

where  $\overline{P}_\ell$  and  $\overline{P}_\ell^2$  are bin-averaged Legendre polynomials (see Friedrich *et al.* [51] for exact expressions).

## B. The rest of the model

To describe the statistics measured from data, we have to model various other physical phenomena that contribute to the signal to obtain unbiased inferences. In this section, we describe the leading sources of these modeling systematics. We have also validated in Krause *et al.* [39] that higher-order corrections do not bias our results.

### 1. Intrinsic alignment

Galaxy-galaxy lensing aims to isolate the percent-level coherent shape distortions, or shear, of background source galaxies due to the gravitational potential of foreground lens galaxies. The local environment, however, including the gravitational tidal field, can also impact the intrinsic shapes of source galaxies and contribute to the measured shear signal. This interaction between the source galaxies and their local environment, generally known as ‘‘intrinsic alignments’’ (IA), is nonrandom. When there is a nonzero overlap between the source and lens redshift distributions, IA can have a nonzero contribution to the galaxy-galaxy lensing signal. To account for this effect, we model IAs using the ‘‘tidal alignment and tidal torquing’’ (TATT) model [52]. Ignoring higher-order effects, such as lens magnification (see [19,22]), IA contributes to the galaxy-shear angular power spectra through the correlation of lens density and the  $E$ -mode component of intrinsic source shapes:  $C_{\text{gk}}^{ij}(\ell) \rightarrow C_{\text{gk}}^{ij}(\ell) + C_{\text{gIE}}^{ij}(\ell)$ . The  $C_{\text{gIE}}^{ij}(\ell)$  term is detailed in Krause *et al.* [39], Secco *et al.* [17], Prat *et al.* [22], and Blazek *et al.* [52]. Within our implementation of the TATT framework,  $C_{\text{gIE}}^{ij}(\ell)$  for all tomographic bin combinations  $i$  and  $j$  can be expressed using five IA parameters— $a_1$  and  $a_2$  (normalization of linear and quadratic alignments);  $\alpha_1$  and  $\alpha_2$  (their respective redshift evolution); and  $b_{\text{ta}}$  (normalization of a density-weighting term)—and the linear lens galaxy bias. Therefore this model captures higher-order contributions to the intrinsic alignment of source galaxies as compared to the simpler nonlinear linear alignment (NLA) model that was used in the DES Y1 analysis [15,53–55]. In principle, there are also contributions at one-loop order in PT involving the nonlinear galaxy bias and nonlinear IA terms. However, in this analysis, we neglect these terms as we expect them to be subdominant, and they can be largely captured through the free  $b_{\text{ta}}$  parameter (see Blazek *et al.* [56] for further discussion of these terms).

## 2. Magnification

All the matter between the observed galaxy and the observer acts as a gravitational lens. Hence, the galaxies get magnified, increasing the size of galaxy images (parametrized by the magnification factor  $\mu$ ) and increasing their total flux. The galaxy magnification decreases the observed number density due to stretching of the local sky, whereas increasing the total flux results in an increase in number density (as intrinsically fainter galaxies, which are more numerous, can be observed). This changes the galaxy-galaxy angular power spectrum to  $C_{\text{gg}}^{ij}(\ell) \rightarrow C_{\text{gg}}^{ij}(\ell) + 2C_{\mu\text{g}}^{ij}(\ell) + C_{\mu\mu}^{ij}(\ell)$  and the galaxy-shear angular power spectrum to  $C_{\text{gk}}^{ij}(\ell) \rightarrow C_{\text{gk}}^{ij}(\ell) + C_{\mu\text{IE}}^{ij}(\ell) + C_{\mu\text{k}}^{ij}(\ell)$ . The auto- and cross-power spectra with magnification are again given by Eq. (3). For example,  $C_{\mu\text{g}}^{ij}(\ell) = 2(\mu^i - 1)C_{\text{gk}}^{ij}(\ell)$ , where, as described below, we fix  $\mu^i$  for the five tomographic bins to [1.31, −0.52, 0.34, 2.25, 1.97]. We refer the reader to Krause *et al.* [39] for the detailed description of the equations for each of the power spectra.

The magnification coefficients are computed with the BALROG image simulations [57,58] in a process described in Elvin-Poole *et al.* [19]. Galaxy profiles are drawn from the DES deep fields [59] and injected into real DES images [60]. The full photometry pipeline [61] and redMaGiC sample selection are applied to the new images to produce a simulated redMaGiC sample with the same selection effects as the real data. To compute the impact of magnification, the process is repeated, this time applying a constant magnification to each injected galaxy. The magnification coefficients are then derived from the fractional increase in number density when magnification is applied. This method captures both the impact of magnification on the galaxy magnitudes and the galaxy sizes, including all numerous sample selection effects. A similar procedure is repeated to estimate the magnification coefficients for the MagLim sample. We refer the reader to Elvin-Poole *et al.* [19] for further details about the impact of magnification on our observable and their constraints from data.

### 3. Nonlocality of galaxy-galaxy lensing

The configuration-space estimate of the galaxy-galaxy lensing signal is a nonlocal statistic. The galaxy-galaxy lensing signal of source galaxy at redshift  $z_s$  by matter around the galaxy at redshift  $z_l$  at transverse distance  $R$  is related to the mass density of matter around the lens galaxy by

$$\gamma_t(R; z_g, z_s) = \frac{\Delta\Sigma(R; z_g)}{\Sigma_{\text{crit}}(z_g, z_s)}, \quad (9)$$

where  $\Sigma_{\text{crit}}$  is the critical surface mass density given by

$$\Sigma_{\text{crit}}(z_g, z_s) = \frac{c^2}{4\pi G} \frac{D_A(z_s)}{D_A(z_g)D_A(z_g, z_s)}. \quad (10)$$

Here  $D_A$  is the angular diameter distance,  $z_l$  is the redshift of the lens and  $z_s$  is the redshift of the source. In Eq. (9),  $\Delta\Sigma(R; z_g) = \bar{\Sigma}(0, R; z_g) - \Sigma(R; z_g)$ ,  $\Sigma(R; z_g)$  is the surface mass density at a transverse separation  $R$  from the lens and  $\bar{\Sigma}(0, R)$  is the average surface mass density within a separation  $R$  from that lens. Through the  $\bar{\Sigma}(0, R)$  term,  $\gamma_t$  at any scale  $R$  is dependent on the mass distribution at all scales less than  $R$ . This makes  $\gamma_t$  highly nonlocal, and any model that is valid only on large scales above some  $r_{\min}$  will break down more rapidly than for a more local statistic like  $w(\theta)$ . However, as the dependence on small scales is through the *mean* surface mass density, the impact of the mass distribution inside  $r_{\min}$  on  $\gamma_t(\theta)$  can be written as

$$\gamma_t(R; z_g, z_s) = \frac{1}{\Sigma_{\text{crit}}(z_g, z_s)} \left[ \Delta\Sigma_{\text{model}}(z_g) + \frac{B(z_g)}{R^2} \right], \quad (11)$$

where  $\Delta\Sigma^{\text{model}}$  is the prediction from a model (which is given by PT here) that is valid on scales above  $r_{\min}$  (also see [2]). Here,  $B$  is the effective total residual mass below  $r_{\min}$  and is known as the point-mass (PM) parameter. In this analysis we use the thin redshift bin approximation (see Appendix A for details of this validation) and hence the average  $\gamma_t$  signal between lens bin  $i$  and source bin  $j$  can be written as

$$\gamma_t^{ij} = \gamma_{t,\text{model}}^{ij} + G^{ij}/\theta^2, \quad (12)$$

where

$$G^{ij} = B^i \int dz_g dz_s n_g^i n_s^j \Sigma_{\text{crit}}^{-1}(z_g, z_s) \chi^{-2}(z_g) \equiv B^i \beta^{ij}. \quad (13)$$

Here  $B^i$  is the PM for lens bin  $i$ ,  $n_g^i$  is the redshift distribution of lens galaxies for tomographic bin  $i$ , and  $n_s^j$  is the redshift distribution of source galaxies for tomographic bin  $j$ .

However, instead of directly sampling over the parameters  $B^i$  for each tomographic bin, we implement an analytic marginalization scheme as described in MacCrann *et al.* [62]. We modify our inverse covariance when calculating the likelihood as described in Sec. III D 2. We note that this scheme of adding and marginalizing over the PM parameters is equivalent to alternative procedures [63,64] for mitigating the impact of unmodeled nonlinear small-scale physics to the large scales.

### III. DATA DESCRIPTION

#### A. DES Y3

The full DES survey was completed in 2019 using the Cerro Tololo Inter-American Observatory 4-m Blanco telescope in Chile and covered approximately 5000 square degrees of the South Galactic Cap. This 570-megapixel dark energy camera [65] images the field in five broadband

filters, grizY, which span the wavelength range from approximately 400 to 1060 nm. The raw images are processed by the DES data management team [66,67] and after a detailed object selection criteria on the first three years of imaging data (detailed in Abbott *et al.* [15]), the Y3 GOLD dataset containing 400 million sources is constructed (single-epoch and coadd images are available [68] as data release 1). We further process this GOLD dataset to obtain the lens and source catalogs described in the following subsections.

#### 1. redMaGiC lens galaxy sample

The principal lens sample used in this analysis is selected with the redMaGiC algorithm [23] run on DES year-3 data. redMaGiC selects luminous red galaxies according to the magnitude-color-redshift relation of red-sequence galaxies, calibrated using an overlapping spectroscopic sample. This procedure is based on selecting galaxies above a threshold luminosity that fit (using  $\chi_{\text{RM}}^2$  as goodness-of-fit criteria) this redMaGiC template of magnitude-color-redshift relation to a threshold better than  $\chi_{\text{RM}}^2 < \chi_{\text{max}}^2$ . The value of  $\chi_{\text{max}}^2$  is chosen such that the sample has a constant comoving space density and is typically less than 3. The full redMaGiC algorithm is described in Rozo *et al.* [23], and after application of this algorithm to DES Y3 data, we have approximately 2.6 million galaxies.

Rodríguez-Monroy *et al.* [21] found that the redMaGiC number density fluctuates with several observational properties of the survey, which imprints a noncosmological bias into the galaxy clustering. To account for this we assign a weight to each galaxy, which corresponds to the inverse of the angular selection function at that galaxy's location. The computation and validation of these weights are described in Rodríguez-Monroy *et al.* [21].

#### 2. MagLim lens galaxy sample

DES cosmological constraints are also derived using a second lens sample, MagLim, selected by applying the criterion  $i < 4z + 18$  to the GOLD catalog, where  $z$  is the photometric redshift estimate given by the directional neighborhood fitting (DNF) algorithm [69]. This selection is shown by Porredon *et al.* [24] to be optimal in terms of its  $2 \times 2$ pt cosmological constraints. We additionally apply a lower magnitude cut,  $i > 17.5$ , to remove contamination from bright objects. The resulting sample has about 10.7 million galaxies.

Similarly to redMaGiC, we correct the impact of observational systematics on the MagLim galaxy clustering by assigning a weight to each galaxy, as described and validated in Rodríguez-Monroy *et al.* [21]. This sample is then used in Porredon *et al.* [18] to obtain cosmological constraints from the combination of galaxy clustering and galaxy-galaxy lensing from DES Y3 data. We refer to Porredon *et al.* [18] for a detailed description of the sample and its validation.



### 3. Source galaxy shape catalog

To estimate the weak lensing shear of the observed source galaxies, we use the Metacalibration algorithm [70,71]. This method estimates the response of a shear estimator to artificially sheared galaxy images and incorporates improvements like better point-spread function (PSF) estimation [72], better astrometric methods [61] and inclusion of inverse variance weighting. The details of the method applied to our galaxy sample are presented in Gatti *et al.* [73]. This methodology does not capture the object-blending effects and shear-dependent detection biases and we use image simulations to calibrate this bias as detailed in MacCrann *et al.* [74]. The galaxies that pass the selection cuts designed to reduce systematic biases (as detailed in Gatti *et al.* [73]) are used to make our source sample shape catalog. This catalog consists of approximately 100 million galaxies with an effective number density of  $n_{\text{eff}} = 5.6$  galaxies per arcmin<sup>2</sup> and an effective shape noise of  $\sigma_e = 0.26$ .

#### B. Buzzard simulations

The Buzzard simulations are  $N$ -body light cone simulations that have been populated with galaxies using the Addgals algorithm [75], endowing each galaxy with positions, velocities, spectral energy distributions, broadband photometry, half-light radii and ellipticities. In order to build a light cone that spans the entire redshift range covered by DES Y3 galaxies, we combine three light cones constructed from simulations with box sizes of 1.05, 2.6 and  $4.0(h^{-3} \text{Gpc}^3)$ , mass resolutions of  $3.3 \times 10^{10}$ ,  $1.6 \times 10^{11}$ , and  $5.9 \times 10^{11} h^{-1} M_{\odot}$ , spanning redshift ranges  $0.0 < z \leq 0.32$ ,  $0.32 < z \leq 0.84$  and  $0.84 < z \leq 2.35$ , respectively. Together these produce 10000 square degrees of unique light cone. The light cones are run with the L-Gadget2  $N$ -body code, a memory optimized version of Gadget2 [45], with initial conditions generated using 2LPTIC at  $z = 50$  [76]. From each 10000 square degree catalog, we can create two DES Y3 footprints.

The Addgals model uses the relationship,  $P(\delta_R|M_r)$ , between a local density proxy  $\delta_R$  and absolute magnitude  $M_r$ , measured from a high-resolution subhalo abundance matching (SHAM) model in order to populate galaxies into these light cone simulations. The Addgals model reproduces the absolute-magnitude-dependent clustering of the SHAM. Additionally, we employ a conditional abundance matching model, assigning redder spectral energy distributions (SEDs) to galaxies that are closer to massive dark matter halos, in a manner that allows us to reproduce the color-dependent clustering measured in the Sloan Digital Sky Survey main galaxy sample [75,77].

These simulations are ray-traced using the spherical-harmonic transform (SHT) configuration of CALCLENS, where the SHTs are performed on an  $N_{\text{side}} = 8192$  HealPix grid [78]. The lensing distortion tensor is computed at each

galaxy position and is used to deflect the galaxy angular positions, apply shear to galaxy intrinsic ellipticities, including effects of reduced shear, and magnify galaxy shapes and photometry. We have conducted convergence tests of this algorithm and found that resolution effects are negligible on the scales used for this analysis [27].

Once the simulations have been ray-traced, we apply DES Y3-specific masking and photometric errors. To mask the simulations, we employ the Y3 footprint mask but do not apply the bad region mask [61], resulting in a footprint with an area of 4143.17 square degrees. Each set of three  $N$ -body simulations yields two Y3 footprints that contain 520 square degrees of overlap. In total, we use 18 Buzzard realizations in this analysis.

We apply a photometric error model to simulate wide-field photometric errors in our simulations. To select a lens galaxy sample, we run the redMaGiC galaxy selection on our simulations using the same configuration as used in the Y3 data, as described in Rodríguez-Monroy *et al.* [21]. A weak lensing source selection is applied to the simulations using PSF-convolved sizes and  $i$ -band SNR to match the nontomographic source number density,  $5.9 \text{ arcmin}^{-2}$ , from the Metacalibration source catalog. This matching was performed using a slightly preliminary version of the Metacalibration catalog, so this number density is slightly different from the final Metacalibration catalog that is used in our DES Y3 analyses. We employ the fiducial redshift estimation framework (see Sec. III C 3) to our simulations in order to place galaxies into four source redshift bins with number densities of  $1.46 \text{ arcmin}^{-2}$  each. Once binned, we match the shape noise of the simulations to that measured in the Metacalibration catalog per tomographic bin, yielding shape noise values of  $\sigma_e = [0.247, 0.266, 0.263, 0.314]$ .

Two-point functions are measured in the Buzzard simulations using the same pipeline used for the DES Y3 data, where we set Metacalibration responses and inverse variance weights equal to 1 for all galaxies, as these are not assigned in our simulation framework. We have opted to make measurements without shape noise in order to reduce the variance in the simulated analyses using these measurements. Lens galaxy weights are produced in a manner similar to that done in the data and applied to measure our clustering and lensing signals. The clustering and galaxy-galaxy lensing predictions match the DES redMaGiC measurements to 10%–20% accuracy over most scales and tomographic bins, except for the first lens bin, which disagrees by 50% in  $w(\theta)$ . We refer the reader to Fig. 4 in DeRose *et al.* [79] for a more detailed comparison.

#### C. Tomography and measurements

In this section we detail the estimation of the photometric redshift distribution of our source galaxy sample and two lens galaxy samples. These three samples are qualitatively different and have different redshift attributes, requiring different redshift calibration methods detailed below.

### 1. redMaGiC redshift methodology

We split the redMaGiC sample into  $N_{z,g} = 5$  tomographic bins, selected on the redMaGiC redshift point estimate quantity ZREDMAGIC. The bin edges used are  $z = 0.15, 0.35, 0.50, 0.65, 0.80, 0.90$ . The first three bins use a luminosity threshold of  $L_{\min} > 0.5L_*$  and are known as the high-density sample. The last two redshift bins use a luminosity threshold of  $L_{\min} > 1.0L_*$  and are known as the high-luminosity sample. The galaxy number densities (in the units of  $\text{arcmin}^{-2}$ ) for the five tomographic bins are  $\langle n_g \rangle = 0.022, 0.038, 0.059, 0.03, 0.025$ .

The redshift distributions are computed by stacking four samples from the probability density function (PDF) of each redMaGiC galaxy, allowing for non-Gaussianity of the PDF. We find an average individual redshift uncertainty of  $\sigma_z/(1+z) < 0.0126$  in the redshift range used from the variance of these samples. We refer the reader to Rozo *et al.* [23] for more details on the algorithm of redshift assignment for redMaGiC galaxies and to Cawthon *et al.* [80] for more details on the calibration of redshift distribution of the Y3 redMaGiC sample.

### 2. MagLim redshift methodology

We use DNF [69] for splitting the MagLim sample into tomographic bins and estimating the redshift distributions. DNF uses a training set from a spectroscopic database as reference and then provides an estimate of the redshift of the object through a nearest-neighbor fit in a hyperplane in color and magnitude space.

We split the MagLim sample into  $N_{z,g} = 6$  tomographic bins from  $z = 0.2$  and  $z = 1.05$ , selected using the DNF photometric redshift estimate. The bin edges are  $[0.20, 0.40, 0.55, 0.70, 0.85, 0.95, 1.05]$ . The galaxy number densities (in units of  $\text{arcmin}^{-2}$ ) for the six tomographic bins of this sample are  $\langle n_g \rangle = 0.15, 0.107, 0.109, 0.146, 0.106, 0.1$ . The redshift distributions in each bin are then computed by stacking the DNF PDF estimates of each MagLim galaxy. See Porredon *et al.* [18] for a more comprehensive description and validation of this methodology and Giannini *et al.* [81] for estimation of redshift distributions of this sample using the same methodology as used for source galaxies that is described below.

### 3. Source redshift methodology

The description of the tomographic bins of source samples and the methodology for calibrating their photometric redshift distributions are summarized in Myles *et al.* [82]. Overall, the redshift calibration methodology involves the use of self-organizing maps [82], clustering redshifts [83] and shear-ratio [84] information. The self-organizing map photometric redshift (SOMPZ) methodology leverages additional photometric bands in the DES deep-field observations [59] and the BALROG simulation software [85] to characterize a mapping between color space and

redshifts. This mapping is then used to provide redshift distribution samples in the wide field, after including the uncertainties from sample variance and galaxy flux measurements in a way that is not subject to selection biases. The clustering redshift methodology performs the calibration by analyzing cross-correlations between redMaGiC and spectroscopic data from Baryon Acoustic Oscillation Survey (BOSS) and its extension (eBOSS). Candidate  $n_s(z)$  distributions are drawn from the posterior distribution defined by the combination of SOMPZ and clustering-redshift likelihoods. These two approaches provide us the mean redshift distribution of source galaxies and uncertainty in this distribution. The shear-ratio calibration uses the ratios of small-scale galaxy-galaxy lensing data, which are largely independent of the cosmological parameters but help calibrate the uncertainties in the redshift distributions. We include it downstream in our analysis pipeline as an external likelihood, as briefly described in Sec. III C 5 and detailed in Sánchez *et al.* [84].

Finally, we split the source catalog into  $N_{z,s} = 4$  tomographic bins. The mean redshift distribution of redMaGiC lens galaxies and source galaxies are compared in Fig. 2. We refer the reader to Porredon *et al.* [18] for MagLim sample redshift distribution.

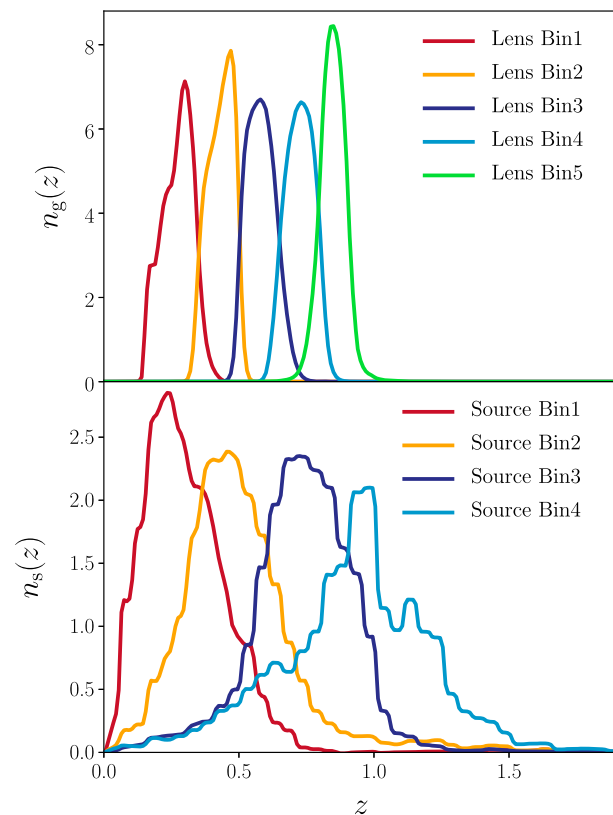


FIG. 2. Comparison of the normalized redshift distributions of various tomographic bins of the source galaxies and redMaGiC lens galaxies in the data.

#### 4. 2pt measurements

For galaxy clustering, we use the Landy-Szalay estimator [86] given as

$$w(\theta) = \frac{DD - 2DR + RR}{RR}, \quad (14)$$

where  $DD$ ,  $DR$  and  $RR$  are normalized weighted number counts of galaxy-galaxy, galaxy-random and random-random pairs, respectively, within angular and tomographic bins. For lens tomographic bins, we measure the autocorrelations in  $N_\theta = 20$  log-spaced angular bins ranging from 2.5 to 250 arcmin. Each lens galaxy in the catalog ( $g_i$ ) is weighted with its systematic weight  $w_{g_i}$ . This systematic weight aims to remove the large-scale fluctuations due to changing observing conditions at the telescope and Galactic foregrounds. Our catalog of randoms is 40 times larger than the galaxy catalog. The validation of this estimator and systematic weights of the lens galaxies is presented in Rodríguez-Monroy *et al.* [21]. In total we have  $N_{w(\theta)} = N_{z,g} \times N_\theta = 100$  measured  $w(\theta)$  data points.

The galaxy-galaxy lensing estimator used in this analysis is given by

$$\gamma_t(\theta) = \frac{\sum_k w_{r_k} \sum_{ij} w_{g_i} w_{s_j} e_{t,ij}^{\text{LS}}}{\sum_i w_{g_i} \sum_{kj} w_{r_k} w_{s_j}} - \frac{\sum_{kj} w_{r_k} w_{s_j} e_{t,kj}^{\text{RS}}}{\sum_{kj} w_{r_k} w_{s_j}}, \quad (15)$$

where  $e_{t,ij}^{\text{LS}}$  and  $e_{t,kj}^{\text{RS}}$  are the measured tangential ellipticity of source galaxy  $j$  around lens galaxy  $i$  and random point  $k$ , respectively. The weight  $w_{g_i}$  is the systematic weight of the lens galaxy as described above,  $w_{r_k}$  is the weight of random point that we fix to 1 and  $w_{s_j}$  is the weight of the source galaxy that is computed from inverse variance of the shear response weighted ellipticity of the galaxy (see Gatti *et al.* [73] for details). This estimator has been detailed and validated in Singh *et al.* [87] and Prat *et al.* [22]. We measure this signal for each pair of lens and source tomographic bins and hence in total we have  $N_{\gamma_t(\theta)} = N_{z,g} \times N_{z,s} \times N_\theta = 400$  measured  $\gamma_t(\theta)$  data points.

We analyze both of these measured statistics jointly and hence we have in total  $N_{\text{data}} = N_{w(\theta)} + N_{\gamma_t(\theta)} = 500$  data points. Our measured signal to noise (SNR),<sup>1</sup> using redMaGiC lens sample, of  $w(\theta)$  is 171 [21] and of  $\gamma_t(\theta)$  is 121 [22], giving a total joint total SNR of 196. In Sec. IV, we describe and validate different sets of scale cuts for the linear bias model [angular scales corresponding to (8, 6) Mpc/ $h$  for  $w(\theta)$  and  $\gamma_t(\theta)$ , respectively] and the nonlinear bias model [(4, 4) Mpc/ $h$ ]. After applying these scale cuts, we obtain the joint SNR, that we analyze for

<sup>1</sup>The SNR is calculated as  $\sqrt{(\vec{\mathcal{D}}\mathcal{C}^{-1}\vec{\mathcal{D}})}$ , where  $\vec{\mathcal{D}}$  is the data under consideration and  $\mathcal{C}$  is its covariance.

cosmological constraints, as 81 for the linear bias model and 106 for the nonlinear bias model.<sup>2</sup>

#### 5. Shear ratios

As will be detailed in Sec. IV A 3, in this analysis, we remove the small scales' nonlinear information from the 2pt measurements that are presented in the above subsection. However, as presented in Sánchez *et al.* [84], the ratio of  $\gamma_t(\theta)$  measurements for the same lens bin but different source bins is well described by our model (see Sec. II) even on small scales. Therefore we include these ratios (referred to as shear ratio henceforth) as an additional independent dataset in our likelihood. In this shear-ratio data vector, we use the angular scales above 2 Mpc/ $h$  and less than our fiducial scale cuts for 2pt measurements described in Sec. IV A 3 (we also leave two data points between 2pt scale cuts and shear-ratio scale cuts to remove any potential correlations between the two). The details of the analysis choices for shear-ratio measurements and the corresponding covariance matrix are detailed in Sánchez *et al.* [84] and DES Collaboration [20].

#### D. Covariance

In this analysis, the covariance between the statistic  $w(\theta)$  and  $\gamma_t(\theta)$  ( $\mathcal{C}$ ) is modeled as the sum of a Gaussian term ( $\mathcal{C}_G$ ), trispectrum term ( $\mathcal{C}_{\text{NG}}$ ) and supersample covariance term ( $\mathcal{C}_{\text{SSC}}$ ). The analytic model used to describe ( $\mathcal{C}_G$ ) is described in Friedrich *et al.* [51]. The terms  $\mathcal{C}_{\text{NG}}$  and  $\mathcal{C}_{\text{SSC}}$  are modeled using a halo model framework as detailed in Krause and Eifler [88] and Krause *et al.* [55]. The covariance calculation has been performed using the CosmoCov package [89], and the robustness of this covariance matrix has been tested and detailed in Friedrich *et al.* [51]. We also account for two additional sources of uncertainties that are not included in our fiducial model using the methodology of analytical marginalization [90] as detailed below.

#### I. Accounting for large scale structure (LSS) systematics

As described in Rodríguez-Monroy *et al.* [21], we modify the  $w(\theta)$  covariance to analytically marginalize over two sources of uncertainty in the correction of survey systematics: the choice of correction method and the bias of the fiducial method as measured on simulations.

These systematics are modeled as

$$w'(\theta) = w(\theta) + A_1 \Delta w_{\text{method}}(\theta) + A_2 w_{\text{r.s. bias}}(\theta), \quad (16)$$

where  $\Delta w_{\text{method}}(\theta)$  is the difference between two systematics correction methods: iterative systematic

<sup>2</sup>Using a more optimal SNR estimator,  $\text{SNR} = \frac{(\vec{\mathcal{D}}^{\text{data}}\mathcal{C}^{-1}\vec{\mathcal{D}}^{\text{model}})}{\sqrt{(\vec{\mathcal{D}}^{\text{model}}\mathcal{C}^{-1}\vec{\mathcal{D}}^{\text{model}})}}$ , where  $\vec{\mathcal{D}}^{\text{data}}$  is the measured data and  $\vec{\mathcal{D}}^{\text{model}}$  is the best-fit model, we get SNR = 79.5 for the linear bias model scale cuts of (8, 6) Mpc/ $h$ .

decontamination (ISD) and elastic net, and  $w_{\text{r.s. bias}}(\theta)$  is the residual systematic bias measured on log-normal mocks. Both terms are presented in detail in Rodríguez-Monroy *et al.* [21]. Also note that here  $A_1$  and  $A_2$  are arbitrary amplitudes.

TABLE I. The parameters varied in different models, their prior range used ( $\mathcal{U}[X, Y] \equiv$  Uniform prior between  $X$  and  $Y$ ;  $\mathcal{G}[\mu, \sigma] \equiv$  Gaussian prior with mean  $\mu$  and standard deviation  $\sigma$ ) in this analysis and the fiducial values used for simulated likelihood tests.

Model	Parameter	Prior	Fiducial	
Cosmology				
Common parameters	$\Omega_m$	$\mathcal{U}[0.1, 0.9]$	0.3	
	$A_s \times 10^{-9}$	$\mathcal{U}[0.5, 5]$	2.19	
	$\Omega_b$	$\mathcal{U}[0.03, 0.07]$	0.048	
	$n_s$	$\mathcal{U}[0.87, 1.06]$	0.97	
	$h$	$\mathcal{U}[0.55, 0.91]$	0.69	
	$\Omega_\nu h^2 \times 10^{-4}$	$\mathcal{U}[6.0, 64.4]$	8.3	
	Intrinsic alignment			
	$a_1$	$\mathcal{U}[-5.0, 5.0]$	0.7	
	$a_2$	$\mathcal{U}[-5.0, 5.0]$	-1.36	
	$\alpha_1$	$\mathcal{U}[-5.0, 5.0]$	-1.7	
	$\alpha_2$	$\mathcal{U}[-5.0, 5.0]$	-2.5	
	$b_{\text{ta}}$	$\mathcal{U}[0.0, 2.0]$	1.0	
	Lens photo-z			
	$\Delta z_{\text{g}}^1$	$\mathcal{G}[0.006, 0.004]$	0.0	
	$\Delta z_{\text{g}}^2$	$\mathcal{G}[0.001, 0.003]$	0.0	
$\Delta z_{\text{g}}^3$	$\mathcal{G}[0.004, 0.003]$	0.0		
$\Delta z_{\text{g}}^4$	$\mathcal{G}[-0.002, 0.005]$	0.0		
$\Delta z_{\text{g}}^5$	$\mathcal{G}[-0.007, 0.01]$	0.0		
$\sigma z_{\text{g}}^5$	$\mathcal{G}[1.23, 0.054]$	1.0		
Shear calibration				
$m^1$	$\mathcal{G}[-0.0063, 0.0091]$	0.0		
$m^2$	$\mathcal{G}[-0.0198, 0.0078]$	0.0		
$m^3$	$\mathcal{G}[-0.0241, 0.0076]$	0.0		
$m^4$	$\mathcal{G}[-0.0369, 0.0076]$	0.0		
Source photo-z				
$\Delta z_{\text{s}}^1$	$\mathcal{G}[0.0, 0.018]$	0.0		
$\Delta z_{\text{s}}^2$	$\mathcal{G}[0.0, 0.015]$	0.0		
$\Delta z_{\text{s}}^3$	$\mathcal{G}[0.0, 0.011]$	0.0		
$\Delta z_{\text{s}}^4$	$\mathcal{G}[0.0, 0.017]$	0.0		
Point mass				
$B_i \ i \in [1, 5]$	$\mathcal{G}[0.0, 10^4]$	0.0		
Cosmology				
wCDM	$w$	$\mathcal{U}[-2, -0.33]$	-1.0	
Galaxy bias				
Linear bias	$b_1^i \ i \in [1, 3]$	$\mathcal{U}[0.8, 3.0]$	1.7	
	$b_1^i \ i \in [4, 5]$	$\mathcal{U}[0.8, 3.0]$	2.0	
Galaxy bias				
Nonlinear bias	$b_1^i \sigma_8 \ i \in [1, 3]$	$\mathcal{U}[0.67, 2.52]$	1.42	
	$b_1^i \sigma_8 \ i \in [4, 5]$	$\mathcal{U}[0.67, 2.52]$	1.68	
	$b_2^i \sigma_8^2 \ i \in [1, 3]$	$\mathcal{U}[-3.5, 3.5]$	0.16	
	$b_2^i \sigma_8^2 \ i \in [4, 5]$	$\mathcal{U}[-3.5, 3.5]$	0.35	

We analytically marginalize over these terms assuming a unit Gaussian as the prior on the amplitudes  $A_1$  and  $A_2$ . The measured difference is a  $1\sigma$  deviation from the prior center. The final additional covariance term to be added to the fiducial covariance is

$$\Delta \mathcal{C} = \Delta \mathbf{w}_{\text{method}} \Delta \mathbf{w}_{\text{method}}^T + \mathbf{w}_{\text{r.s. bias}} \mathbf{w}_{\text{r.s. bias}}^T. \quad (17)$$

The systematic contribution to each tomographic bin is treated as independent so the covariance between lens bins is not modified. However, we verified that both 0% correlation and 100% correlation between the tomographic bins (hence bounding the likely effect) on a simulated analyses resulted in negligible differences in the cosmological parameter constraints.

## 2. Point-mass analytic marginalization

As mentioned in Sec. II B 3, we modify the inverse covariance to perform analytic marginalization over the PM parameters. As detailed in MacCrann *et al.* [62], using the generalization of the Sherman-Morrison formula, this procedure changes our fiducial inverse covariance  $\mathcal{C}^{-1}$  to  $\mathcal{C}_{\text{wPM}}^{-1}$  as follows:

$$\mathcal{C}_{\text{wPM}}^{-1} = \mathcal{C}^{-1} - \mathcal{C}^{-1} \mathcal{U} (\mathcal{I} + \mathcal{U}^T \mathcal{C}^{-1} \mathcal{U})^{-1} \mathcal{U}^T \mathcal{C}^{-1}. \quad (18)$$

Here  $\mathcal{C}^{-1}$  is the inverse of the halo-model covariance as described above,  $\mathcal{I}$  is the identity matrix and  $\mathcal{U}$  is a  $N_{\text{data}} \times N_{z,\text{g}}$  matrix where the  $i$ th column is given by  $\sigma_{B^i} \vec{t}^i$ . Here  $\sigma_{B^i}$  is the standard deviation of the Gaussian prior on point-mass parameter  $B^i$  and  $\vec{t}^i$  is given as

$$(\vec{t}^i)_a = \begin{cases} 0 & \text{if } a \text{th element does not correspond} \\ & \text{to } \gamma_t(\theta) \text{ and if lens redshift of } a \text{th} \\ & \text{element } \neq i, \\ \beta^{ij} \theta_a^{-2} & \text{otherwise,} \end{cases} \quad (19)$$

where the expression for  $\beta^{ij}$  is shown in Eq. (13). We evaluate that term at fixed fiducial cosmology as given in Table I. In our analysis we put a wide prior on PM parameters  $B^i$  by choosing  $\sigma_{B^i} = 10000$  which translates to the effective mass residual prior of  $10^{17} M_\odot/h$  [see Eq. (A1)].

## E. Blinding and unblinding procedure

We shield our results from observer bias by randomly shifting our results and data vector at various phases of the analysis [91]. This procedure prevents us from knowing the impact of any particular analysis choice on the inferred cosmological constraints from our data until all analysis choices have been made. This procedure, as well as the decision tree used to unblind, is detailed in DES Collaboration [20], which is also employed here. Therefore, all of our cosmology results acquired with fiducial galaxy

samples described in this section are achieved using analysis choices that were validated prior to unblinding (see Sec. IV). The results obtained by changing analysis choices (and with a different galaxy sample), after unblinding, are confined to Secs. V G and V H of the main article and in Appendix C.

#### IV. VALIDATION OF PARAMETER INFERENCE

We assume the likelihood to be a multivariate Gaussian

$$\ln \mathcal{L}(\vec{\mathcal{D}}|\Theta) = -\frac{1}{2}[\vec{\mathcal{D}} - \vec{\mathcal{T}}(\Theta)]^T \mathcal{C}_{\text{wPM}}^{-1}[\vec{\mathcal{D}} - \vec{\mathcal{T}}(\Theta)]. \quad (20)$$

Here  $\vec{\mathcal{D}}$  is the measured  $\gamma_t(\theta)$  and  $w(\theta)$  data vector of length  $N_{\text{data}}$  (if we use all the angular and tomographic bins),  $\vec{\mathcal{T}}$  is the theoretical prediction for these statistics for the parameter values given by  $\Theta$ , and  $\mathcal{C}_{\text{wPM}}^{-1}$  is the inverse covariance matrix of shape  $N_{\text{data}} \times N_{\text{data}}$  (including modifications from the PM marginalization term).

For our analysis we use the Polychord sampler with the settings described in Lemos *et al.* [92]. The samplers probe the posterior  $[\mathcal{P}(\Theta|\vec{\mathcal{D}})]$  which is given by

$$\mathcal{P}(\Theta|\vec{\mathcal{D}}) = \frac{\mathcal{L}(\vec{\mathcal{D}}|\Theta)\mathcal{P}(\Theta)}{\mathcal{P}(\vec{\mathcal{D}})}, \quad (21)$$

where  $\mathcal{P}(\Theta)$  are the priors on the parameters of our model, described in Sec. IV A 4, and  $\mathcal{P}(\vec{\mathcal{D}})$  is the evidence of data.

To estimate the constraints on the cosmological parameters, we have to marginalize the posterior over all the rest of the multidimensional parameter space. We quote the mean and  $1\sigma$  variance of the marginalized posteriors when quoting the constraints. However, note that these marginalized constraints can be biased if the posterior has significant non-Gaussianities, particularly in the case of broad priors assigned to poorly constrained parameters. The maximum *a posteriori* (MAP) point is not affected by such ‘‘projection effects’’; therefore, we also show the MAP value in our plots. However, we note that, in high-dimensional parameter space with a nontrivial structure, it is difficult to converge on a global maximum of the whole posterior (also see Joachimi *et al.* [93] and citations therein).

##### A. Analysis choices

In this subsection, we detail the galaxy-bias models that we use, describe the free parameters of our models, and choose priors on those parameters.

###### 1. PT models

In this analysis, we test two different galaxy-bias models.

- (1) *Linear bias model.*—The simplest model to describe the overdensity of galaxies, valid at large scales, assumes it to be linearly biased with respect to the

dark matter overdensity (see Sec. II A 1). In this model, for each lens tomographic bin  $j$ , the average bias of galaxies is given by a constant free parameter  $b_1^j$ .

- (2) *Nonlinear bias model.*—To describe the clustering of galaxies at smaller scales robustly, we also implement a one-loop PT model. As described in Sec. II A 1, in general, this model has five free bias parameters for each lens tomographic bin. For each tomographic bin  $j$ , we fix two of the nonlinear parameters to their coevolution value given by  $b_s^j = (-4/7)(b_1^j - 1)$  and  $b_{\text{3nl}}^j = b_1^j - 1$  [41,42], while we set  $b_k^j = 0$  [43]. Therefore, in our implementation, we have two free parameters for each tomographic bin: linear bias  $b_1^j$  and nonlinear bias  $b_2^j$ . This allows us to probe smaller scales with minimal extra degrees of freedom, obtaining tighter constraints on the cosmological parameters while keeping the biases due to projection effects, as described below, in control.

As we describe below, in order to test the robustness of our model, we analyze the bias in the marginalized constraints on cosmological parameters. However, given asymmetric non-Gaussian degeneracies between the parameters of the model (particularly between cosmological parameters and poorly constrained nonlinear bias parameters  $b_2^j$  and intrinsic alignment parameters), the marginalized constraints show projection effects. We find that imposing priors on the nonlinear bias model parameters in combination with  $\sigma_8$ , as  $b_1^j\sigma_8$  and  $b_2^j\sigma_8^2$  remove much of the posterior projection effect. As detailed later, these parameters are sampled with flat priors. We emphasize that the flat priors imposed on these nonlinear combinations of parameters are noninformative, and our final constraints on  $b_1^j$  and  $b_2^j$  are significantly tighter than the projection of priors on these parameters.

##### 2. Cosmological models

We report the constraints on two choices of the cosmological model.

- (1) *Flat  $\Lambda$ CDM.*—We free six cosmological parameters the total matter density  $\Omega_m$ , the baryonic density  $\Omega_b$ , the spectral index  $n_s$ , the Hubble parameter  $h$ , the amplitude of scalar perturbations  $A_s$  and  $\Omega_\nu h^2$  (where  $\Omega_\nu$  is the massive neutrino density). We assume a flat cosmological model, and hence the dark energy density  $\Omega_\Lambda$  is fixed to be  $\Omega_\Lambda = 1 - \Omega_m$ .
- (2) *Flat  $w$ CDM.*—In addition to the six parameters listed above, we also free the dark energy equation of state parameter  $w$ . Note that this parameter is constant in time and  $w = -1$  corresponds to the  $\Lambda$ CDM cosmological model.

### 3. Scale cuts

The complex astrophysics of galaxy formation, evolution, and baryonic processes like feedback from active galactic nuclei (AGN), supernova explosions, and cooling make higher-order nonlinear contributions that we do not include in our model. The contribution from these poorly understood effects can exceed our statistical uncertainty on the smallest scales; hence we apply scale cuts chosen so that our PT models give unbiased cosmological constraints.

As mentioned earlier, marginalizing over a multidimensional parameter space can lead to biased 2D parameter constraints due to projection effects. To calibrate this effect for each of our models, we first perform an analysis using a *baseline* data vector constructed from the fiducial values of that model. We then run our Markov chain Monte Carlo (MCMC) chain on the *contaminated* data vector that includes higher-order nonlinearities, and we measure the bias between the peak of the marginalized baseline contours and the peak of the marginalized contaminated contours.

From a joint analysis of 3D galaxy-galaxy and galaxy-matter correlation functions at fixed cosmology in simulations [43], we find that the *linear bias* model is a good description above 8 Mpc/h while the two-parameter *nonlinear bias* model describes the correlations above 4 Mpc/h. We convert these physical comoving distances to angular scale cuts for each tomographic bin and treat them as starting guesses. Then for each model, we iterate over scale cuts until we find the minimum scales at which the bias between marginalized baseline and contaminated contours is less than  $0.3\sigma$ . For the  $\Lambda$ CDM model, we impose this criterion on the  $\Omega_m - S_8$  projected plane, and for the  $w$ CDM model, we impose this criterion on all three 2D plane combinations constructed out of  $\Omega_m$ ,  $S_8$  and  $w$ . Further validation of these cuts is performed using simulations in Sec. IV C and DeRose *et al.* [79].

### 4. Priors and fiducial values

We use locally noninformative priors on the cosmological parameters to ensure statistically independent constraints on them. Although our constraints on cosmological parameters like the Hubble constant  $h$ , spectral index  $n_s$  and baryon fraction  $\Omega_b$  are modest compared to surveys like *Planck*, we have verified that our choice of wide priors does not bias the inference on our cosmological parameters of interest,  $\Omega_m$  and  $S_8$ .

When analyzing the linear bias model, we use a wide uniform prior on these linear bias parameters, given by  $0.5 < b_1^j < 3$ . For the nonlinear bias model, as mentioned above, we sample the parameters  $b_1^j \sigma_8$  and  $b_2^j \sigma_8^2$ . We use uninformative uniform priors on these parameters for each tomographic bin  $j$  given by  $0.67 < b_1^j \sigma_8 < 3.0$  and  $-4.2 < b_2^j \sigma_8^2 < 4.2$ . At each point in the parameter space, we calculate  $\sigma_8$  and retrieve the bias parameters  $b_1^j$  and  $b_2^j$

from the sampled parameters to get the prediction from the theory model. The fiducial values of the linear bias parameters  $b_1^j$  used in our simulated likelihood tests are motivated by the recovered bias values in  $N$ -body simulations and are summarized in Table I. For the nonlinear bias parameters, the fiducial values of  $b_2^j$  are obtained from the interpolated  $b_1 - b_2$  relation extracted from 3D tests in MICE simulations (see Fig. 8 of Pandey *et al.* [43]) for the fiducial  $b_1^j$  for each tomographic bin.

For the intrinsic alignment parameters, we again choose uniform and uninformative priors. As the IA parameters are directly dependent on the source galaxy population, it is challenging to motivate a reasonable choice of prior from other studies. The fiducial values of these parameters required for the simulated test are motivated by the Y1 analysis as detailed in Samuroff *et al.* [94].

We impose an informative prior for our measurement systematics parameters, lens photo- $z$  shift errors ( $\Delta z_g^j$ ), lens photo- $z$  width errors ( $\sigma z_g^j$ ), source photo- $z$  shift errors ( $\Delta z_s^j$ ) and shear calibration biases ( $m^j$ ) for various tomographic bins  $i$ . The photo- $z$  shift parameter changes the redshift distributions for lenses (g) or sources (s) for any tomographic bin  $j$ , used in the theory predictions (see Sec. II) as  $n_{g/s}^j(z) \rightarrow n_{g/s}^j(z - \Delta z_{g/s}^j)$ , while the photo- $z$  width results in  $n_g^j(z) \rightarrow n_g^j(\sigma z_g^j [z - \langle z \rangle^j] + \langle z \rangle^j)$ , where  $\langle z \rangle^j$  is the mean redshift of the tomographic bin  $j$ . Lastly, the shear calibration uncertainty modifies the galaxy-galaxy lensing signal prediction between lens bin  $i$  and source bin  $j$  as  $\gamma_t^{ij} \rightarrow (1 + m^j) \gamma_t^{ij}$ .

For the source photo- $z$ , we refer the reader to Myles *et al.* [82] for the characterization of source redshift distribution, Gatti *et al.* [83] for reducing the uncertainty in these redshift distribution using cross-correlations with spectroscopic galaxies and Cordero *et al.* [95] for a validation of the shift parametrization using a more complete method based on sampling the discrete distribution realizations. For the shear calibration biases, we refer the reader to MacCrann *et al.* [74] which tests the shape measurement pipeline and determine the shear calibration uncertainty while accounting for effects like blending using state-of-art image simulation suite. For the priors on the lens photo- $z$  shift and lens photo- $z$  width errors, we refer the reader to Cawthon *et al.* [80], which cross-correlated the DES lens samples with spectroscopic galaxy samples from Sloan Digital Sky Survey to calibrate the photometric redshifts of lenses (also see Porredon *et al.* [18] and Giannini *et al.* [81] for further details on MagLim redshift calibration).

In this paper we fix the magnification coefficients to the best-fit values described in Elvin-Poole *et al.* [19] and Krause *et al.* [39], but we refer the reader to Elvin-Poole *et al.* [19] for details on the impact of varying the magnification coefficients on the cosmological constraints. Note that in our tests to obtain scale cuts for cosmological analysis using simulated data vectors (described below),

we remain conservative and fix the shear systematics to their fiducial parameter values and analyze the data vectors at the mean source redshift distribution  $n_s(z)$ , as shown in Fig. 2. This procedure, after fixing the systematic parameters, results in tighter constraints and ensures that the impact of baryons and nonlinear bias on the cosmological inference is overestimated. Therefore, we expect our recovered scale cuts to be conservative.

## B. Simulated likelihood tests

We perform simulated likelihood tests to validate our choices of scale cuts, galaxy-bias model and the cosmological model (including priors and external datasets when relevant). In this analysis we focus on determining and validating the scale cuts using redMaGiC lens galaxy sample and we refer the reader to Porredon *et al.* [18] for validation using the MagLim lens galaxy sample. We require that the choices adopted return unbiased cosmological parameters. This first step based on the tests on noiseless data vectors in the validation is followed by tests on cosmological simulations.

### 1. Scale cuts for the linear bias model

Our baseline case assumes linear galaxy bias and no baryonic impact on the matter-matter power spectrum. We use the linear bias values for the five lens bins (in order of increasing redshift)  $b_1 = 1.7, 1.7, 1.7, 2.0$ , and  $2.0$ . We compare the cosmology constraints from the baseline data vector with a simulated data vector contaminated with contributions from nonlinear bias and baryonic physics. For baryons, the nonlinear matter power spectra ( $P_{\text{mm}}^{\text{cont}}$ ) used in

generating the contaminated data vector is estimated using the following prescription:

$$P_{\text{mm}}^{\text{cont}} = \left( \frac{P_{\text{mm}}^{\text{hydro-sim}}}{P_{\text{mm}}^{\text{DM-only}}} \right) P_{\text{mm}}^{\text{Halofit}}, \quad (22)$$

where  $P_{\text{mm}}^{\text{hydro-sim}}$  and  $P_{\text{mm}}^{\text{DM-only}}$  are the matter power spectra measured from a full hydrodynamical simulation and dark matter only simulation, respectively. We use the measurements from the OWLS-AGN simulations, which is based on hydrodynamical simulations that include the effects of supernovae and AGN feedback, metal-dependent radiative cooling, stellar evolution, and kinematic stellar feedback [96]. To capture the effect of nonlinear bias, we use the fiducial  $b_2^j$  values as described in the previous section and fix the bias parameters  $b_s^j$  and  $b_{3\text{nl}}^j$  to their coevolution values.

Figure 3 shows the  $0.3\sigma$  contours when implementing the angular cuts corresponding to  $(8, 6)$  Mpc/h for  $w(\theta)$  and  $\gamma_t$ . The left panel is for  $\Lambda$ CDM, and the right panel for  $w$ CDM (only the  $w - \Omega_m$  plane is shown, but we also verified that the criterion is satisfied in the  $\Omega_m - S_8$  and  $S_8 - w$  planes). The figure shows the peaks of marginalized contaminated and baseline posteriors in 2D planes with blue and red markers, respectively. We find that a  $0.24\sigma$  marginalized contaminated contour intersects the peak of baseline marginalized posterior in  $\Lambda$ CDM model, while the same is true for a  $0.05\sigma$  contour in  $w$ CDM model. We find that, for the linear bias model,  $(8, 6)$  Mpc/h scale cuts pass the above-mentioned criteria that the distance between the peaks of baseline and contaminated contours is less than

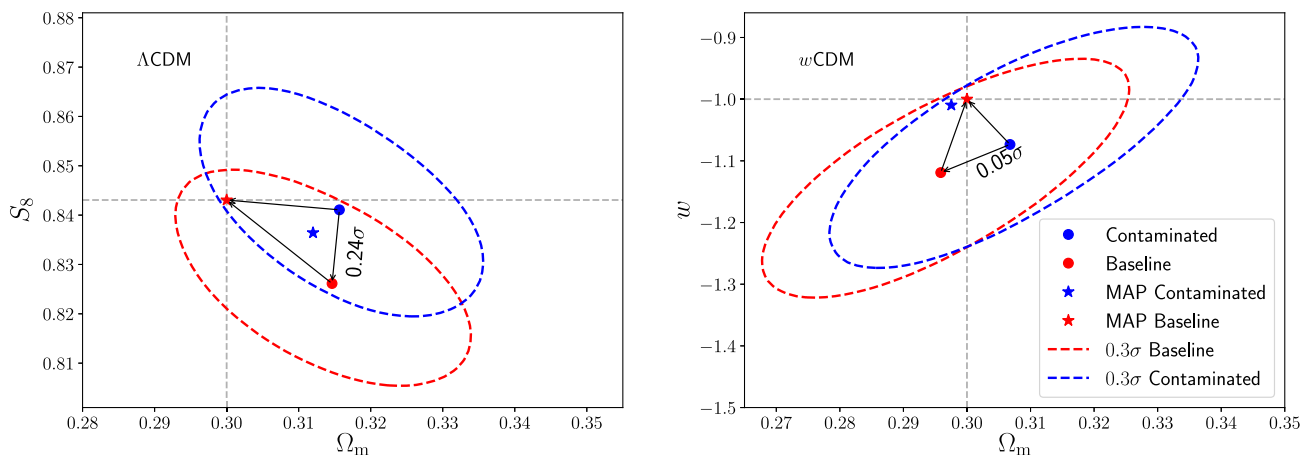


FIG. 3. Simulated data vector parameter constraints from a data vector contaminated with nonlinear bias + baryons but analyzed with a linear bias + Halofit model. Dashed gray lines mark the truth values for the simulated data vector. The left panel shows contours for  $\Lambda$ CDM, and the right panel shows  $w$ CDM. The scale cuts are  $(8, 6)$  Mpc/h for  $w(\theta)$  and  $\gamma_t$ , respectively. In both panels, we compare the peak of the marginalized constraints in the 2D parameter plane for the contaminated data vector (blue circle) and the baseline data vector (red square). The peaks of the marginalized baseline contours are within  $0.3\sigma$  of the peaks of the marginalized contaminated contours, which is our criterion for acceptable scale cuts. We also show the corresponding maximum posterior value obtained for all the contours (with a star symbol), obtained using the methodology described in the main text.

$0.3\sigma$ . In Fig. 3, we also show the MAP parameter values for each run using a star symbol. In order to obtain the MAP value, we use the Nelder-Mead algorithm [97] to minimize the posterior value after starting the optimization from the highest posterior point of the converged parameter inference chain. We find that the MAP point also lies within  $0.3\sigma$  of the true cosmology, further validating the inferred scale cuts (although note the caveats about MAP mentioned in Sec. IV). We note that we analyze smaller scales of  $\gamma_t$  compared to  $w(\theta)$  statistic because it is a less significant measurement and, hence, can tolerate greater modeling uncertainty. Moreover, we use the point-mass marginalization scheme (see Sec. II B 3 and Appendix A) that effectively makes  $\gamma_t$  a local statistic (cf. [15]).

### C. Buzzard simulation tests

Finally, we validate our model with mock catalogs from cosmological simulations for analysis choice combinations that pass the simulated likelihood tests. These tests, and tests of cosmic shear and  $3 \times 2$ -point analyses, are presented in full in DeRose *et al.* [79], and we summarize the details relevant for  $2 \times 2$ -point analyses here. We use the suite of Y3 Buzzard simulations described above. We again require that our analysis choices return unbiased cosmological parameters. In order to reduce the sample variance, we analyze the mean data vector constructed from 18 Buzzard realizations.

#### 1. Validation of linear bias model

We have run simulated  $2 \times 2$ -point analyses on the mean of the measurements from all 18 Buzzard simulations. We compare our model for  $w(\theta)$  and  $\gamma_t(\theta)$  to our measurements at the true Buzzard cosmology, leaving only linear bias and lens magnification coefficients free. In this case, we have

ten free parameters in total, and we find a chi-squared value of 13.6 for 285 data points using our fiducial scale cuts and assuming the covariance of a single simulation, as appropriate for application to the data. Note that the data vector is mean of multiple realization, so we expect a low chi-squared value for the best-fit curve and a principled accounting of error is presented in DeRose *et al.* [79]. This analysis assumes true source redshift distributions, and we fix the source redshift uncertainties to zero as a conservative choice. This results in cosmological constraints where the mean two-dimensional parameter biases are  $0.23\sigma$  in the  $S_8 - \Omega_m$  plane and  $0.18\sigma$  in the  $w - \Omega_m$  plane. These biases are consistent with noise, as they have an approximately  $1/\sqrt{18}\sigma$  error associated with them (assuming  $1\sigma$  error from a single realization). We perform a similar analysis using calibrated photometric redshift distributions where we use redMaGiC lens redshift distributions and use the SOMPZ redshift distribution estimates of source galaxies. These are weighted by the likelihood of those samples given the cross-correlation of our source galaxies with redMaGiC and spectroscopic galaxies (we refer the reader to Appendix F of DeRose *et al.* [79] for detailed procedure). This procedure results in the mean two-dimensional parameter biases of  $0.07\sigma$  in the  $S_8 - \Omega_m$  plane and  $0.05\sigma$  in the  $w - \Omega_m$  plane.

The left panels of Figs. 4 and 5 show the  $0.3\sigma$  constraints obtained from analyzing linear galaxy-bias models in  $\Lambda$ CDM and  $w$ CDM cosmologies on the Buzzard data vector in blue colored contours. Since we expect the marginalized posteriors to be affected by the projection effects, we compare these contours to a simulated noiseless baseline data vector obtained at the input cosmology of Buzzard (denoted by gray dashed lines in Figs. 4 and 5; also see [27]). We find that, similar to results obtained with simulated data vectors in the previous section, our

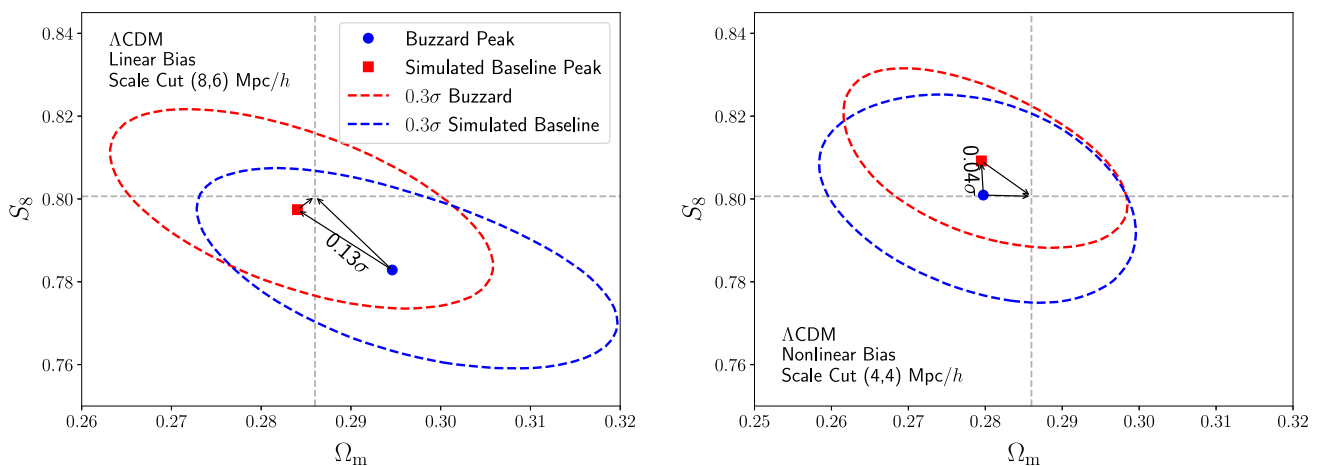
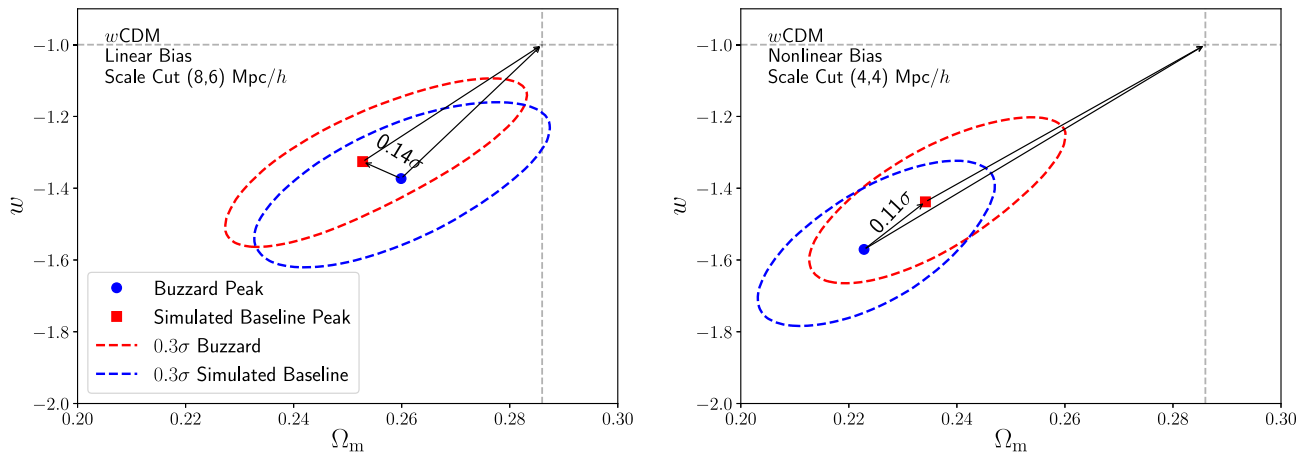


FIG. 4. The blue contours show constraints from Buzzard simulations (blue contours) compared with Buzzard-like theory data vector (red contours) in the  $\Lambda$ CDM cosmological model. The left (right) panel shows the constraints for linear (nonlinear) bias models with the scale cuts given in the legend. The linear and nonlinear bias values are extracted from fits to the 3D correlation functions ( $\xi_{\text{gg}}$  and  $\xi_{\text{gm}}$ ). We see that both the scale-cut choices satisfy our validation criterion.



FIG. 5. The same as Fig. 4 but for  $w$ CDM cosmology.

parameter biases are less than the threshold of  $0.3\sigma$  for the fiducial scale cuts. For a more detailed discussion how these shift compare with probability to exceed (PTE) values of exceeding a  $0.3\sigma$  bias, see Sec. V of DeRose *et al.* [79].

Also note that, as changing the input truth values of the parameters impacts the shape of the multidimensional posterior, we find that the effective magnitude and direction of the projection effects of the baseline contours (comparison of red contours in Fig. 3 with Figs. 4 and 5) are different.

## 2. Scale cuts for nonlinear bias model

Likewise, we have run simulated  $2 \times 2$ -point analyses including our nonlinear bias model on the mean of the measurements from all 18 simulations. Similar to the procedure used to determine the linear bias scale cuts in Sec. IV B 1, we iterate over scale cuts for each tomographic bin defined from varying physical scale cuts.

We compare our model for  $w(\theta)$  and  $\gamma_t(\theta)$  to our measurements at the true Buzzard cosmology, leaving our bias model parameters and magnification coefficients free, which adds 15 free parameters. We find a  $\chi^2$  value of 15.6 for 340 data points using our nonlinear bias scale cuts and assuming the covariance of a single simulation. Simulated analyses using true redshift distributions result in cosmological constraints where the associated mean two-dimensional parameter biases for these analyses are  $0.04\sigma$  in the  $S_8 - \Omega_m$  plane and  $0.11\sigma$  in the  $w - \Omega_m$  plane. This is again consistent with noise due to a finite number of realizations.

In the right panel of Fig. 4 we show the constraints on  $\Omega_m$  and  $S_8$  from the mean Buzzard  $2 \times 2$ pt measurements for  $\Lambda$ CDM cosmological model. The results for nonlinear bias models are shown, where we find the criterion for unbiased cosmology is satisfied for the choice of scale cuts of (4, 4) Mpc/h for  $(w(\theta), \gamma_t(\theta))$ , respectively. Again for a more detailed discussion how these shift compare with PTE values of exceeding a  $0.3\sigma$  bias, see DeRose *et al.* [79]. Figure 5 shows the same analysis for  $w$ CDM cosmological

model in the  $\Omega_m$  and  $w$  plane, where we find similar results. We therefore use (4, 4) Mpc/h as our validated scale cuts when analyzing data with the nonlinear bias model.

## V. RESULTS

In this section we present the  $2 \times 2$ pt cosmology results using the DES Y3 redMaGiC lens galaxy sample and study the implications of our constraints on galaxy bias.

### A. redMaGiC cosmology constraints

In Fig. 6, we compare the constraints on the cosmological parameters obtained from jointly analyzing  $w(\theta)$  and

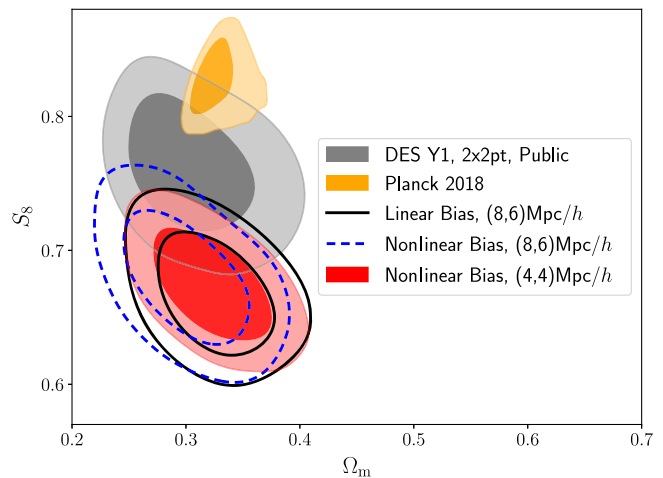


FIG. 6. Comparison of the  $2 \times 2$ pt  $\Lambda$ CDM constraints, using redMaGiC lens galaxy sample, for both linear bias and nonlinear bias models at their respectively defined scale cuts given in the legend. We find a preference for a low value of  $S_8$ , compared to DES Y1  $2 \times 2$ pt public result [15] and Planck 2018 public result [98], with both models of galaxy bias which we investigate in Sec. V C. We also show that analyzing smaller scales using the nonlinear galaxy-bias model leads to 17% better constraints in the  $\Omega_m - S_8$  plane.

$\gamma_t(\theta)$  with both linear and nonlinear bias models. We find  $\Omega_m = 0.325_{-0.034}^{+0.033}$  from the linear bias model (a 10% constraint) at the fiducial scale cuts of (8, 6) Mpc/h [for  $(w(\theta), \gamma_t(\theta))$ , respectively], while using the nonlinear bias model at same scale cuts gives completely consistent constraints. We also show the results for the scale cuts of (4, 4) Mpc/h using the nonlinear bias model where we find  $\Omega_m = 0.323_{-0.035}^{+0.034}$ . These marginalized constraints on  $\Omega_m$  are completely consistent with the public DES Y1  $2 \times 2$ pt results [15] and *Planck* results (including all three correlations between temperature and E-mode polarization; see Aghanim *et al.* [98] for details).

With the analysis of the linear bias model with (8, 6) Mpc/h scale cuts (referred to as fiducial model in the following text), we find  $S_8 = 0.668_{-0.033}^{+0.026}$ . As is evident from the contour plot in Fig. 6, our constraints prefer lower  $S_8$  compared to previous analyses. We use the Monte Carlo parameter difference distribution methodology (as detailed in Lemos *et al.* [99]) to assess the tension between our fiducial constraints and *Planck* results. Using this criterion, we find a tension of  $4.1\sigma$ , largely driven by the differences in the  $S_8$  parameter. We find similar constraints on  $S_8$  from the nonlinear bias as well for both the scale cuts. We investigate the cause of this low  $S_8$  value in the following subsections. We note that the shift to slightly lower  $\Omega_m$  with the nonlinear bias model compared to the linear bias model at (8, 6) Mpc/h scale cuts can arise in a noisy data vector. This is in contrast to the analysis done in Sec. IV with noiseless data vectors to validate the scale cuts.

Note that the nonlinear bias model at (4, 4) Mpc/h scale cuts results in tighter constraints in the  $\Omega_m - S_8$  plane. We estimate the total constraining power in this  $\Omega_m - S_8$  plane by estimating the 2D figure of merit (FOM), which is defined as  $\text{FOM}_{p_1, p_2} = 1/\sqrt{|\det \text{Cov}(p_1, p_2)|}$ , for any two parameters  $p_1$  and  $p_2$  [100,101]. This statistic here is proportional to the inverse of the confidence region area in the 2D parameter plane of  $\Omega_m - S_8$ . We find that the nonlinear bias model at (4, 4) Mpc/h results in a 17% increase in constraining power compared to the linear bias model at (8, 6) Mpc/h.

## B. Comparison with MagLim results

In Fig. 7, we show the comparison of the cosmology constraints obtained from  $2 \times 2$ pt analysis using the MagLim sample (see Porredon *et al.* [18]) with the results obtained here with the redMaGiC lens galaxy sample. The top panel compares the  $\Omega_m - S_8$  contours assuming  $\Lambda$ CDM cosmology while the bottom panel compares the  $\Omega_m - w$  contours assuming  $w$ CDM cosmology. We compare both the linear bias and the nonlinear bias model at the (8, 6) and (4, 4) Mpc/h scale cuts, respectively. We again find that the  $S_8$  constraints obtained with the redMaGiC sample are low compared to the MagLim sample for both linear and nonlinear bias models. As the source galaxy sample, the

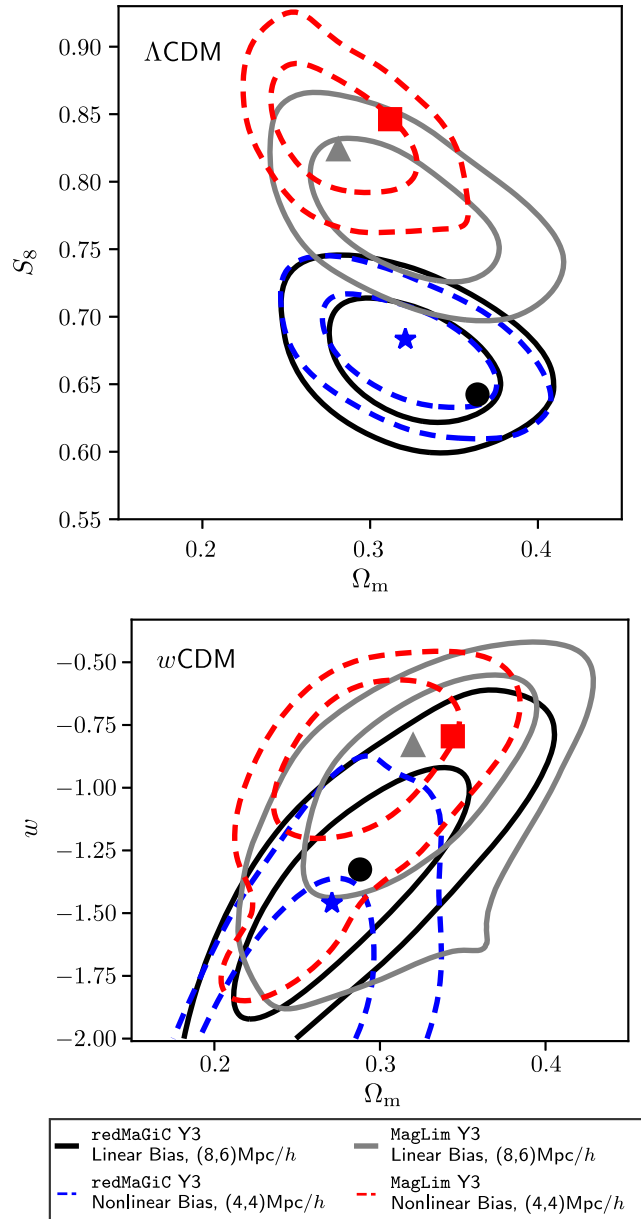


FIG. 7. Comparing the constraints from  $2 \times 2$ pt between the redMaGiC and MagLim samples. The black dot and blue star denote the MAP point estimate for redMaGiC linear and nonlinear bias model, respectively, while the gray triangle and red square show the same for the MagLim sample.

measurement pipeline and the modeling methodology used are the same for the two  $2 \times 2$ pt analysis, this suggests that the preference for low  $S_8$  in our fiducial results is driven by the Y3 redMaGiC lens galaxy sample, which we investigate in the following subsections.

We also show the MAP estimate in the  $\Omega_m - S_8$  and the  $\Omega_m - w$  planes, in order to estimate the projection effects arising from marginalizing over the large multidimensional space to these two-dimensional contours (see Figs. 3 and 5). We find that the nonlinear bias model suffers from mild

projection effects within the  $w$ CDM model (although note the caveats about the MAP estimator mentioned in Sec. IV). We also emphasize that using the nonlinear galaxy-bias model with smaller scale cuts gives similar improvement in the figure of merit of the cosmology contours shown in Fig. 7, using both redMaGiC and MagLim lens galaxy samples.

### C. Internal consistency of the redMaGiC results

To investigate the low  $S_8$  constraints in the fiducial analysis of the redMaGiC galaxy sample, we first check various aspects of the modeling pipeline. In Fig. 8, we show the constraints on  $\Omega_m$ ,  $S_8$  and galaxy bias for the third tomographic bin  $b_3$ , for various robustness tests. We choose to show the third tomographic bin for the galaxy-bias constraints as this bin has the highest signal-to-noise ratio.

We divide the figure into three parts, separated by horizontal black lines. The bottom panel shows the marginalized constraints from the results described in the previous subsection (see Fig. 6). As mentioned previously, we obtain completely consistent constraints from both linear and nonlinear bias models. To check the robustness and keep the interpretation simple, we use the linear bias model using the scale cuts of (8, 6) Mpc/h in the following variations.

In the next part of the figure, moving upward from the bottom, we test the robustness of the model. In particular, we check the robustness of the fiducial intrinsic alignment model by using the NLA model. We also run the analysis by fixing the neutrino masses to  $\Omega_\nu h^2 = 0.00083$ . This choice of  $\Omega_\nu h^2$  parameter corresponds to the sum of neutrino masses,  $\sum m_\nu = 0.06$  eV at the fiducial cosmology described in Table I (which is the baseline value used in

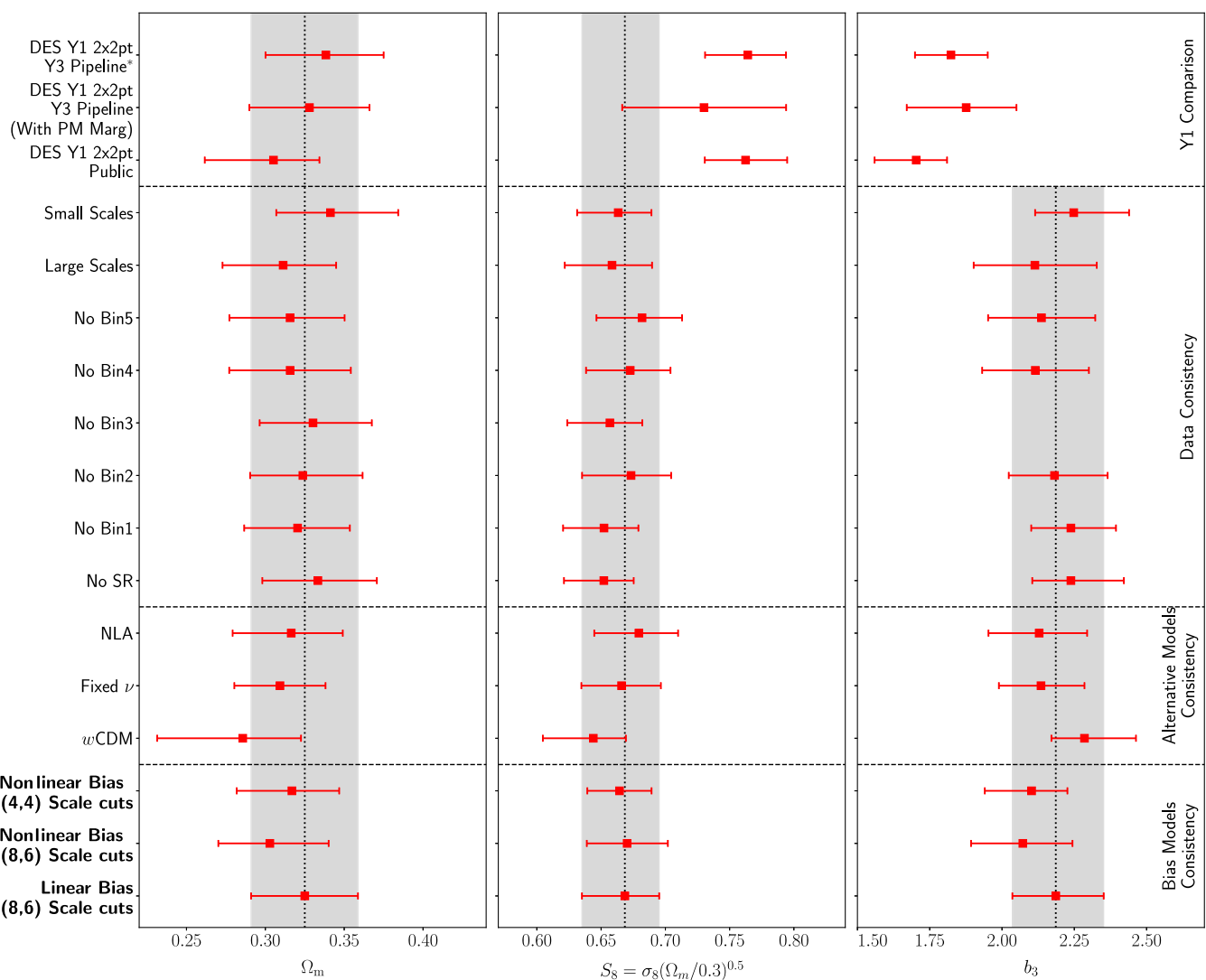


FIG. 8. The consistency of the redMaGiC  $2 \times 2$ pt cosmology and galaxy-bias constraints when changing the analysis choices (see Sec. V C for details). We also compare our constraints to the DES Y1 public  $2 \times 2$ pt results as well as its reanalysis with the current analysis pipeline (we fix the point-mass parameters when reanalyzing the DES Y1 data due to the large degeneracy between point-mass parameters and cosmology at the scale cuts described and validated in Abbott *et al.* [15]).

the *Planck* 2018 cosmology results as well [98]). Lastly, we test the impact of varying the dark energy parameter using the  $w$ CDM model. We find entirely consistent constraints for all of the above variations.

In the next part of the figure, we test the internal consistency of the data vector. Firstly we remove the contribution of shear-ratio information to the total likelihood, resulting in entirely consistent constraints. Also, note that the size of constraints on the cosmological parameters does not change in this case compared to the fiducial results. This demonstrates that the majority of constraints on the cosmological and bias parameters are obtained from the  $w(\theta)$  and  $\gamma_t(\theta)$  themselves. We also test the impact of removing one tomographic bin at a time from the data vector. We find consistent constraints in all five cases. Lastly, we also split the data vector into large and small scales. The small-scale run uses the data vector between angular scales corresponding to (8, 6) and (30, 30) Mpc/h. The large-scale run uses the data vector between angular scales corresponding to (30, 30) Mpc/h and 250 arcmin. When analyzing the large scales, we fix the point-mass parameters to their fiducial values (see Table I) because of the large degradation of constraining power at these larger-scale cuts due to the degeneracy between point-mass parameters, galaxy bias and cosmological parameter  $\sigma_8$  (see Appendix A and MacCrann *et al.* [62]). In both of these cases, we find similar constraints on all parameters, demonstrating that the low  $S_8$  does not originate from either large or small scales.

As an additional test of the robustness of the modeling pipeline, we analyze the  $w(\theta)$  and  $\gamma_t(\theta)$  measurements as measured from DES Y1 data [15]. Note that, in this analysis, we keep the same scale cuts as described and validated in Abbott *et al.* [15], which are 8 Mpc/h for  $w(\theta)$  and 12 Mpc/h for  $\gamma_t(\theta)$ . To analyze this data vector, while we use the model described in this paper, we fix the point-mass parameters again to zero due to similar reasons as described above in the analysis of large scales. The constraints we obtain are consistent with the public results described in Abbott *et al.* [15]. We attribute an approximately  $1\sigma$  shift in the marginalized  $\Omega_m$  posterior to the improvements made in the current model, compared to the model used for the public Y1 results [55]. In particular, we use the full non-Limber calculation, including the effects of redshift-space distortions, for galaxy clustering (also see Fang *et al.* [50]).

Lastly, to assess the impact of projection effects on the  $S_8$  parameter, we compare the profile posterior to the marginalized posterior. The profile posterior in Fig. 9 is obtained by dividing the samples into 20 bins of  $S_8$  values and calculating the maximum posterior value for each bin. Therefore, unlike the marginalized posterior, the profile posterior does not involve the projection of a high-dimensional posterior to a single  $S_8$  parameter. Hence the histogram of the profile posterior is not impacted by projection effects. We compare the marginalized posterior and profile posterior in Fig. 9, showing that projection effects have a subdominant impact on the marginalized  $S_8$  constraints. This demonstrates that

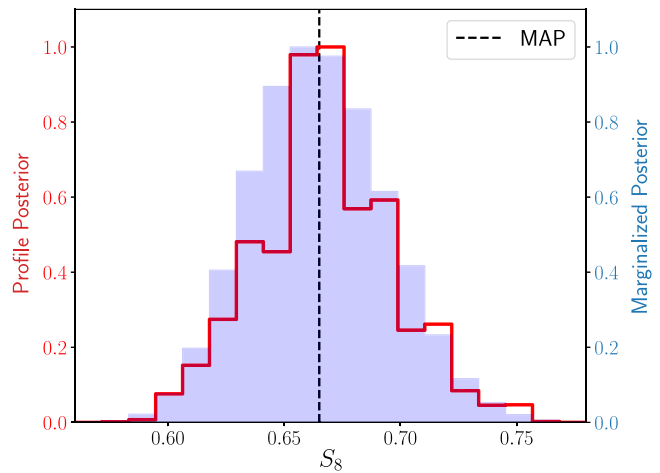


FIG. 9. Comparison of the profile posterior and marginalized posterior on the  $S_8$  parameter from the  $2 \times 2$ pt redMaGiC  $\Lambda$ CDM chain.

projection effects do not explain the preference for low  $S_8$  with the redMaGiC sample.

In summary, the results presented in this subsection demonstrate that our modeling methodology is entirely robust, and hence we believe our data are driving the low  $S_8$  constraints with the redMaGiC sample. Moreover, as described above, no individual part of the data drives a low value of  $S_8$ ; therefore, we perform global checks of the data vector in the following subsections.

#### D. Galaxy bias from individual probes

In this subsection, we test the compatibility of the  $w(\theta)$  and  $\gamma_t(\theta)$  parts of the data vector. As we will lose the power of complementarity when analyzing them individually, we fix the cosmological parameters to the maximum posterior obtained from the DES Y1  $3 \times 2$ pt analysis [15]. We find that the best-fit bias values from the  $w(\theta)$  part of the data vector are systematically higher than  $\gamma_t(\theta)$  for each tomographic bin. We parametrize this difference in bias values with a phenomenological parameter  $X$  for each tomographic bin  $i$  as

$$X_{\text{lens}}^i = b_{\gamma_t(\theta)}^i / b_{w(\theta)}^i. \quad (23)$$

We refer to  $X$  as a “decorrelation parameter” because its effect on the data is very similar to assuming that the mass and galaxy density functions have less than 100% correlation. A value of  $X = 1$  is expected from local biasing models. The constraints on the parameter  $X_{\text{lens}}^i$  are shown in Fig. 10. We also compare the constraints of these  $X_{\text{lens}}^i$  parameters obtained from Y1 redMaGiC  $2 \times 2$ pt (see Abbott *et al.* [15] and Prat *et al.* [102] for details) and the  $2 \times 2$ pt data vector using Y3 MagLim lens galaxy sample. For the Y1 redMaGiC data vector, we fix the scale cuts and priors on the calibration of photometric redshifts of lens and source galaxies as described in Abbott *et al.* [15] and for analysis of Y3

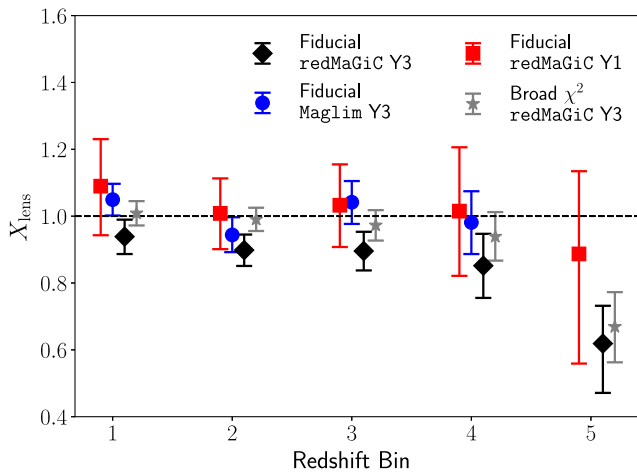


FIG. 10. Constraints on the phenomenological decorrelation parameter,  $X_{\text{lens}}^i$ , for each tomographic bin obtained from  $2 \times 2$ pt analysis using Y1 redMaGiC, Y3 fiducial redMaGiC sample, Y3 broad- $\chi^2$  redMaGiC sample (see Sec. V G) and Y3 MagLim as the lens galaxies (the cosmological parameters are fixed to the DES Y1 best-fit values [15]).

MagLim data vector we follow the analysis choices detailed in Porredon *et al.* [18]. In this analysis of all the data vectors, we use the linear bias galaxy-bias model while keeping the rest of the model the same as described in Sec. II B. We find that the Y1 redMaGiC as well as Y3 MagLim  $2 \times 2$ pt data are consistent with  $X_{\text{lens}}^i = 1$  for all the tomographic bins, while redMaGiC Y3  $2 \times 2$ pt data have a persistent preference for  $X_{\text{lens}}^i < 1$  for all the tomographic bins.

Noticeably, we find that for the DES Y1 best-fit cosmological parameters, the Y3 redMaGiC data vector prefers a value of  $X_{\text{lens}}^i \sim 0.9$  for each tomographic bin. Therefore, in order to keep the interpretation simple, we use a single parameter  $X_{\text{lens}}$  to describe the ratio of galaxy bias  $b_{\gamma_i(\theta)}^i / b_{w(\theta)}^i$  for all tomographic bins  $i \in [1, 5]$ . We constrain this single redshift-independent parameter to be  $X_{\text{lens}} = 0.9^{+0.03}_{-0.03}$  for Y3 redMaGiC, a  $3.5\sigma$  deviation from  $X_{\text{lens}} = 1$ . Within general relativity, even when including the impact of nonlinear astrophysics, we do not expect a decorrelation between galaxy clustering and galaxy-galaxy lensing to be present at more than a few percent level [103]. We comment on the impact of this decorrelation on the redMaGiC cosmology constraints in Sec. V F.

Note that the inferred value of  $X_{\text{lens}}$  depends on the cosmological parameters, because the large-scale amplitudes of galaxy clustering and galaxy-galaxy lensing involve different combinations of galaxy bias,  $\sigma_8$  and  $\Omega_m$ . Therefore, a self-consistent inference of  $X_{\text{lens}}$  requires the full  $3 \times 2$ pt data vector and is presented in DES Collaboration [20]. However, the DES Y1  $3 \times 2$ pt best-fit cosmological parameters are fairly close to the DES Y3  $3 \times 2$ pt best-fit parameters; therefore, we expect the results presented here to be good approximations to those obtained with the Y3  $3 \times 2$ pt data vector.

### E. Area split of the decorrelation parameter

In order to further study the properties of this decorrelation parameter  $X_{\text{lens}}$ , we estimate it independently in ten approximately equal area patches of the DES Y3 footprint. We measure the data vectors,  $w(\theta)$  and  $\gamma_t(\theta)$  in each of these ten patches, using the same methodology presented in Sec. III C 4. In order to obtain the covariance for each patch, we rescale the fiducial covariance (see Sec. III D) of the full footprint to the area of each patch. We then estimate  $X_{\text{lens}}$  from each patch while keeping all the other analysis choices the same.

In Fig. 11 we show the DES footprint split into ten regions. In this figure, each region is colored in proportion to the mean value of the  $X_{\text{lens}}$  parameter we obtain using redMaGiC as the lens galaxy sample. We run a similar analysis when using MagLim as the lens sample.

In Fig. 12 we show a scatter plot between the value of  $X_{\text{lens}}$  recovered from each of ten regions using redMaGiC and MagLim as lens samples. We find a tight correlation between the value of  $X_{\text{lens}}$  from the two lens samples, as would be expected if they share noise from sample variance and fluctuations in the source galaxy population. Note that the scatter in the inferred  $X_{\text{lens}}$  for both the MagLim and the redMaGiC samples corresponding to each sky patch (red points) around the mean of full sample (the blue point) is consistent with the expectation. This shows that, compared with MagLim, the redMaGiC lens sample has a preference for  $X_{\text{lens}} < 1$  in the whole DES footprint. This correlation and area independence of the ratio  $X_{\text{Redmagic}}/X_{\text{Maglim}}$  is remarkable and suggests that the potential systematic in the redMaGiC sample has a more global origin.

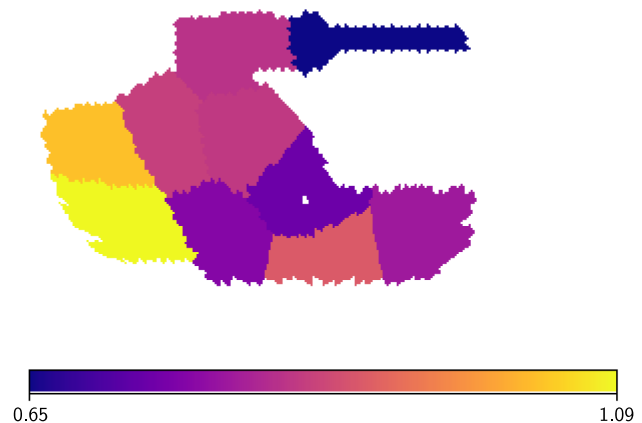


FIG. 11. The DES footprint is split into ten regions. The color of each area corresponds to the mean value of the constraints on  $X_{\text{lens}}$  from that particular area, inferred at fixed DES Y1 cosmology and using the redMaGiC lens sample. This plot shows that no special region in the sky (for example, near the galactic plane) drives the preference for low  $X_{\text{lens}}$ . While a variation over the sky in the inferred  $X_{\text{lens}}$  is expected from analyzing only the  $2 \times 2$ pt data due to the variations in the photometric redshift distribution of source galaxies, we find that the preferred mean value of  $X_{\text{lens}}$  from the redMaGiC sample is significantly lower than the expected value of 1 (see Fig. 12).

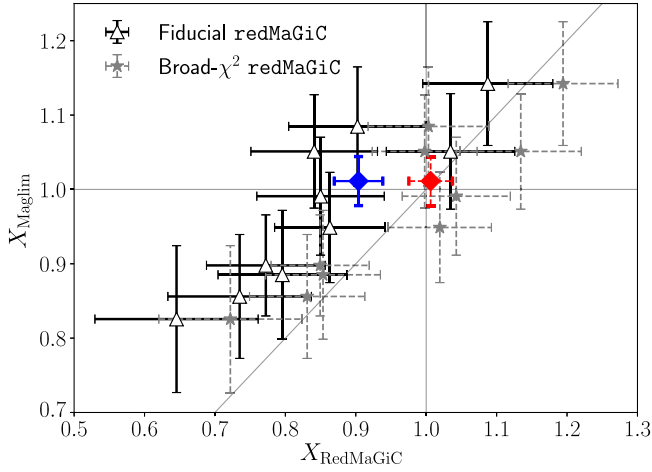


FIG. 12. Each error bar corresponds to the 68% credible interval constraints on  $X_{\text{lens}}$  from one of the ten regions (see Fig. 11), using either the redMaGiC sample or the MagLim lens galaxy sample. The blue error bar corresponds to the constraints on  $X_{\text{lens}}$  from the entire Y3 area using the MagLim sample and the fiducial redMaGiC sample, whereas the red error bar uses the broad- $\chi^2$  galaxy sample (see Sec. V G). We find a tight correlation between  $X_{\text{Redmagic}}$  and  $X_{\text{Maglim}}$ , due to common sources of statistical noise (e.g., photometric redshifts of the source galaxies). For example, if the photometric redshift distribution of the source galaxies fluctuates from the imposed prior for each patch in a different direction, it would shift the inferred  $X_{\text{lens}}$  similarly for each lens sample. We find that, while the inferred  $X_{\text{lens}}$  from ten regions using the MagLim and the broad- $\chi^2$  redMaGiC sample fluctuates around its mean value that is close to 1, the inference from the fiducial redMaGiC sample fluctuates around a mean value that is significantly lower than 1. This figure shows that the fiducial redMaGiC sample prefers  $X_{\text{lens}}$  to be lower than 1, independent of the sky area.

### F. Impact of decorrelation on $2 \times 2\text{pt}$ cosmology

To summarize, assuming a standard cosmological model, we have identified that the galaxy-clustering and galaxy-galaxy lensing signal measured using the Y3 redMaGiC lens galaxy sample are incompatible with each other (at the set of cosmological parameters preferred by previous studies). We have further identified that this incompatibility is well captured by a redshift-, scale- and area-independent phenomenological parameter  $X_{\text{lens}}$ . Using Y3 redMaGiC lens sample, we detect  $X_{\text{lens}} \sim 0.9$ , at the  $3.5\sigma$  confidence level away from the expected value of  $X_{\text{lens}} = 1$ . This  $2 \times 2\text{pt}$  analysis is done when the cosmological parameters are fixed to their DES Y1 best-fit values; a self-consistent  $X_{\text{lens}}$  inference analysis with free cosmological parameters requires the full  $3 \times 2\text{pt}$  data vector. This is presented in DES Collaboration [20], where the inferred constraints on this decorrelation parameter are  $X_{\text{lens}} = 0.87^{+0.02}_{-0.02}$ .

In Fig. 13, we fix  $X_{\text{lens}} = 0.87$  in our model and rerun the Y3 redMaGiC  $2 \times 2\text{pt}$  analysis. We find, as expected, that this has a significant impact on the marginalized  $S_8$  values and results in the marginalized constraints  $S_8 = 0.76^{+0.034}_{-0.037}$ ,

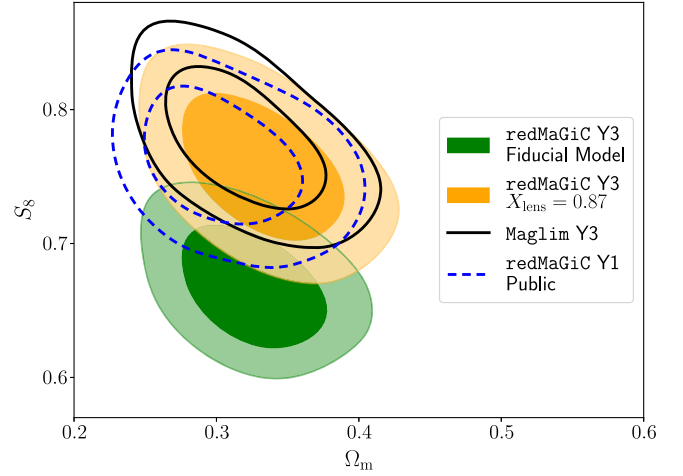


FIG. 13. Comparison of the constraints from  $2 \times 2\text{pt}$  analysis when using the mean value of  $X_{\text{lens}}$  parameter for redMaGiC lens sample analysis, as estimated and described in DES Collaboration [20]. We find a shift in  $S_8$  parameter compared to our fiducial results in Sec. V A, but  $\Omega_m$  constraints are fully consistent.

completely consistent with  $2 \times 2\text{pt}$  Y1 redMaGiC public results as well as Y3 MagLim results. Also note that the marginalized constraints on  $\Omega_m$  for  $X_{\text{lens}} = 0.87$  model are  $\Omega_m = 0.331^{+0.037}_{-0.037}$ , which remains consistent with the fiducial result.

### G. Broad- $\chi^2$ redMaGiC sample

In order to further investigate the source of the decorrelation, we modify the  $\chi^2_{\text{RM}}$  threshold for a galaxy to be classified as a redMaGiC galaxy when fitting to the redMaGiC template using the procedure as described in Rozo *et al.* [23]. As described in Sec. III A 1, the fiducial redMaGiC catalog is generated by implementing the  $\chi^2_{\text{RM}}$  threshold of 3. This low- $\chi^2_{\text{RM}}$  threshold only selects the galaxies that closely match the template. In case there are any residual variations in the redMaGiC catalog number densities caused by variations in the colors that are not already corrected using the fiducial weighting scheme (as described in Rodríguez-Monroy *et al.* [21]), it would contribute a spurious galaxy clustering signal. This would contribute toward  $X_{\text{lens}} < 1$ , as we found above. In order to test this hypothesis, we increase the threshold criteria and generate another catalog with  $\chi^2_{\text{RM}} = 8$  and denote this new sample as the “broad- $\chi^2$ ” sample.

We show the result for  $X_{\text{lens}}^i$  for all five tomographic bins in Fig. 10. We find that with the broad- $\chi^2$  sample  $X_{\text{lens}}^i$  is consistent with 1 for the first four tomographic bins, while we still find that for the fifth tomographic bin,  $X_{\text{lens}}^5 < 1$ , this bin has low constraining power. We also show the inferred  $X_{\text{lens}}$  from ten independent regions over the DES footprint in Fig. 11. We find that, with the new sample, the scatter in the inferred  $X_{\text{lens}}$  is consistent with the expected value of 1. Moreover, as shown with a red symbol in

TABLE II. The lens photo- $z$  shift and stretch parameters varied in the analysis using the broad- $\chi^2$  sample and their prior range used ( $\mathcal{G}[\mu, \sigma] \equiv$  Gaussian prior with mean  $\mu$  and standard deviation  $\sigma$ ).

Parameter	Prior
$\Delta z_{\text{g}}^1$	$\mathcal{G}[0.0088, 0.0029]$
$\sigma z_{\text{g}}^1$	$\mathcal{G}[1.015, 0.035]$
$\Delta z_{\text{g}}^2$	$\mathcal{G}[-0.0033, 0.0022]$
$\sigma z_{\text{g}}^2$	$\mathcal{G}[0.991, 0.028]$
$\Delta z_{\text{g}}^3$	$\mathcal{G}[0.0076, 0.0029]$
$\sigma z_{\text{g}}^3$	$\mathcal{G}[1.096, 0.029]$
$\Delta z_{\text{g}}^4$	$\mathcal{G}[0.0015, 0.0042]$
$\sigma z_{\text{g}}^4$	$\mathcal{G}[1.104, 0.045]$
$\Delta z_{\text{g}}^5$	$\mathcal{G}[-0.0058, 0.0061]$
$\sigma z_{\text{g}}^5$	$\mathcal{G}[1.193, 0.056]$

Fig. 11, we find the redshift- and area-independent  $X_{\text{lens}}$  to be entirely consistent with 1 using the broad- $\chi^2$  sample. This validates our hypothesis and points toward an uncorrected systematic that might be related to a color-dependent photometric issue in the DES data. Since the shear catalog, as well as the MagLim galaxy catalog, do not select galaxies based on a red-galaxy template, we do not expect this systematic to have an effect on those catalogs.

In Appendix C, we further describe details of this new sample and compare it with our fiducial redMaGiC sample. With this new sample, we use conservative analysis choices and implement the following approximations.

- (i) We downsample the broad- $\chi^2$  catalog to roughly match the number densities of the fiducial redMaGiC sample. This ensures that the validations of analysis choices performed for the redMaGiC sample, including the covariance, scale cuts, and methodology, remain true for the broad- $\chi^2$  sample as well.
- (ii) We use a two-parameter model (shift and stretch parametrization) to account for the uncertainty in the lens redshift distribution for each tomographic bin [80]. We implement this model to reduce the impact of the outliers in the assigned galaxy redshifts for this new sample. The Gaussian priors on the shift and stretch parameters are tabulated in Table II.

We show the cosmological constraints from the broad- $\chi^2$  sample in Fig. 14 and find that they are consistent with the results from MagLim sample in both  $\Lambda$ CDM and  $w$ CDM cosmological models. Using the  $\Lambda$ CDM model, we constrain  $\Omega_m = 0.363_{-0.0388}^{+0.0375}$  and  $S_8 = 0.73_{-0.029}^{+0.035}$ , and using the  $w$ CDM model, we constrain  $w = -0.821_{-0.4341}^{+0.1908}$ .

We note that this analysis is showing the constraints on the cosmological parameters under the approximation that we neglect the contribution to the LSS covariance systematic term. We use the ISD method to get the weights for this sample. Moreover, we assume that the same scale cuts work with this sample as we obtained for the fiducial redMaGiC

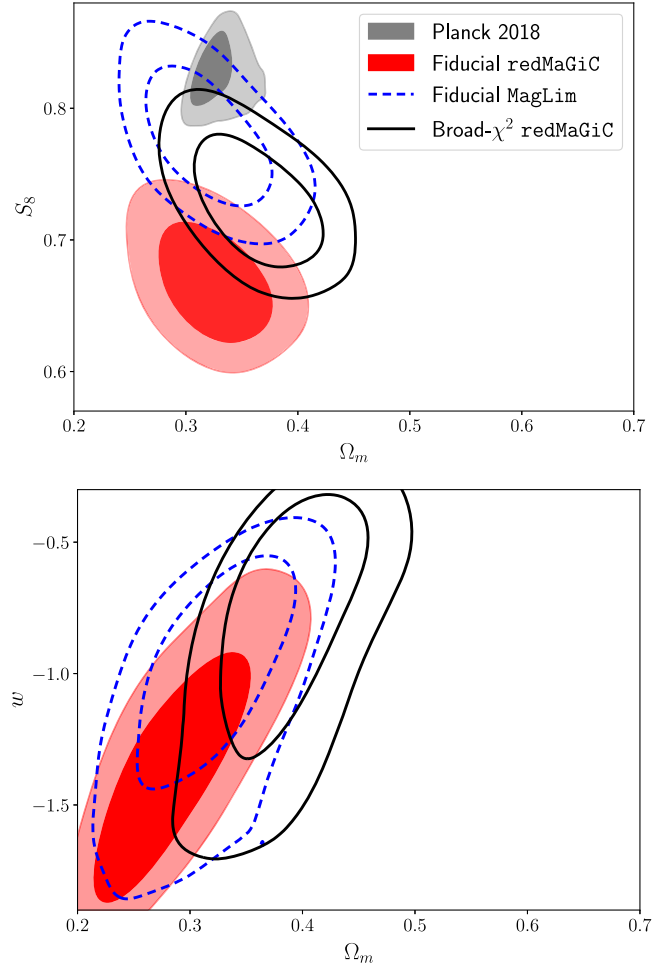


FIG. 14. Constraints on the cosmological parameters using the linear bias model with the broad- $\chi^2$  redMaGiC sample. The top figure corresponds to the  $\Lambda$ CDM cosmological model and the bottom figure corresponds to the  $w$ CDM cosmological model. We also compare the constraints from the fiducial redMaGiC and the fiducial MagLim lens galaxy samples.

sample. Lastly, we have used the same value of lens magnification as for the fiducial redMaGiC sample. We do not expect these choices to have any major effects on the cosmological constraints described above. However, we leave a detailed study optimizing the  $\chi^2_{\text{RM}}$  value, validating the analysis choices, and obtaining final constraints with redMaGiC sample to DES Collaboration [104].

## H. redMaGiC host-halo mass inference

In the halo model framework (see Cooray and Sheth [105] for a review), the value of the linear bias of a tracer of dark matter can be related to the host-halo mass of that tracer. The standard HOD approach parametrizes the distribution of galaxies inside halos, and hence the observed number density as well as the large-scale bias values of any galaxy sample can be expressed in terms of its HOD parameters [106–108]. The same HOD parameters can also be used to infer the mean

host-halo mass of the galaxy sample. We use the constraints on linear galaxy-bias parameters and the comoving number density to infer the mean host-halo mass of the broad- $\chi^2$  redMaGiC galaxy sample by marginalizing over HOD parameters.

The details of the halo model framework used here are given in Appendix D. Note that we have neglected the effects of assembly bias and the correlation between number density and bias constraints in this analysis. With these caveats in mind, in Fig. 15 we show approximately 25% constraints on mean host-halo mass of broad- $\chi^2$  redMaGiC galaxies and the constraints for different tomographic bins show its evolution with redshift. This redshift evolution trend is broadly consistent with the pseudoevolution of halo masses due to changing background reference density with redshift (see [109] for more details). Therefore we find that the broad- $\chi^2$  redMaGiC sample lives in halos of mass of approximately  $1.6 \times 10^{13} M_\odot/h$ , which remains broadly constant with redshift.

We also bracket the uncertainty in the host-halo masses of the fiducial redMaGiC sample with a gray band in Fig. 15. In order to estimate the band, we use the linear bias constraints from the  $2 \times 2$ pt analysis with fiducial redMaGiC sample, after fixing  $X_{\text{lens}} = 0.87$ . This decorrelation parameter results in  $w(\theta)$  and  $\gamma_t$  preferring different linear bias parameters, related by  $b^i[w(\theta)]/b^i[\gamma_t(\theta)] = X_{\text{lens}} = 0.87$ , for all tomographic bins  $i$ . Therefore, we infer the host-halo masses using both linear bias parameter values. The band is estimated by using the lower limit of masses inferred by  $b^i[\gamma_t(\theta)]$  and upper limit of masses inferred by  $b^i[w(\theta)]$  for all

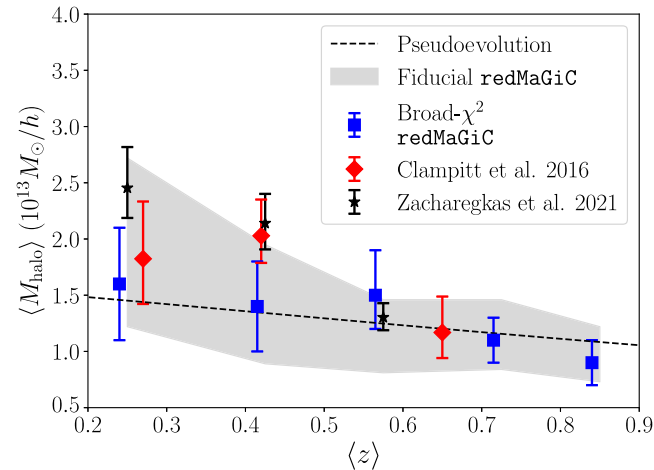


FIG. 15. This figure shows the inferred constraints on mean host-halo masses of redMaGiC galaxies for five tomographic bins. We use the HOD framework to make this inference as detailed in Appendix D and use the linear bias constraints obtained using the broad- $\chi^2$  redMaGiC sample. We infer the mean host-halo masses from the linear bias constraints for all five tomographic bins. We compare our results to Clampitt *et al.* [110] and Zacharegkas *et al.* [111] and also show the expected pseudoevolution of a halo having  $M_{\text{halo}} = 1.6 \times 10^{13} M_\odot/h$  at  $z = 0$ .

tomographic bins  $i$ . We find that the broad- $\chi^2$  sample has a slight preference for lower halo masses, but it is consistent with constraints for the fiducial sample.

We find that our results are also broadly consistent with the analysis of [110], which used the redMaGiC galaxies of DES science-verification dataset and estimated the mean halo masses by studying galaxy-galaxy lensing signal in a broad range of scales (including high signal-to-noise small scales that we remove here) using HOD model.<sup>3</sup> We also find broad agreement with a similar study presented in Zacharegkas *et al.* [111], analyzing DES Y3 using the galaxy-galaxy lensing data estimated from the fiducial redMaGiC sample and on a wide range of scales with an improved halo model.

## VI. CONCLUSIONS

This paper has presented the cosmological analysis of the  $2 \times 2$ pt data vector of the DES year-3 dataset using redMaGiC lens sample. We refer the reader to Porredon *et al.* [18] for similar results using MagLim lens sample and Elvin-Poole *et al.* [19] for details on the impact of lens magnification on the  $2 \times 2$ pt data vector. The  $2 \times 2$ pt data vector comprises the two-point correlations of galaxy clustering and galaxy lensing using five redshift bins for the lens galaxies and four bins for source galaxies. It provides independent constraints on two primary parameters of interest, the mass density  $\Omega_m$  and amplitude of fluctuations  $S_8$ . As shown in Fig. 1, these constraints are complementary to those from cosmic shear. The combination of  $2 \times 2$ pt with cosmic shear is thus better able to constrain  $\Omega_m$  and  $S_8$  as well as the dark energy equation of state parameter  $w$ . Perhaps more importantly, this provides a robustness check on the results from either approach.

The estimation and marginalization of galaxy-bias parameters is one of the central tasks in extracting cosmology from the  $2 \times 2$ pt data vector. We have developed and validated the methodology for this based on perturbation theory. We use a five-parameter description of galaxy bias per redshift bin, with three of the parameters fixed based on theoretical considerations. We validated these choices using mock catalogs built on  $N$ -body simulations as detailed in our earlier study [43] and Sec. IV C. We carry out two analyses: the first using linear bias with more conservative scale cuts and the second using the full PT bias model going down to smaller scales. Other elements of our model include intrinsic alignments, magnification and “point-mass marginalization” (see Sec. II B). The validation of the analysis choice and scale cuts with simulated data vectors (both idealized and from mock catalogs) are presented in Sec. IV A.

<sup>3</sup>Note that we use  $M_{200c}$  as our halo mass definition, which denotes the total mass within a sphere enclosing a mean density which is 200 times the *critical* density of the Universe. Clampitt *et al.* [110] work with  $M_{200m}$  as their mass definition, denoting the total mass within a sphere enclosing a mean density which is 200 times the *mean* density of the Universe; therefore, we convert their constraints to  $M_{200c}$  in the above figure.



Our cosmological results are presented in Figs. 6–8, which show preference for a low value of  $S_8$  parameter when compared with previous results. We refer the reader to DES Collaboration [20], where, after unblinding the cosmological parameter constraints, we find similar inconsistency in the  $S_8$  parameter constraints between Y3  $2 \times 2$ pt redMaGiC analysis and Y3 cosmic-shear analysis, as well as a high  $\chi^2$  using the  $\Lambda$ CDM model. As detailed in DES Collaboration [20], we discovered that the reason for the high  $\chi^2$  of the  $3 \times 2$ pt analysis with the fiducial model was due to inconsistencies in the galaxy-galaxy lensing and galaxy clustering signals. The source of this inconsistency is still undetermined; however, we found that a single parameter  $X_{\text{lens}}$ , representing the ratio of the bias inferred from  $w(\theta)$  and  $\gamma_t$ , substantially improves the goodness of fit. This ratio is cosmology dependent and can only be inferred consistently (along with the other model parameters) when using the full  $3 \times 2$ pt analysis, presented in DES Collaboration [20].

This ratio is expected to be unity in the absence of galaxy stochasticity, an effect that is expected to be only at the percent level on scales above  $\sim 10$  Mpc [103]. Several previous analyses with similar datasets have also found this ratio to be consistent with unity [3,7,102]. However, we detect a value of  $X_{\text{lens}} = 0.87$ , below 1 at the  $5\sigma$  level. This purely phenomenological model assumes no scale or redshift dependence, and we found consistent values of  $X_{\text{lens}}$  when fitting to different scales (see Fig. 8) and when fitting separate values for each *lens* redshift bin (see Fig. 10). Considering the constraints from the cosmic-shear measurements, no known cosmological effect can produce such a large and coherent deviation in clustering and galaxy lensing. We therefore pursued possible systematic errors that could lead to this unusual result. Note that this kind of behavior can arise with potential systematics, for example unaccounted-for impact of photometric uncertainty or background subtraction for large or faint objects on the galaxy selection. This can introduce extra fluctuation of the number density of the lens galaxies across the footprint which will not be captured by the set of survey property maps used in the LSS weights estimation pipeline.

Figure 13 shows the  $2 \times 2$ pt redMaGiC cosmology constraints after fixing  $X_{\text{lens}} = 0.87$ , the best-fit value from DES Collaboration [20]. There is a significant shift in  $S_8$ , while  $\Omega_m$  remains stable. Interestingly the resulting contours are fully consistent with the Y1 analysis as well as the  $2 \times 2$ pt analysis using the MagLim lens galaxy sample [18]. We track down the source of this decorrelation to an aggressive threshold on the colors of galaxies to match the red-galaxy template. We find that using a sample with a relaxed threshold, which we call the broad- $\chi^2$  sample, results in cosmological constraints that are consistent with the expectations from MagLim sample. This points toward the existence of a potential color-dependent systematic in the galaxy catalog, and we leave a detailed exploration and mitigation of this systematic to a future study [104].

We note that, although recent analyses using BOSS galaxies have found similar inconsistencies in the galaxy

clustering and galaxy-galaxy lensing using *Planck*-preferred cosmological parameters (see [112,113] and references therein); there are some important differences. In this analysis as well as in DES Collaboration [20], unlike in Leauthaud *et al.* [112], we do not use any small-scale information for galaxy clustering and galaxy-galaxy lensing measurements. Therefore, we are significantly less prone to the impacts of poorly understood small-scale nonlinear physics, like baryon feedback and galaxy assembly biases [114–116]. Moreover, in DES Collaboration [20], by leveraging all three two-point functions used in  $3 \times 2$ pt, the analysis of the consistency between galaxy lensing and galaxy clustering can be carried out while freeing the relevant cosmological parameters. The analysis in this paper fixes the cosmological parameters close to the best-fit cosmology from DES Collaboration [20]; hence, our results are a good approximation to the analysis using the full  $3 \times 2$ pt data vector. Similarly, a few recent studies jointly analyzing galaxy clustering autocorrelations and galaxy-CMB lensing cross-correlations have also reported preference for lower galaxy-bias value for the cross-correlation compared to the autocorrelations [117,118]. However, similar to the above analysis with BOSS galaxies, these studies also fix their cosmological parameters to the best-fit cosmology from *Planck* results [98], which is different from this study (see [119] for related discussion).

To access the information in the measurements on smaller scales, we use higher-order perturbation theory. We use a hybrid one-loop perturbation theory model for galaxy bias, capturing the nonlinear contributions to the overdensity field till third order. We have tested and validated our model using three-dimensional correlation functions from DES mock catalogs in Pandey *et al.* [43] as well as with projected statistics in DeRose *et al.* [79]; in this study, we validate the bias model with mocks for the  $2 \times 2$ pt redMaGiC data vector at scales above  $4 \text{ Mpc}/h$ . This validation presented here, along with results in Pandey *et al.* [43], are then also directly used to validate the nonlinear bias model for MagLim data vector. We apply it to the data and find that the nonlinear bias model results in a gain in constraining power of approximately 17% in the  $\Omega_m - S_8$  parameter plane.

A different approach, the halo occupation distribution in the halo model, enables a connection between the masses of halos in which galaxies live and their large-scale bias. We use our constraints on linear bias parameters (along with the galaxy number density) and estimate the host-halo masses of redMaGiC galaxies. We marginalize over the halo occupation distribution parameters and obtain 25% constraints on the mean mass of host halos. We show these constraints, including its evolution with redshift in Fig. 15, finding a halo mass of approximately  $1.5 \times 10^{13} M_\odot/h$  and its evolution with redshift consistent with the expected pseudoevolution due to changing background density.

The  $2 \times 2$ pt combination of probes plays a crucial role in extracting the most cosmological information from LSS surveys, especially in constraining the matter content of the Universe ( $\Omega_m$ ) and the dark energy equation of state ( $w$ ).

In this analysis we measure the combination of galaxy clustering and galaxy-galaxy lensing at approximately  $200\sigma$ ; this significance is expected to dramatically increase with imminent large-scale surveys like the Euclid Space Telescope, the Dark Energy Spectroscopic Instrument, the Nancy G. Roman Space Telescope, and the Vera C. Rubin Observatory Legacy Survey of Space and Time. In order to optimally analyze these high-precision measurements, especially at nonlinear small scales, we need better models and ensure their proper validation before applying them to measurements. We have shown that the hybrid perturbation theory galaxy-bias model can be validated with simulations to sufficient accuracy for the present analysis. By relaxing the priors on all five parameters (per redshift bin), the model's accuracy can be improved though the increase in model complexity poses other challenges in parameter estimation. Finally, and perhaps most importantly, we have highlighted how understanding potential sources of systematic uncertainty is of paramount importance for extracting unbiased cosmological information in this era of precision cosmology.

### ACKNOWLEDGMENTS

E. K. is supported by the Department of Energy Grant No. DE-SC0020247 and the David and Lucile Packard Foundation. S. P. and B. J. are supported in part by the U.S. Department of Energy Grant No. DE-SC0007901 and NASA ATP Grant No. NNH17ZDA001N. Funding for the DES Projects has been provided by the U.S. Department of Energy, the U.S. National Science Foundation, the Ministry of Science and Education of Spain, the Science and Technology Facilities Council of the United Kingdom, the Higher Education Funding Council for England, the National Center for Supercomputing Applications at the University of Illinois at Urbana-Champaign, the Kavli Institute of Cosmological Physics at the University of Chicago, the Center for Cosmology and Astro-Particle Physics at The Ohio State University, the Mitchell Institute for Fundamental Physics and Astronomy at Texas A&M University, Financiadora de Estudos e Projetos, Fundação Carlos Chagas Filho de Amparo à Pesquisa do Estado do Rio de Janeiro, Conselho Nacional de Desenvolvimento Científico e Tecnológico and the Ministério da Ciência, Tecnologia e Inovação, the Deutsche Forschungsgemeinschaft and the Collaborating Institutions in the Dark Energy Survey. The Collaborating Institutions are Argonne National Laboratory, the University of California at Santa Cruz, the University of Cambridge, Centro de Investigaciones Energéticas, Medioambientales y Tecnológicas-Madrid, the University of Chicago, University College London, the DES-Brazil Consortium, the University of Edinburgh, the Eidgenössische Technische Hochschule (ETH) Zürich, Fermi National Accelerator Laboratory, the University of Illinois at Urbana-Champaign, the Institut de Ciències de l'Espai (IEEC/CSIC), the Institut de Física d'Altes Energies, Lawrence Berkeley National Laboratory, the Ludwig-Maximilians Universität

München and the associated Excellence Cluster Universe, the University of Michigan, the National Optical Astronomy Observatory, the University of Nottingham, The Ohio State University, the University of Pennsylvania, the University of Portsmouth, SLAC National Accelerator Laboratory, Stanford University, the University of Sussex, Texas A&M University, and the OzDES Membership Consortium. The DES data management system is supported by the National Science Foundation under Grants No. AST-1138766 and No. AST-1536171. The DES participants from Spanish institutions are partially supported by MINECO under Grants No. AYA2015-71825, No. ESP2015-88861, No. FPA2015-68048, No. SEV-2012-0234, No. SEV-2016-0597, and No. MDM-2015-0509, some of which include ERDF funds from the European Union. I. F. A. E. is partially funded by the CERCA program of the Generalitat de Catalunya. Research leading to these results has received funding from the European Research Council under the European Union's Seventh Framework Program (FP7/2007-2013) including ERC Grant Agreements No. 240672, No. 291329, and No. 306478. We acknowledge support from the Australian Research Council Centre of Excellence for All-sky Astrophysics (CAASTRO), through Project No. CE110001020. This manuscript has been authored by Fermi Research Alliance, LLC under Contract No. DE-AC02-07CH11359 with the U.S. Department of Energy, Office of Science, Office of High Energy Physics. The United States Government retains and the publisher, by accepting the article for publication, acknowledges that the United States Government retains a non-exclusive, paid-up, irrevocable, world-wide license to publish or reproduce the published form of this manuscript, or allow others to do so, for United States Government purposes. Based in part on observations at Cerro Tololo Inter-American Observatory, National Optical Astronomy Observatory, which is operated by the Association of Universities for Research in Astronomy (AURA) under a cooperative agreement with the National Science Foundation. The analysis made use of the software tools SciPy [120], NumPy [121], MATPLOTLIB [122], CAMB [123–125], GetDist [126], MultiNest [127–129], POLYCHORD [130], CosmoSIS [131], CosmoLike [132] and Treecorr [133].

### APPENDIX A: POINT-MASS MARGINALIZATION

The point-mass parameter ( $B$ ) can also be expressed as residual mass bias  $B = \delta M / \pi$ , where  $\delta M$  is approximately related to the difference between the model and true estimate of halo mass below the scales of our model validity ( $r_{\min}$ ). More accurately,  $\delta M_{\text{halo}}$  can be expressed in terms of galaxy-matter correlation as

$$\delta M = \int_0^{r_{\min}} dr_p (2\pi r_p) \int_{-\infty}^{\infty} d\Pi \Delta \xi_{\text{gm}} \left( \sqrt{r_p^2 + \Pi^2}, z \right), \quad (\text{A1})$$

where  $\Delta \xi_{\text{gm}} = \xi_{\text{gm}}^{\text{true}} - \xi_{\text{gm}}^{\text{model}}$ .

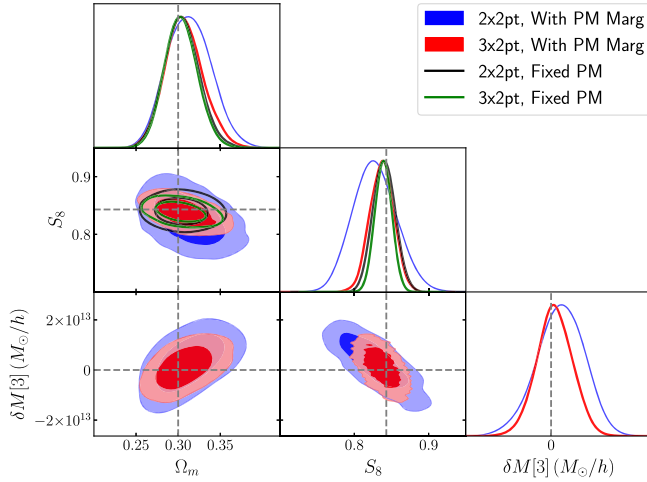


FIG. 16. Effect of point-mass marginalization on the constraining power of  $2 \times 2$ pt and  $3 \times 2$ pt. We see that the constraining power of  $2 \times 2$ pt degrades significantly with point-mass marginalization, while for  $3 \times 2$ pt the change is minimal. Including the shear-shear correlation breaks the degeneracy between point mass (we show PM for third bin,  $M_{\text{halo}}[3]$ ) and  $S_8$ , leading to smaller sensitivity of cosmology constraints on point-mass constraints.

In Fig. 16 we compare the constraining power of  $2 \times 2$ pt and  $3 \times 2$ pt *simulated* analysis at our fiducial scale cuts for different point-mass parameter settings. We generate a noiseless theory baseline data vector using the linear bias model and the fiducial parameter values given in Table I. In the blue and red filled contours, instead of analytically marginalizing over the point-mass parameters, we explicitly sample them when analyzing  $2 \times 2$ pt and  $3 \times 2$ pt data vectors, respectively. To test the impact of point-mass marginalization on the constraining power, we also show the constraints obtained after fixing the PM parameters to their fiducial value of zero using unfilled contours. The black and green unfilled contours show the constraints using  $2 \times 2$ pt and  $3 \times 2$ pt data vectors, respectively. We see that, although point-mass marginalization has a significant impact on the constraining power of the  $2 \times 2$ pt analysis, it has a small impact on the  $3 \times 2$ pt analysis. The main reason is that, due to extra constraints from cosmic shear, we break the degeneracy between PM parameters and cosmological parameters, and hence uncertainty in PM parameters does not dilute our cosmology constraints.

As PM marginalization degrades the constraining power of  $2 \times 2$ pt significantly, it might be desirable to implement an informative prior on the PM parameters. However, motivating an astrophysical prior on the PM parameters is not possible for our scale cuts as the majority of residual mass constraints are contributed from the two-halo regime, as shown in Fig. 17. For simplicity, we assume all our galaxies occupy the center of  $2.5 \times 10^{13} M_{\odot}/h$  mass halos. The input “truth” curve in black solid line uses  $\xi_{\text{gm}}$  that is generated using the Navarro-Frenk-White profile [134] in

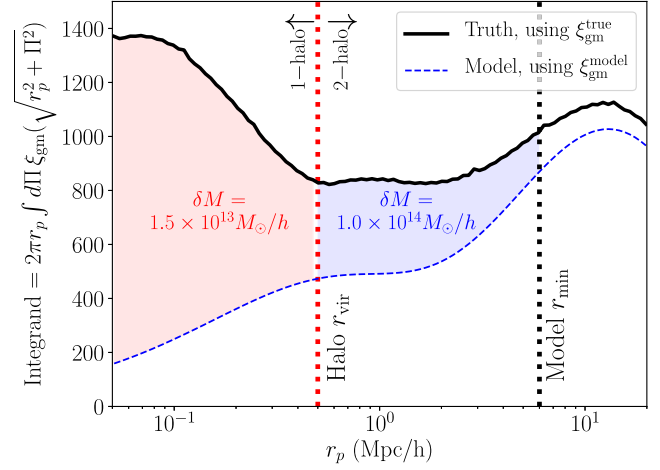


FIG. 17. We show the contribution to the residual mass shown in Eq. (A1) from different radial regimes. We find a significant contribution from the two-halo regime and therefore we cannot motivate an astrophysical informative prior on the PM parameters, without putting an informative prior on cosmology as well.

the one-halo regime ( $r < 0.5$  Mpc/h) and one-loop PT in the two-halo regime ( $r > 0.5$  Mpc/h). Given this input halo mass, the halo model framework predicts the effective large-scale linear bias value [105]. The dashed blue curve is generated using a linear bias model, using a linear bias value that is  $1\sigma$  lower from this predicted value. Here  $\sigma$  is the uncertainty obtained from  $2 \times 2$ pt marginalized constraints on the galaxy bias for first tomographic bin. The area between the two curves below some scale is equal to total  $\delta M$  as calculated using Eq. (A1).

We show the contribution to  $\delta M$  separately for the one-halo region (below the red dashed line) and two-halo regimes [up to the scales of 6 Mpc/h, which are our scale cuts for  $\gamma_t(\theta)$ ]. We find that the two-halo regime contributes significantly more than the one-halo region and the resulting  $\delta M$  value is significantly more than the input halo mass of  $2.5 \times 10^{13} M_{\odot}/h$ . An informative prior would amount to understanding the galaxy-matter correlation and its dependence on cosmology and galaxy-bias model from all scales below our scale cuts. Therefore we choose an uninformative wide prior on the point-mass parameters.

The baseline model parametrization assumes the point-mass parameter to be constant within each tomographic bin. We test this assumption implicitly in the suite of Buzzard simulations. The data vector measured in  $N$ -body Buzzard simulation will capture the effects of evolving point-mass parameters due to the evolution of the galaxy-matter correlation within a lens tomographic bin. As we have validated that our scale cuts pass our threshold criteria of bias in cosmological parameters being less than  $0.3\sigma$ , we can conclude that the effect of point-mass parameter evolution is small. Here we also test this effect explicitly by generating a simulated galaxy matter correlation function using the halo model. We assume a constant HOD of

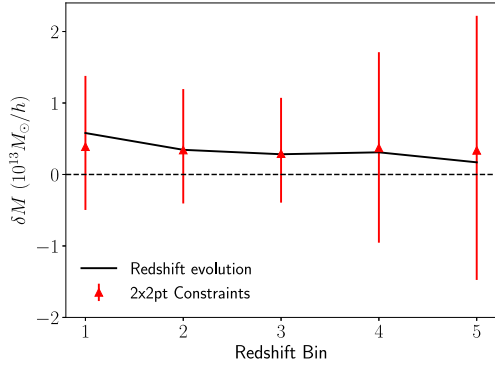


FIG. 18. We show the effect of the evolution of galaxy matter correlation functions on the PM parameters for each tomographic bin in the black line. The red error bars show the expected error bars on PM parameters for  $2 \times 2$ pt as shown in Fig. 16. The blue error bars are the constraints from  $3 \times 2$ pt.

the redMaGiC galaxies but include the evolution of halo mass function and halo bias to predict the evolution of the galaxy-matter correlation function. The contribution to the PM parameter due to this evolution in each tomographic bin is given by Eq. (A1). In Fig. 18, we show this contribution to each redshift bin by the black solid line. We compare this bias with the expected level of uncertainty in the PM parameters by plotting the marginalized constraints on these parameters as shown in Fig. 16 for  $2 \times 2$ pt analyses. We see that the uncertainty in PM parameters is significantly greater than the expected bias.

## APPENDIX B: DATA VECTOR RESIDUALS

We show the comparison between our measurements and best-fit theory data vector in Fig. 19. We show the residuals between data and best-fit theory model from both the

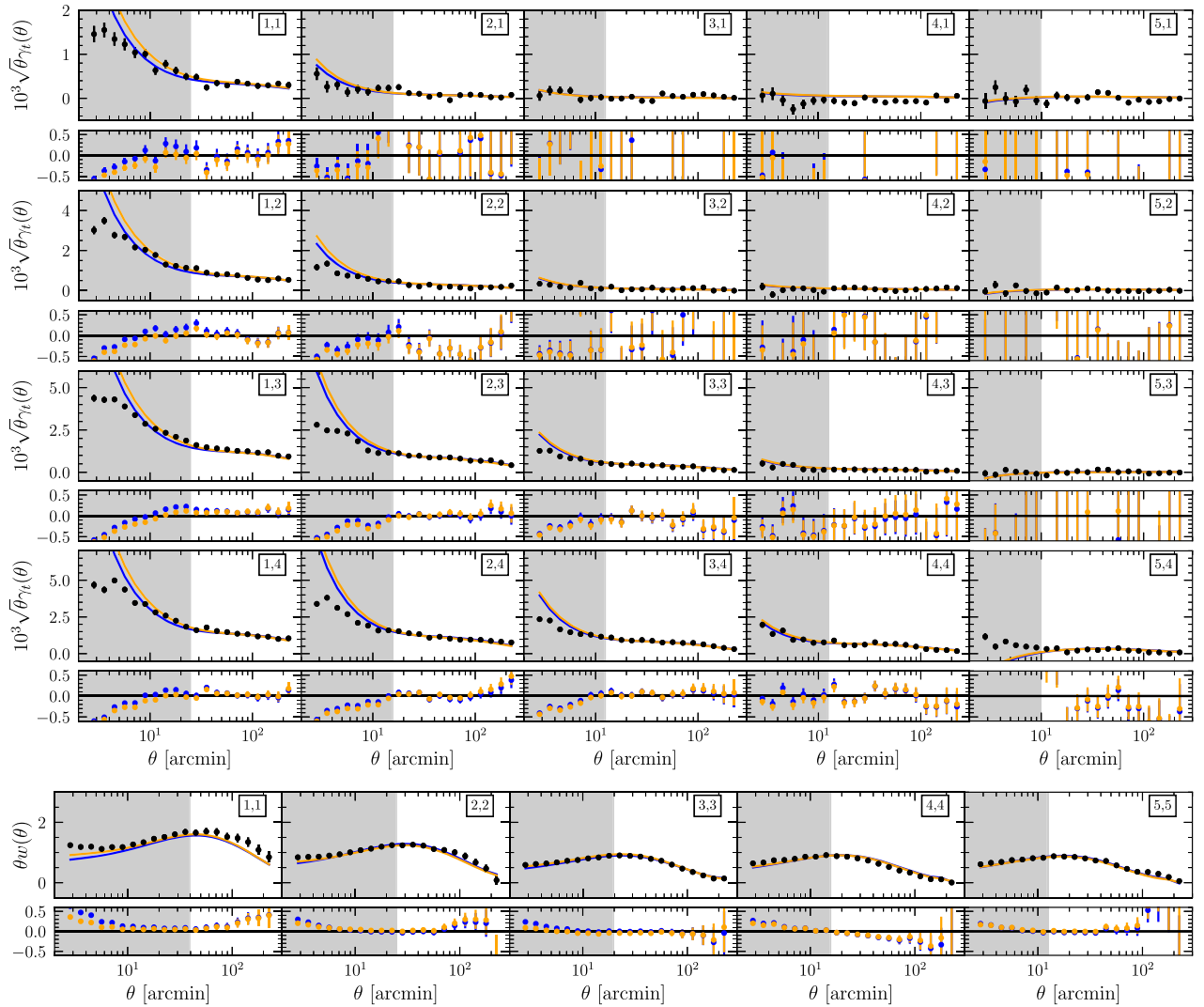


FIG. 19. The measurements of  $w(\theta)$  and  $\gamma_t(\theta)$  with redMaGiC sample are shown with black dots. We show the best fit using the fiducial linear bias model in blue and model with  $X_{\text{lens}} = 0.87$  in orange.

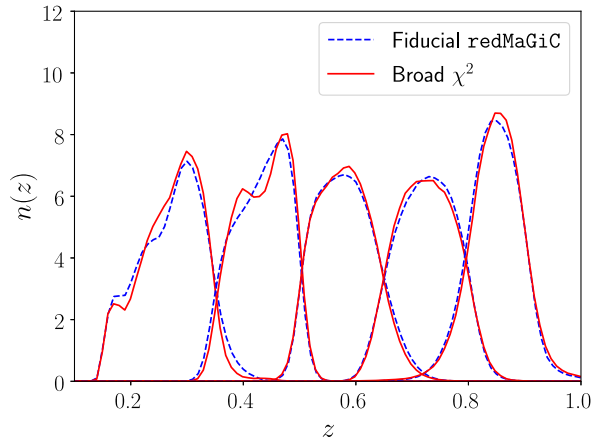


FIG. 20. We compare the redshift distribution of the fiducial redMaGiC sample with the broad- $\chi^2$  redMaGiC sample.

fiducial model as well as with  $X_{\text{lens}} = 0.87$  model. Using the fiducial linear bias model scale cuts of  $(8, 6)$  Mpc/ $h$  (that leaves 302 data points in total), we find a minimum  $\chi^2$  of 347.2 and 351.1 for the fiducial model and  $X_{\text{lens}} = 0.87$  model, respectively.

### APPENDIX C: BROAD- $\chi^2$ SAMPLE

As detailed in the main text, we generate a new galaxy sample by relaxing the selection criteria and selecting galaxies with goodness of fit  $\chi^2_{\text{RM}} = 8$  to the redMaGiC template. This new sample is constructed to reduce the sensitivity of any color-dependent photometric issue that might be present in the fiducial redMaGiC sample and causing  $X_{\text{lens}} < 1$ . After analyzing the  $2 \times 2$ pt data vector, we do find that this sample prefers  $X_{\text{lens}} = 1$  and results in  $S_8$  consistent with the MagLim galaxy sample.

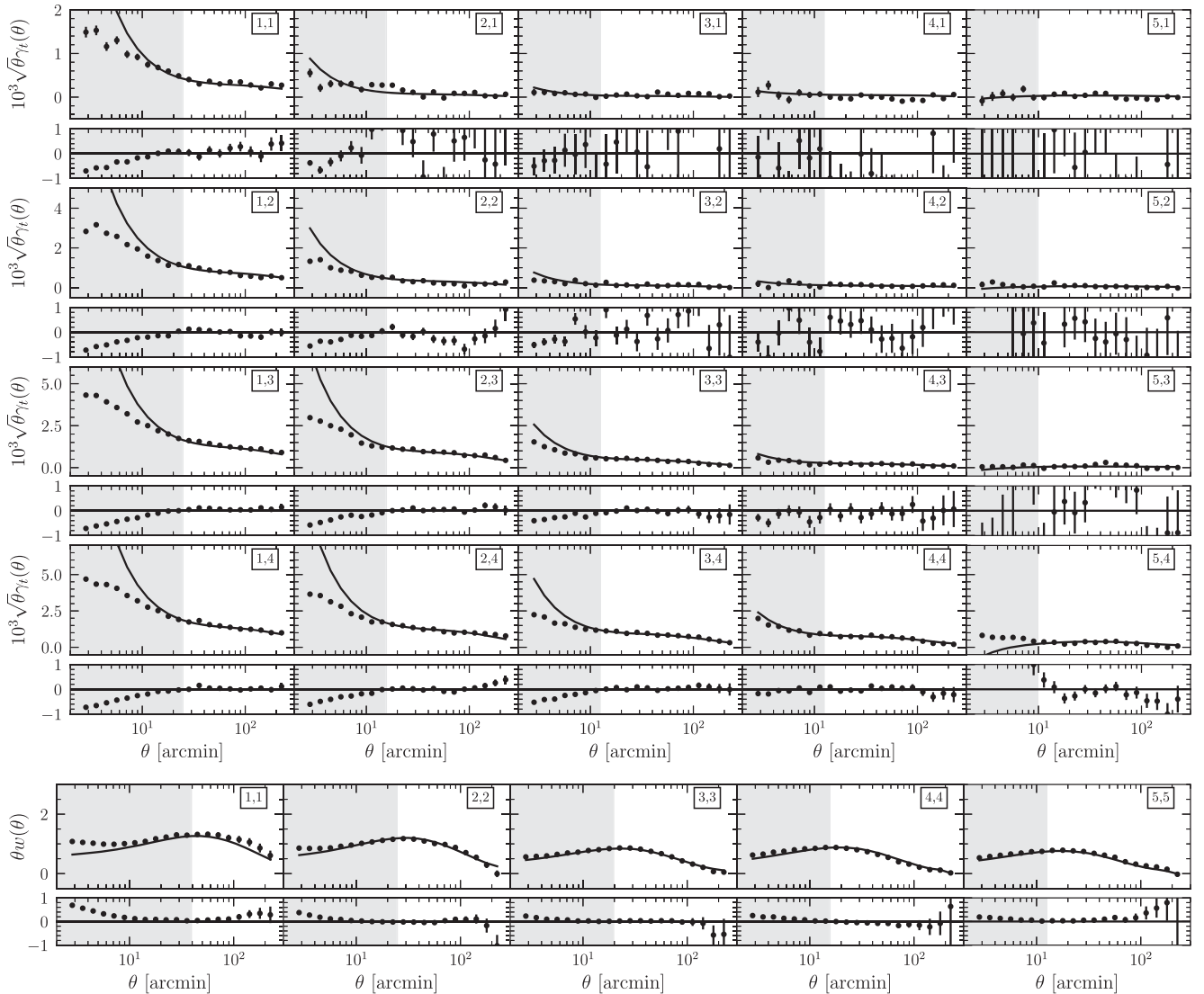


FIG. 21. The measurements of  $w(\theta)$  and  $\gamma_t(\theta)$  with the broad- $\chi^2$  redMaGiC sample are shown with black dots. We show the best-fit model in black.

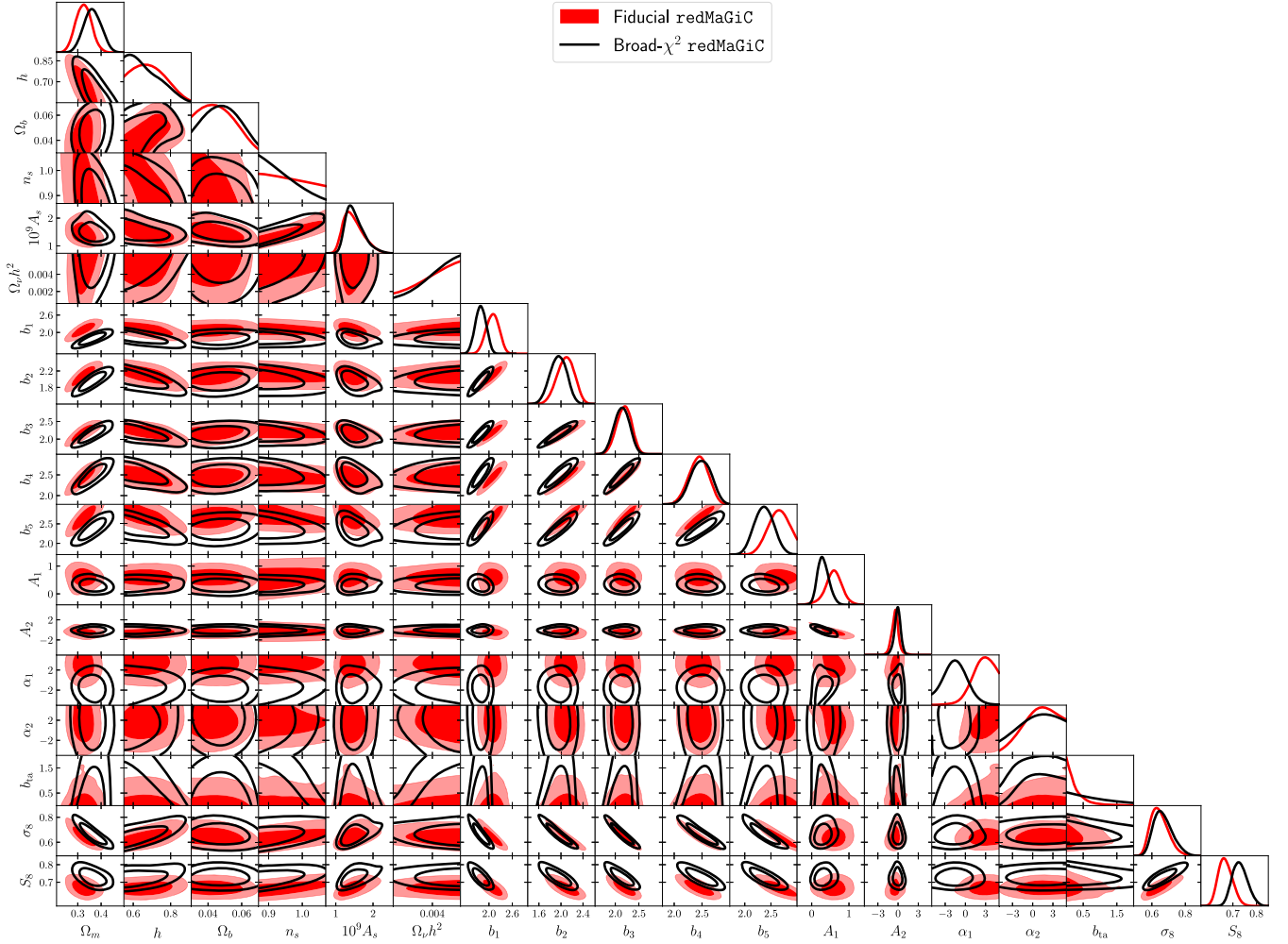


FIG. 22. Comparison of parameter constraints using fiducial and broad- $\chi^2$  redMaGiC for all the parameters sampled in the analysis without a tight Gaussian prior. We also show the derived parameters  $\sigma_8$  and  $S_8$ .

In Fig. 20, we show the comparison of the lens number densities for the five tomographic bins. We perform the calibration of these redshift distributions using cross-correlations with BOSS and eBOSS data using the same methods described in Cawthon *et al.* [80]. The lens photo- $z$  priors that we use are shown in Table II. After down-sampling the full catalog by a factor of 2, the number densities (in the units of  $\text{arcmin}^{-2}$ ) for this sample are  $\langle n_g \rangle = 0.027, 0.04, 0.07, 0.03, 0.03$  for the five tomographic bins. We generate a non-Gaussian covariance corresponding to these number densities. To mitigate the bias caused by wrong parameter values input to theory covariance calculations, we recalculate the covariance matrix using the best-fit parameters of an initial  $2 \times 2$ pt analysis and show the cosmological constraints corresponding to this new covariance.

Using the best-fit parameter values obtained with the linear bias model, we show the residuals in Fig. 21. We find a best-fit  $\chi^2$  of 353 for 302 data points, and both the  $w(\theta)$  and  $\gamma_t$  measurements are fit well with a linear bias,  $\Lambda$ CDM

model. In Fig. 22 we show the parameters constraints and compare them to the ones obtained with the fiducial redMaGiC sample.

#### APPENDIX D: HALO MASS INFERENCE

In this section we detail the methodology to infer the host-halo mass of our redMaGiC lens galaxy sample from the constraints on galaxy-bias parameters and number density. We use the halo model framework to make this prediction and parametrize the number of galaxies in a halo of mass  $M$  in tomographic bin  $j$  as  $N_g^j(M) = N_{\text{cen}}^j(M) + N_{\text{sat}}^j(M)$ , where  $N_{\text{cen}}^j$  is the number of central galaxies and  $N_{\text{sat}}^j$  is the number of satellite galaxies. We parametrize these two components as

$$N_{\text{cen}}^j = \frac{f_{\text{cen}}^j}{2} \left[ 1 + \text{erf} \left( \frac{\log M - (\log M_{\text{min}})^j}{(\sigma_{\log M})^j} \right) \right], \quad (\text{D1})$$

$$N_{\text{sat}}^j = \frac{1}{2} \left[ 1 + \text{erf} \left( \frac{\log M - (\log M_{\text{min}})^j}{(\sigma_{\log M})^j} \right) \right] \times \left( \frac{M_h}{M_1^j} \right)^{\alpha_j}. \quad (\text{D2})$$

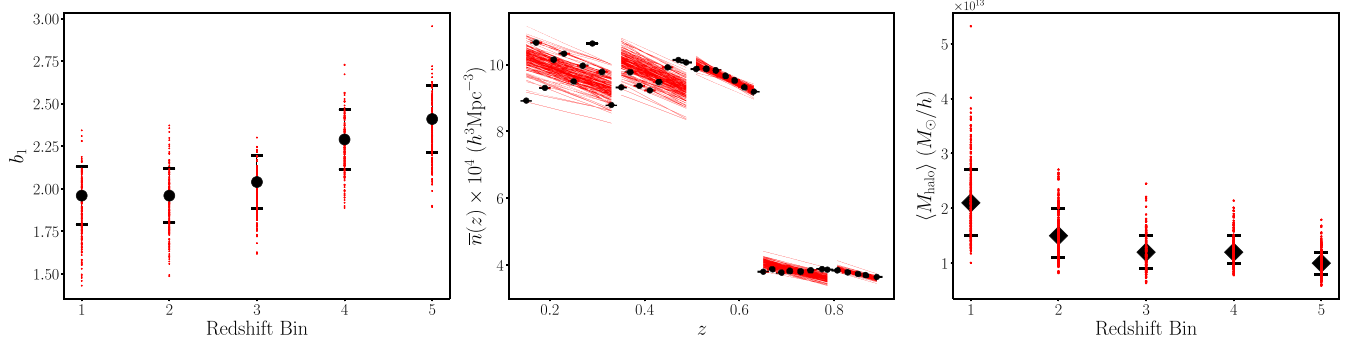


FIG. 23. This figure shows the marginalized constraints on the large-scale bias of redMaGiC sample for the five tomographic bins on the left panel. The black dots denote the mean, and the error bars correspond to 68% credible interval. Using these constraints and comoving number density (middle panel), we infer the constraints on mean halo mass, as shown in the right panel for five tomographic bins. The red line and dots correspond to MCMC samples. We use the linear bias model with  $X_{\text{lens}} = 0.87$ .

Here we have five free parameters,  $f_{\text{cen}}^j$ ,  $(\log M_{\text{min}})^j$ ,  $(\sigma_{\log M})^j$ ,  $M_1^j$  and  $\alpha^j$ , that we marginalize over. We can predict the comoving number density ( $\bar{n}(z)^j$ ) and galaxy bias for a given tomographic bin  $j$ ,  $b_1^j$ , from galaxy HOD as follows:

$$\bar{n}^j(z) = \int_0^\infty dM \frac{dn}{dM} N_g^j(M),$$

$$b_1^j = \int dz \frac{n_g^j(z)}{\bar{n}^j(z)} \int_0^\infty dM \frac{dn}{dM} N_g^j(M) b_1^{\text{halo}}(M, z). \quad (\text{D3})$$

We use the Tinker *et al.* [135] halo mass function ( $dn/dM$ ) and the Tinker *et al.* [136] relation for linear halo bias [ $b_1^{\text{halo}}(M, z)$ ].

Therefore, Eqs. (D3) allow us to predict the number density and galaxy-bias values. We then sample these HOD parameters to fit the data vector  $\vec{\mathcal{D}}_H = [\bar{n}^j(z_1) \dots \bar{n}^j(z_n), b_1^j, b_2^j]$  of length  $d$ , where  $\bar{n}^j(z_1) \dots \bar{n}^j(z_n)$  are the  $n = d - 2$  observed comoving number density of redMaGiC galaxies as shown in middle panel of

Fig. 23 and  $b_1^j$  and  $b_2^j$  are the marginalized mean bias values obtained at our fiducial scale cut. For a given set of HOD parameters ( $\Theta_H$ ), the theoretical prediction is given by  $\mathcal{T}_H$  and we write our log-likelihood as

$$\ln \mathcal{L}(\vec{\mathcal{D}}_H | \Theta) = -\frac{1}{2} [(\vec{\mathcal{D}}_H - \vec{\mathcal{T}}_H(\Theta_H)) \mathcal{C}_H^{-1} \times (\vec{\mathcal{D}}_H - \vec{\mathcal{T}}_H(\Theta_H))^T - \ln(|\mathcal{C}_H|)]. \quad (\text{D4})$$

In order to account for variation of HOD within a tomographic bin that contributes to the variation on  $\bar{n}^j(z)$  within each tomographic bin as seen in Fig. 23, we implement an analytical marginalization scheme. We change the covariance of our data vector  $\mathcal{C}_H$  as

$$\mathcal{C}_H \rightarrow \mathcal{C}_H + \alpha_c \mathcal{I}_D, \quad (\text{D5})$$

where  $\mathcal{I}_D$  is a diagonal matrix of dimension  $d \times d$  whose diagonal elements equal to 1 from index 1 to  $d - 1$  and equal to 0 otherwise. We sample over the parameter  $\alpha_c$ , treating it as a free parameter.

[1] M. Cacciato, F. C. van den Bosch, S. More, R. Li, H. J. Mo, and X. Yang, *Mon. Not. R. Astron. Soc.* **394**, 929 (2009).  
[2] T. Baldauf, R. E. Smith, U. Seljak, and R. Mandelbaum, *Phys. Rev. D* **81**, 063531 (2010).  
[3] M. Cacciato, O. Lahav, F. C. van den Bosch, H. Hoekstra, and A. Dekel, *Mon. Not. R. Astron. Soc.* **426**, 566 (2012).  
[4] F. C. van den Bosch, S. More, M. Cacciato, H. Mo, and X. Yang, *Mon. Not. R. Astron. Soc.* **430**, 725 (2013).  
[5] B. D. Wibking, A. N. Salcedo, D. H. Weinberg, L. H. Garrison, D. Ferrer, J. Tinker, D. Eisenstein, M. Metchnik, and P. Pinto, *Mon. Not. R. Astron. Soc.* **484**, 989 (2018).

[6] M. Cacciato, F. C. van den Bosch, S. More, H. Mo, and X. Yang, *Mon. Not. R. Astron. Soc.* **430**, 767 (2013).  
[7] R. Mandelbaum, A. Slosar, T. Baldauf, U. Seljak, C. M. Hirata, R. Nakajima, R. Reyes, and R. E. Smith, *Mon. Not. R. Astron. Soc.* **432**, 1544 (2013).  
[8] J. Kwan, C. Sánchez, J. Clampitt, J. Blazek, M. Crocce, B. Jain, J. Zuntz, A. Amara, M. R. Becker, G. M. Bernstein *et al.*, *Mon. Not. R. Astron. Soc.* **464**, 4045 (2016).  
[9] S. More, H. Miyatake, R. Mandelbaum, M. Takada, D. N. Spergel, J. R. Brownstein, and D. P. Schneider, *Astrophys. J.* **806**, 2 (2015).

- [10] A. Dvornik, H. Hoekstra, K. Kuijken, P. Schneider, A. Amon, R. Nakajima, M. Viola, A. Choi, T. Erben, D. J. Farrow *et al.*, *Mon. Not. R. Astron. Soc.* **479**, 1240 (2018).
- [11] J. Coupon, S. Arnouts, L. van Waerbeke, T. Moutard, O. Ilbert, E. van Uitert, T. Erben, B. Garilli, L. Guzzo, C. Heymans *et al.*, *Mon. Not. R. Astron. Soc.* **449**, 1352 (2015).
- [12] S. Singh, R. Mandelbaum, U. Seljak, S. Rodríguez-Torres, and A. Slosar, *Mon. Not. R. Astron. Soc.* **491**, 51 (2019).
- [13] B. D. Wibking, D. H. Weinberg, A. N. Salcedo, H.-Y. Wu, S. Singh, S. Rodríguez-Torres, L. H. Garrison, and D. J. Eisenstein, *Mon. Not. R. Astron. Soc.* **492**, 2872 (2019).
- [14] M. Troxel, N. MacCrann, J. Zuntz, T. Eifler, E. Krause, S. Dodelson, D. Gruen, J. Blazek, O. Friedrich, S. Samuroff *et al.*, *Phys. Rev. D* **98**, 043528 (2018).
- [15] T. Abbott, F. Abdalla, A. Alarcon, J. Aleksić, S. Allam, S. Allen, A. Amara, J. Annis, J. Asorey, S. Avila *et al.*, *Phys. Rev. D* **98**, 043526 (2018).
- [16] A. Amon *et al.*, *Phys. Rev. D* **105**, 023514 (2022).
- [17] L. F. Secco, S. Samuroff *et al.*, *Phys. Rev. D* **105**, 023515 (2022).
- [18] A. Porredon *et al.*, [arXiv:2105.13546](https://arxiv.org/abs/2105.13546) [Phys. Rev. D (to be published)].
- [19] J. Elvin-Poole, N. MacCrann *et al.* [Mon. Not. R. Astron. Soc. (to be published)].
- [20] T. M. C. Abbott *et al.* (DES Collaboration), *Phys. Rev. D* **105**, 023520 (2022).
- [21] M. Rodríguez-Monroy *et al.*, *Mon. Not. R. Astron. Soc.* **511**, 2665 (2022).
- [22] J. Prat *et al.*, *Phys. Rev. D* **105**, 083528 (2022).
- [23] E. Rozo, E. S. Rykoff, A. Abate, C. Bonnett, M. Crocce, C. Davis, B. Hoyle, B. Leistedt, H. V. Peiris, R. H. Wechsler *et al.*, *Mon. Not. R. Astron. Soc.* **461**, 1431 (2016).
- [24] A. Porredon *et al.* (DES Collaboration), *Phys. Rev. D* **103**, 043503 (2021).
- [25] J. N. Fry and E. Gaztanaga, *Astrophys. J.* **413**, 447 (1993).
- [26] R. J. Scherrer and D. H. Weinberg, *Astrophys. J.* **504**, 607 (1998).
- [27] J. DeRose *et al.*, [arXiv:1901.02401](https://arxiv.org/abs/1901.02401).
- [28] P. Fosalba, E. Gaztañaga, F. J. Castander, and M. Crocce, *Mon. Not. R. Astron. Soc.* **447**, 1319 (2014).
- [29] M. Crocce, F. J. Castander, E. Gaztañaga, P. Fosalba, and J. Carretero, *Mon. Not. R. Astron. Soc.* **453**, 1513 (2015).
- [30] P. Fosalba, M. Crocce, E. Gaztañaga, and F. J. Castander, *Mon. Not. R. Astron. Soc.* **448**, 2987 (2015).
- [31] C. Heymans *et al.*, *Mon. Not. R. Astron. Soc.* **432**, 2433 (2013).
- [32] C. Heymans, T. Tröster, M. Asgari, C. Blake, H. Hildebrandt, B. Joachimi, K. Kuijken, C.-A. Lin, A. G. Sánchez, J. L. van den Busch *et al.*, *Astron. Astrophys.* **646**, A140 (2021).
- [33] C. Hikage, M. Oguri, T. Hamana, S. More, R. Mandelbaum, M. Takada, F. Köhlinger, H. Miyatake, A. J. Nishizawa, H. Aihara *et al.*, *Publ. Astron. Soc. Jpn.* **71**, 43 (2019).
- [34] T. Abbott, M. Aguena, A. Alarcon, S. Allam, S. Allen, J. Annis, S. Avila, D. Bacon, K. Bechtol, A. Bermeo *et al.*, *Phys. Rev. D* **102**, 023509 (2020).
- [35] C. To, E. Krause, E. Rozo, H. Wu, D. Gruen, R. Wechsler, T. Eifler, E. Rykoff, M. Costanzi, M. Becker *et al.*, *Phys. Rev. Lett.* **126**, 141301 (2021).
- [36] O. H. Philcox, M. M. Ivanov, M. Simonović, and M. Zaldarriaga, *J. Cosmol. Astropart. Phys.* **05** (2020) 032.
- [37] R. Takahashi, M. Sato, T. Nishimichi, A. Taruya, and M. Oguri, *Astrophys. J.* **761**, 152 (2012).
- [38] S. Bird, M. Viel, and M. G. Haehnelt, *Mon. Not. R. Astron. Soc.* **420**, 2551 (2012).
- [39] E. Krause *et al.*, [arXiv:2105.13548](https://arxiv.org/abs/2105.13548) [Phys. Rev. D (to be published)].
- [40] A. J. Mead, S. Brieden, T. Tröster, and C. Heymans, *Mon. Not. R. Astron. Soc.* **502**, 1401 (2021).
- [41] P. McDonald and A. Roy, *J. Cosmol. Astropart. Phys.* **08** (2009) 020.
- [42] S. Saito, T. Baldauf, Z. Vlah, U. Seljak, T. Okumura, and P. McDonald, *Phys. Rev. D* **90**, 123522 (2014).
- [43] S. Pandey, E. Krause, B. Jain, N. MacCrann, J. Blazek, M. Crocce, J. DeRose, X. Fang, I. Ferrero, O. Friedrich *et al.*, *Phys. Rev. D* **102**, 123522 (2020).
- [44] P. Simon and S. Hilbert, *Astron. Astrophys.* **613**, A15 (2018).
- [45] V. Springel, S. D. M. White, A. Jenkins, C. S. Frenk, N. Yoshida, L. Gao, J. Navarro, R. Thacker, D. Croton, J. Helly *et al.*, *Nature (London)* **435**, 629 (2005).
- [46] B. M. B. Henriques, S. D. M. White, P. A. Thomas, R. Angulo, Q. Guo, G. Lemson, V. Springel, and R. Overzier, *Mon. Not. R. Astron. Soc.* **451**, 2663 (2015).
- [47] S. Goldstein, S. Pandey, A. Slosar, J. Blazek, B. Jain (The LSST Dark Energy Science Collaboration), *Phys. Rev. D* **105**, 123518 (2022).
- [48] D. N. Limber, *Astrophys. J.* **117**, 134 (1953).
- [49] M. LoVerde and N. Afshordi, *Phys. Rev. D* **78**, 123506 (2008).
- [50] X. Fang, E. Krause, T. Eifler, and N. MacCrann, *J. Cosmol. Astropart. Phys.* **05** (2020) 010.
- [51] O. Friedrich *et al.* (DES Collaboration), *Mon. Not. R. Astron. Soc.* **508**, 3125 (2021).
- [52] J. A. Blazek, N. MacCrann, M. Troxel, and X. Fang, *Phys. Rev. D* **100**, 103506 (2019).
- [53] S. Bridle and L. King, *New J. Phys.* **9**, 444 (2007).
- [54] C. M. Hirata and U. Seljak, *Phys. Rev. D* **70**, 063526 (2004).
- [55] E. Krause *et al.*, [arXiv:1706.09359](https://arxiv.org/abs/1706.09359).
- [56] J. Blazek, Z. Vlah, and U. Seljak, *J. Cosmol. Astropart. Phys.* **08** (2015) 015.
- [57] E. Suchyta, E. M. Huff, J. Aleksić, P. Melchior, S. Jouvel, N. MacCrann, A. J. Ross, M. Crocce, E. Gaztanaga, K. Honscheid *et al.*, *Mon. Not. R. Astron. Soc.* **457**, 786 (2016).
- [58] S. Everett *et al.*, *Astrophys. J. Suppl. Ser.* **258**, 15 (2022).
- [59] W. G. Hartley, A. Choi *et al.* (DES Collaboration), *Mon. Not. R. Astron. Soc.* **509**, 3547 (2022).
- [60] E. Morganson, R. A. Gruendl, F. Menanteau, M. C. Kind, Y.-C. Chen, G. Daues, A. Drlica-Wagner, D. N. Friedel, M. Gower, M. W. G. Johnson *et al.*, *Publ. Astron. Soc. Pac.* **130**, 074501 (2018).
- [61] I. Sevilla-Noarbe *et al.* (DES Collaboration), *Astrophys. J. Suppl. Ser.* **254**, 24 (2021).
- [62] N. MacCrann, J. Blazek, B. Jain, and E. Krause, *Mon. Not. R. Astron. Soc.* **491**, 5498 (2020).



- [63] Y. Park, E. Rozo, and E. Krause, *Phys. Rev. Lett.* **126**, 021301 (2021).
- [64] M. Asgari, I. Friswell, M. Yoon, C. Heymans, A. Dvornik, B. Joachimi, P. Simon, and J. Zuntz, *Mon. Not. R. Astron. Soc.* **501**, 3003 (2020).
- [65] B. Flaugher, H. T. Diehl, K. Honscheid, T. M. C. Abbott, O. Alvarez, R. Angstadt, J. T. Annis, M. Antonik, O. Ballester, L. Beaufore *et al.*, *Astron. J.* **150**, 150 (2015).
- [66] I. Sevilla *et al.*, [arXiv:1109.6741](https://arxiv.org/abs/1109.6741).
- [67] E. Morganson *et al.* (DES Collaboration), *Publ. Astron. Soc. Pac.* **130**, 074501 (2018).
- [68] <https://des.ncsa.illinois.edu/releases/drl>.
- [69] J. De Vicente, E. Sánchez, and I. Sevilla-Noarbe, *Mon. Not. R. Astron. Soc.* **459**, 3078 (2016).
- [70] E. S. Sheldon and E. M. Huff, *Astrophys. J.* **841**, 24 (2017).
- [71] E. Huff and R. Mandelbaum, [arXiv:1702.02600](https://arxiv.org/abs/1702.02600).
- [72] M. Jarvis *et al.* (DES Collaboration), *Mon. Not. R. Astron. Soc.* **501**, 1282 (2021).
- [73] M. Gatti, E. Sheldon *et al.* (DES Collaboration), *Mon. Not. R. Astron. Soc.* **504**, 4312 (2021).
- [74] N. MacCrann, M. R. Becker *et al.*, *Mon. Not. R. Astron. Soc.* **509**, 3371 (2022).
- [75] R. H. Wechsler, J. DeRose, M. T. Busha, M. R. Becker, E. Rykoff, and A. Evrard, *Astrophys. J.* **931**, 145 (2022).
- [76] M. Crocce, S. Pueblas, and R. Scoccimarro, 2LPTIC: 2nd-order lagrangian perturbation theory initial conditions (2012), [ascl:1201.005](https://ui.adsabs.harvard.edu/abs/2012ascl.soft01005C/exportcitation), <https://ui.adsabs.harvard.edu/abs/2012ascl.soft01005C/exportcitation>.
- [77] J. DeRose, M. R. Becker, and R. H. Wechsler, [arXiv:2105.12104](https://arxiv.org/abs/2105.12104).
- [78] M. R. Becker, *Mon. Not. R. Astron. Soc.* **435**, 115 (2013).
- [79] J. DeRose *et al.*, *Phys. Rev. D* **105**, 123520 (2022).
- [80] R. Cawthon *et al.* (DES Collaboration), *Mon. Not. R. Astron. Soc.* **513**, 5517 (2022).
- [81] G. Giannini *et al.*, *Phys. Rev. D* (to be published).
- [82] J. Myles, A. Alarcon *et al.*, *Mon. Not. R. Astron. Soc.* **505**, 4249 (2021).
- [83] M. Gatti, G. Giannini *et al.* (DES Collaboration), *Mon. Not. R. Astron. Soc.* **510**, 1223 (2022).
- [84] C. Sánchez, J. Prat *et al.*, *Phys. Rev. D* **105**, 083529 (2022).
- [85] S. Everett *et al.*, *Astrophys. J. Suppl. Ser.* **258**, 15 (2022).
- [86] S. D. Landy and A. S. Szalay, *Astrophys. J.* **412**, 64 (1993).
- [87] S. Singh, R. Mandelbaum, U. Seljak, A. Slosar, and J. Vazquez Gonzalez, *Mon. Not. R. Astron. Soc.* **471**, 3827 (2017).
- [88] E. Krause and T. Eifler, *Mon. Not. R. Astron. Soc.* **470**, 2100 (2017).
- [89] X. Fang, T. Eifler, and E. Krause, *Mon. Not. R. Astron. Soc.* **497**, 2699 (2020).
- [90] S. L. Bridle, R. Crittenden, A. Melchiorri, M. P. Hobson, R. Kneissl, and A. N. Lasenby, *Mon. Not. R. Astron. Soc.* **335**, 1193 (2002).
- [91] J. Muir *et al.* (DES Collaboration), *Mon. Not. R. Astron. Soc.* **494**, 4454 (2020).
- [92] P. Lemos, N. Weaverdyck *et al.*, [arXiv:2202.08233](https://arxiv.org/abs/2202.08233) [*Mon. Not. R. Astron. Soc.* (to be published)].
- [93] B. Joachimi, C.-A. Lin, M. Asgari, T. Tröster, C. Heymans, H. Hildebrandt, F. Köhlinger, A. G. Sánchez, A. H. Wright, M. Bilicki *et al.*, *Astron. Astrophys.* **646**, A129 (2021).
- [94] S. Samuroff, J. Blazek, M. A. Troxel, N. MacCrann, E. Krause, C. D. Leonard, J. Prat, D. Gruen, S. Dodelson, T. F. Eifler *et al.*, *Mon. Not. R. Astron. Soc.* **489**, 5453 (2019).
- [95] J. P. Cordero, I. Harrison *et al.*, *Mon. Not. R. Astron. Soc.* **511**, 2170 (2022).
- [96] A. M. C. Le Brun, I. G. McCarthy, J. Schaye, and T. J. Ponman, *Mon. Not. R. Astron. Soc.* **441**, 1270 (2014).
- [97] J. A. Nelder and R. Mead, *Comput. J.* **7**, 308 (1965).
- [98] N. Aghanim, Y. Akrami, M. Ashdown, J. Aumont, C. Baccigalupi, M. Ballardini, A. J. Banday, R. B. Barreiro, N. Bartolo *et al.*, *Astron. Astrophys.* **641**, A6 (2020).
- [99] M. Lemos, P. Raveri *et al.* (DES Collaboration), *Mon. Not. R. Astron. Soc.* **505**, 6179 (2021).
- [100] D. Huterer and M. S. Turner, *Phys. Rev. D* **64**, 123527 (2001).
- [101] Y. Wang, *Phys. Rev. D* **77**, 123525 (2008).
- [102] J. Prat, C. Sánchez, Y. Fang, D. Gruen, J. Elvin-Poole, N. Kokron, L. Secco, B. Jain, R. Miquel, N. MacCrann *et al.*, *Phys. Rev. D* **98**, 042005 (2018).
- [103] V. Desjacques, D. Jeong, and F. Schmidt, *Phys. Rep.* **733**, 1 (2018).
- [104] DES Collaboration *et al.*, (to be published).
- [105] A. Cooray and R. Sheth, *Phys. Rep.* **372**, 1 (2002).
- [106] G. Zacharegkas *et al.*, *Mon. Not. R. Astron. Soc.* **509**, 3119 (2022).
- [107] Z. Zheng, A. A. Berlind, D. H. Weinberg, A. J. Benson, C. M. Baugh, S. Cole, R. Dave, C. S. Frenk, N. Katz, and C. G. Lacey, *Astrophys. J.* **633**, 791 (2005).
- [108] I. Zehavi, Z. Zheng, D. H. Weinberg, M. R. Blanton, N. A. Bahcall, A. A. Berlind, J. Brinkmann, J. A. Frieman, J. E. Gunn, R. H. Lupton *et al.*, *Astrophys. J.* **736**, 59 (2011).
- [109] B. Diemer, S. More, and A. V. Kravtsov, *Astrophys. J.* **766**, 25 (2013).
- [110] J. Clampitt, C. Sánchez, J. Kwan, E. Krause, N. MacCrann, Y. Park, M. A. Troxel, B. Jain, E. Rozo, E. S. Rykoff *et al.*, *Mon. Not. R. Astron. Soc.* **465**, 4204 (2016).
- [111] G. Zacharegkas *et al.* (to be published).
- [112] A. Leauthaud, S. Saito, S. Hilbert, A. Barreira, S. More, M. White, S. Alam, P. Behroozi, K. Bundy, J. Coupon *et al.*, *Mon. Not. R. Astron. Soc.* **467**, 3024 (2017).
- [113] J. U. Lange, A. Leauthaud, S. Singh, H. Guo, R. Zhou, T. L. Smith, and F.-Y. Cyr-Racine, *Mon. Not. R. Astron. Soc.* **502**, 2074 (2021).
- [114] S. Yuan, D. J. Eisenstein, and A. Leauthaud, *Mon. Not. R. Astron. Soc.* **493**, 5551 (2020).
- [115] S. Amodeo, N. Battaglia, E. Schaan, S. Ferraro, E. Moser, S. Aiola, J. E. Austermann, J. A. Beall, R. Bean, D. T. Becker *et al.*, *Phys. Rev. D* **103**, 063514 (2021).
- [116] Y. Zu, [arXiv:2010.01143](https://arxiv.org/abs/2010.01143).
- [117] Q. Hang, S. Alam, J. A. Peacock, and Y.-C. Cai, *Mon. Not. R. Astron. Soc.* **501**, 1481 (2020).
- [118] E. Kitanidis and M. White, *Mon. Not. R. Astron. Soc.* **501**, 6181 (2020).
- [119] A. Krolewski, S. Ferraro, and M. White, *J. Cosmol. Astropart. Phys.* **12** (2021) 028.

- [120] P. Virtanen *et al.* (SciPy 1.0 Contributors), *Nat. Methods* **17**, 261 (2020).
- [121] C. R. Harris *et al.*, *Nature (London)* **585**, 357 (2020).
- [122] J. D. Hunter, *Comput. Sci. Eng.* **9**, 90 (2007).
- [123] A. Lewis, A. Challinor, and A. Lasenby, *Astrophys. J.* **538**, 473 (2000).
- [124] A. Lewis and S. Bridle, *Phys. Rev. D* **66**, 103511 (2002).
- [125] C. Howlett, A. Lewis, A. Hall, and A. Challinor, *J. Cosmol. Astropart. Phys.* 04 (2012) 027.
- [126] A. Lewis, *arXiv:1910.13970*.
- [127] F. Feroz and M. P. Hobson, *Mon. Not. R. Astron. Soc.* **384**, 449 (2008).
- [128] F. Feroz, M. P. Hobson, and M. Bridges, *Mon. Not. R. Astron. Soc.* **398**, 1601 (2009).
- [129] F. Feroz, M. P. Hobson, E. Cameron, and A. N. Pettitt, *Open J. Astrophys.* **2**, 10 (2019), <https://ui.adsabs.harvard.edu/abs/2019OJAp....2E..10F/exportcitation>.
- [130] W. J. Handley, M. P. Hobson, and A. N. Lasenby, *Mon. Not. R. Astron. Soc.* **450**, L61 (2015).
- [131] J. Zuntz, M. Paterno, E. Jennings, D. Rudd, A. Manzotti, S. Dodelson, S. Bridle, S. Sehrish, and J. Kowalkowski, *Astron. Comput.* **12**, 45 (2015).
- [132] E. Krause and T. Eifler, *Mon. Not. R. Astron. Soc.* **470**, 2100 (2017).
- [133] M. Jarvis, G. Bernstein, and B. Jain, *Mon. Not. R. Astron. Soc.* **352**, 338 (2004).
- [134] J. F. Navarro, C. S. Frenk, and S. D. M. White, *Astrophys. J.* **462**, 563 (1996).
- [135] J. Tinker, A. V. Kravtsov, A. Klypin, K. Abazajian, M. Warren, G. Yepes, S. Gottlöber, and D. E. Holz, *Astrophys. J.* **688**, 709 (2008).
- [136] J. L. Tinker, B. E. Robertson, A. V. Kravtsov, A. Klypin, M. S. Warren, G. Yepes, and S. Gottlöber, *Astrophys. J.* **724**, 878 (2010).